

On Use of Inhomogeneous Media for Elimination of Ill-Posedness in the Inverse Problem

By

Md Jamil Feroj

A thesis submitted to the Faculty of Graduate Studies of
the University of Manitoba

in partial fulfillment of the requirements of the degree of

Master of Science

Department of Electrical and Computer Engineering

University of Manitoba

Winnipeg

April 2014

Copyright © 2014 by Md Jamil Feroj

Abstract

This thesis outlines a novel approach to make ill-posed inverse source problem well-posed exploiting inhomogeneous media. More precisely, we use Maxwell fish-eye lens to make scattered field emanating from distinct regions of an object of interest more directive and concentrated onto distinct regions of observation. The object of interest in this thesis is a thin slab placed conformally to the Maxwell fish-eye lens. Focused Green's function of the background medium results in diagonal dominance of the matrix to be inverted for inverse problem solution. Hence, the problem becomes well-posed. We have studied one-dimensional variation of a very thin dielectric slab of interest having conformal shape to the lens. This method has been tested solving the forward problem using both Mie series and using COMSOL.

Most common techniques for solving inverse problem are full non-linear inversion techniques, such as: distorted Born iterative method (DBIM) and contrast source inversion (CSI). DBIM needs to be regularized at every iteration. In some cases, it converges to a solution, and, in some cases, it does not. Diffraction tomography does not utilize regularization. It is a technique under Born approximation. It eliminates ill-posedness, but it works only for small contrast. Our proposed method works for high contrast and also provides well-posedness.

In this thesis, our objective is to demonstrate inverse source problem and inverse scattering problem are not inherently ill-posed. They are ill-posed because conventional techniques usually use homogeneous or non-focusing background medium. These mediums do not support separation of scattered field. Utilization of background medium for scattered field separation casts the inverse problem in well-posed form.

Acknowledgements

My heartfelt gratitude is for my advisor, Dr. Vladimir Okhmatovski. I am indebted to him for pushing me to a level I have never been before. Prof. Vladimir Okhmatovski has given me countless hours to guide me through difficulties. This thesis would not be possible without his kind guidance and directions. I also acknowledge my gratitude to Prof. Lotfollah Shafai. He has also been very kind with his guidance and directions. I thank both my advisors for funding my research. This work would not have been possible without the financial support.

I would also like to express my appreciation to Dr. Joe LoVetri for reviewing my thesis. My thanks also go to my friends and colleagues: Stasi, Pedram Mojabi, Cameron Kaye, Mohammad Qudrat-E-Maula, and Mohammad Shafiepour for their continuous support.

Finally, I would like to thank my parents and my wife for their support, patience, and making me feel loved.

Dedication

To my parents, wife, and son.

Contents

Front Matter

Contents	vi
List of Figures	viii

Introduction 1

Mathematical Formulation 10

2.1 Maxwell's Equations.....	10
2.2 Helmholtz equation	12
2.3 Green's function	14
2.4 Integral equation	15

Forward problem 19

3.1 Imaging setup	19
3.2 Technique.....	20
3.3 Green's function calculation using Mie series	21
3.4 Incident field calculation	23
3.5 Total field calculation	27

Inverse problem 29

4.1 Introduction	29
------------------------	----

4.2	Contrast source calculation.....	32
4.3	Volumetric equivalence principle.....	33
4.4	Inverse Problem Ill-posedness: Imaging in Non-focusing vs. Focusing media.....	34
4.5	Comparison of G matrix	36
4.6	Focal width.....	37
Numerical Results for the Inverse Problem		43
5.1	Background variation	45
5.2	Thickness variation	66
5.3	Effect of number of excitation sources	75
5.4	Effect of frequency variation	83
5.5	Higher resolution.....	87
5.6	COMSOL Verification	95
5.7	Noisy data	103
Conclusion and Future work		111
6.1	Conclusion.....	111
6.2	Future work	112

List of Figures

Figure 3.1: Imaging setup: thin slab conformal to 11-layered Maxwell fish-eye lens.....	19
Figure 3.2: Maxwell fish-eye lens discretized with 4 layers of permittivity.....	21
Figure 3.3: Normalized analytic solution of Green’s function with continuous variation of lens’ permittivity from [6] compared with Mie series solution using equation (3.3.1a).....	22
Figure 3.4: Logarithmic electric field norm distribution when a filament current of 1 ampere radiates at 0.0025 meters away from the circumference of the 11-layered Maxwell fish-eye lens.....	23
Figure 3.5: Position of Maxwell fish-eye lens and 400 filament sources in x-y plane.....	24
Figure 3.6: COMSOL simulation result of electric field norm distribution is illustrated, in logarithmic scale, in absence of object of interest when 400 filament sources are evenly placed from 0 to π	25
Figure 3.7: Logarithmic total electric field norm when 400 filament sources located uniformly on an arc spaced from 0 to π are used for interrogation.....	27
Figure 4.1: Conventional setup to excite object of interest. Field values are recorded at positions marked $\mathbf{r}_1, \mathbf{r}_2, \dots, \mathbf{r}_N$	29

Figure 4.2: Maxwell fish-eye lens is used in our proposed method of imaging. The lens is modeled using 11 layers of dielectric. The imaging domain S contains object of interest, the thin slab, placed conformal to the lens. $\mathbf{r}_1, \mathbf{r}_2, \dots, \mathbf{r}_N$ signifies the observation locations.....30

Figure 4.3: Scattered field from different pixels are concentrated over to diametrically opposite side of lens.....34

Figure 4.4: The matrix \mathbf{G} element magnitudes corresponding to the imaging experiment with conventional homogeneous background (condition number $5.4 \cdot 10^{15}$)...35

Figure 4.5: The matrix \mathbf{G} element magnitudes corresponding to the imaging experiment with proposed Maxwell fish-eye lens background (condition number 8.01).....36

Figure 4.6: Focusing width gets narrower with higher $k_b a$40

Figure 5.1: Thin slab conforming to Maxwell fish-eye lens is excited with incident wave in imaging domain S43

Figure 5.2: Real part of object's relative permittivity and its reconstructed values are illustrated with air in homogeneous part of background. Values shown are reconstructed in presence of lens.....45

Figure 5.3: In absence of lens, real part of reconstructed relative permittivity is compared to object's relative permittivity when air is the homogeneous background...46

Figure 5.4: Real part of object's relative permittivity and its reconstructed values are illustrated with relative permittivity 2 in homogeneous part of background. Values shown are reconstructed in presence of lens.....46

Figure 5.5: When imaging experiment is conducted in absence of lens, real part of object's relative permittivity and its reconstructed values are illustrated, provided relative permittivity of homogeneous background is 2.....	47
Figure 5.6: Real part of object's relative permittivity and its reconstructed values are illustrated when homogeneous part of background has relative permittivity 4. Values shown are reconstructed in presence of lens.....	48
Figure 5.7: When imaging experiment is conducted in absence of lens, real part of object's relative permittivity and its reconstructed values are illustrated, provided relative permittivity of homogeneous background is 4.....	49
Figure 5.8: Real part of object's relative permittivity and its reconstructed values are illustrated with relative permittivity 9 in homogeneous part of background. Values shown are reconstructed in presence of lens.....	49
Figure 5.9: When imaging experiment is conducted in absence of lens, real part of object's relative permittivity and its reconstructed values are illustrated, provided relative permittivity of homogeneous background is 9.....	50
Figure 5.10: Real part of object's relative permittivity and its reconstructed values are illustrated with relative permittivity 16 in homogeneous part of background. Values shown are reconstructed in presence of lens.....	51
Figure 5.11: When imaging experiment is conducted in absence of lens, real part of object's relative permittivity and its reconstructed values are illustrated, provided relative permittivity of homogeneous background is 16.....	52

Figure 5.12: Imaginary part of object's relative permittivity and its reconstructed values are illustrated with air in homogeneous part of background. Values shown are reconstructed in presence of lens.....52

Figure 5.13: When imaging experiment is conducted in absence of lens, imaginary part of object's relative permittivity and its reconstructed values are illustrated, provided air is the homogeneous background.....53

Figure 5.14: Imaginary part of object's relative permittivity and its reconstructed values are illustrated with relative permittivity 2 in homogeneous part of background. Values shown are reconstructed in presence of lens.....54

Figure 5.15: When imaging experiment is conducted in absence of lens, real part of object's relative permittivity and its reconstructed values are illustrated, provided relative permittivity of homogeneous background is 2.....55

Figure 5.16: Imaginary part of object's relative permittivity and its reconstructed values are illustrated with relative permittivity 4 in homogeneous part of background. Values shown are reconstructed in presence of lens.....55

Figure 5.17: When imaging experiment is conducted in absence of lens, real part of object's relative permittivity and its reconstructed values are illustrated, provided relative permittivity of homogeneous background is 4.....56

Figure 5.18: Imaginary part of object's relative permittivity and its reconstructed values are illustrated with relative permittivity 9 in homogeneous part of background. Values shown are reconstructed in presence of lens.....57

Figure 5.19: When imaging experiment is conducted in absence of lens, real part of object's relative permittivity and its reconstructed values are illustrated, provided relative permittivity of homogeneous background is 9.....58

Figure 5.20: Imaginary part of object's relative permittivity and its reconstructed values are illustrated with relative permittivity 16 in homogeneous part of background. Values shown are reconstructed in presence of lens.....58

Figure 5.21: When imaging experiment is conducted in absence of lens, real part of object's relative permittivity and its reconstructed values are illustrated, provided relative permittivity of homogeneous background is 16.....59

Figure 5.22: Norm of total electric field variation in the object of interest and reconstructed electric field from inverse problem solution in presence of lens when homogeneous part of background permittivity is 1.....60

Figure 5.23: Norm of total electric field variation in the object of interest and reconstructed electric field from inverse problem solution when homogeneous part of background permittivity is 2.....60

Figure 5.24: Norm of total electric field variation in the object of interest and reconstructed electric field from inverse problem solution when homogeneous part of background permittivity is 4.....61

Figure 5.25: Norm of total electric field variation in the object of interest and reconstructed electric field from inverse problem solution when homogeneous part of background permittivity is 9.....62

Figure 5.26: Norm of total electric field variation in the object of interest and reconstructed electric field from inverse problem solution when homogeneous part of background permittivity is 16.....	63
Figure 5.27: Illustration of error norm per pixel variation in presence of lens when background is varied.....	63
Figure 5.28: Illustration of error norm per pixel variation in absence of lens when background is varied.....	64
Figure 5.29: Norm of total electric field variation in the slab when thickness is 0.005 meters.....	66
Figure 5.30: Norm of total electric field variation in the slab when thickness is 0.025 meters.....	66
Figure 5.31: Norm of total electric field variation in the slab when thickness is 0.05 meters.....	67
Figure 5.32: Norm of total electric field variation in the slab when thickness is 0.1 meters.....	67
Figure 5.33: When slab thickness is 0.005 meters, real part of reconstructed relative permittivity is compared with the exact relative permittivity in presence of the lens.....	68
Figure 5.34: When slab thickness is 0.025 meters, real part of reconstructed relative permittivity is compared with the exact relative permittivity in presence of the lens.....	69

Figure 5.35: When slab thickness is 0.05 meters, real part of reconstructed relative permittivity is compared with the exact relative permittivity in presence of the lens.....	70
Figure 5.36: When slab thickness is 0.1 meters, real part of reconstructed relative permittivity is compared with the exact relative permittivity in presence of the lens.....	70
Figure 5.37: When slab thickness is 0.005 meters, imaginary part of reconstructed relative permittivity is compared with the exact relative permittivity in presence of the lens.....	71
Figure 5.38: When slab thickness is 0.025 meters, imaginary part of reconstructed relative permittivity is compared with the exact relative permittivity in presence of the lens.....	71
Figure 5.39: When slab thickness is 0.05 meters, imaginary part of reconstructed relative permittivity is compared with the exact relative permittivity in presence of the lens.....	72
Figure 5.40: When slab thickness is 0.1 meters, imaginary part of reconstructed relative permittivity is compared with the exact relative permittivity in presence of the lens	73
Figure 5.41: Illustration of error norm per pixel variation in presence of lens when thickness is the varied parameter.....	74
Figure 5.42: Single filament source is used for excitation of the object of interest. The real part of reconstructed relative permittivity is compared to exact relative permittivity.....	75

Figure 5.43: 10 filament sources are used for excitation of the object of interest. The real part of reconstructed relative permittivity is compared to exact relative permittivity.....	76
Figure 5.44: 50 filament sources are used for excitation of the object of interest. The real part of reconstructed relative permittivity is compared to exact relative permittivity.....	76
Figure 5.45: 100 filament sources are used for excitation of the object of interest. The real part of reconstructed relative permittivity is compared to exact relative permittivity.....	77
Figure 5.46: 400 filament sources are used for excitation of the object of interest. The real part of reconstructed relative permittivity is compared to exact relative permittivity.....	78
Figure 5.47: Single filament source is used for excitation of the object of interest. The imaginary part of reconstructed relative permittivity is compared to exact relative permittivity.....	78
Figure 5.48: 10 filament sources are used for excitation of the object of interest. The imaginary part of reconstructed relative permittivity is compared to exact relative permittivity.....	79
Figure 5.49: 50 filament sources are used for excitation of the object of interest. The imaginary part of reconstructed relative permittivity is compared to exact relative permittivity.....	80

Figure 5.50: 100 filament sources are used for excitation of the object of interest. The imaginary part of reconstructed relative permittivity is compared to exact relative permittivity.....	80
Figure 5.51: 400 filament sources are used for excitation of the object of interest. The imaginary part of reconstructed relative permittivity is compared to exact relative permittivity.....	81
Figure 5.52: Error norm per pixel variation is illustrated when the number of sources is varied.....	81
Figure 5.53: When 300 MHz time-harmonic field is used to interrogate object of interest, reconstructed real part of relative permittivity is compared to exact relative permittivity.....	83
Figure 5.54: When 450 MHz time-harmonic field is used to interrogate object of interest, reconstructed real part of relative permittivity is compared to exact relative permittivity.....	83
Figure 5.55: When 600 MHz time-harmonic field is used to interrogate object of interest, reconstructed real part of relative permittivity is compared to exact relative permittivity.....	84
Figure 5.56: When 300 MHz time-harmonic field is used to interrogate object of interest, reconstructed imaginary part of relative permittivity is compared to exact relative permittivity.....	84
Figure 5.57: When 450 MHz time-harmonic field is used to interrogate object of interest, reconstructed imaginary part of relative permittivity is compared to exact relative permittivity.....	85

Figure 5.58: When 600 MHz time-harmonic field is used to interrogate object of interest, reconstructed imaginary part of relative permittivity is compared to exact relative permittivity.....	85
Figure 5.59: Illustration of error norm per pixel variation when different frequencies are employed to reconstruct the object of interest.....	86
Figure 5.60: Norm of Green's function over angular distribution when the resolution is $\frac{\lambda_b}{2}$; where, λ_b is wavelength in homogeneous part of background.....	87
Figure 5.61: When air is in homogeneous part of background, real part of relative permittivity reconstruction is compared to exact relative permittivity.....	88
Figure 5.62: Real part of relative permittivity reconstruction is compared to exact relative permittivity when homogeneous part of background has relative permittivity 2.....	88
Figure 5.63: Real part of relative permittivity reconstruction is compared to exact relative permittivity when homogeneous part of background has relative permittivity 4.....	89
Figure 5.64: Real part of relative permittivity reconstruction is compared to exact relative permittivity when homogeneous part of background has relative permittivity 9.....	90
Figure 5.65: Real part of relative permittivity reconstruction is compared to exact relative permittivity when homogeneous part of background has relative permittivity 16.....	90

Figure 5.66: When air is in homogeneous part of background, imaginary part of relative permittivity reconstruction is compared to exact relative permittivity.....	91
Figure 5.67: Imaginary part of relative permittivity reconstruction is compared to exact relative permittivity when homogeneous part of background has relative permittivity 2.....	91
Figure 5.68: Imaginary part of relative permittivity reconstruction is compared to exact relative permittivity when homogeneous part of background has relative permittivity 4.....	92
Figure 5.69: Imaginary part of relative permittivity reconstruction is compared to exact relative permittivity when homogeneous part of background has relative permittivity 9.....	93
Figure 5.70: Imaginary part of relative permittivity reconstruction is compared to exact relative permittivity when homogeneous part of background has relative permittivity 16.....	93
Figure 5.71: When we attempt to reconstruct permittivity at higher resolution, error norm per pixel variation is illustrated.....	94
Figure 5.72: Real part of reconstructed relative permittivity is compared to exact relative permittivity distribution when homogeneous part of background is air.....	95
Figure 5.73: Real part of reconstructed relative permittivity is compared to exact relative permittivity distribution when homogeneous part of background is 2.....	96
Figure 5.74: Real part of reconstructed relative permittivity is compared to exact relative permittivity distribution when homogeneous part of background is 4.....	96

Figure 5.75: Real part of reconstructed relative permittivity is compared to exact relative permittivity distribution when homogeneous part of background is 9.....	97
Figure 5.76: Real part of reconstructed relative permittivity is compared to exact relative permittivity distribution when homogeneous part of background is 16.....	98
Figure 5.77: Imaginary part of reconstructed relative permittivity is compared to exact relative permittivity distribution when homogeneous part of background is air.....	98
Figure 5.78: Imaginary part of reconstructed relative permittivity is compared to exact relative permittivity distribution when homogeneous part of background is 2.....	99
Figure 5.79: Imaginary part of reconstructed relative permittivity is compared to exact relative permittivity distribution when homogeneous part of background is 4.....	99
Figure 5.80: Imaginary part of reconstructed relative permittivity is compared to exact relative permittivity distribution when homogeneous part of background is 9.....	100
Figure 5.81: Imaginary part of reconstructed relative permittivity is compared to exact relative permittivity distribution when homogeneous part of background is 16.....	101
Figure 5.82: Error norm per pixel variation is illustrated when we confirm our proposed technique using COMSOL.....	101
Figure 5.83: With no noise added, real part of reconstructed relative permittivity is illustrated.....	103

Figure 5.84: When signal-to-noise ratio (SNR) is 20, real part of reconstructed permittivity distribution is compared to true permittivity distribution.....	104
Figure 5.85: Real part of reconstructed permittivity distribution compared to true permittivity distribution when signal-to-noise ratio (SNR) is 10.....	104
Figure 5.86: With signal-to-noise ratio (SNR) set to 5, real part of reconstructed permittivity distribution is illustrated.....	105
Figure 5.87: With no noise added, imaginary part of reconstructed relative permittivity is illustrated.....	106
Figure 5.88: When signal-to-noise ratio (SNR) is 20, imaginary part of reconstructed permittivity distribution is compared to true permittivity distribution.....	107
Figure 5.89: Imaginary part of reconstructed permittivity distribution compared to true permittivity distribution when signal-to-noise ratio (SNR) is 10.....	107
Figure 5.90: With signal-to-noise ratio (SNR) set to 5, imaginary part of reconstructed permittivity distribution is illustrated.....	108
Figure 5.91: Effect of noise on error norm per pixel is illustrated.....	109

Chapter 1

Introduction

Objective of this thesis is to obtain well-posed inverse problem solution using focused background medium. When time-harmonic field is incident on an object of interest, inverse problem solution provides permittivity variation within the object. This reconstruction of material properties is based on the information about the scattered field collected at certain observation locations. The problem of object reconstruction from its scattering characteristics has important applications in geoscience, medicine, security, and many other areas [1]. This process has different names in different disciplines. As such, it is commonly referred to in medicine as “non-invasive technique”, in manufacturing and materials science as “non-destructive testing and evaluation” and in earth science as “geophysical exploration” or “remote sensing” [4].

Inverse problem is typically cast in the form of Fredholm first kind integral equation [1]. In this equation, the domain and range of integral operator do not coincide. In other words the locations where the scattered field is observed are not allowed to be inside the

imaged object. In the cases when the imaging experiment is staged in a homogeneous medium the pertinent first kind integral equation constitutes ill-posedness in the sense of Hadamard [13] due to violation of the stability condition. That is, the small errors in data may result in greatly increased error in the solution. The ill-posedness is commonly treated through regularization [8]. In regularization, typically a constant term is added to the integral operator. The resulting regularized second kind integral equation becomes well-posed, but loses its equivalence to the Maxwell's equations because of the artificial addition of the regularizing constant term. With a judicious choice of the regularization parameter the errors in the solution due to numerical instability and lack of equivalence to Maxwell Equations can be balanced. This error balancing technique is foundational in most schemes for solution of the inverse problem including the regularized least squares method and distorted Born iterative method (aka Gauss-Newton inversion method) [8].

In what follows we overview some of the most common techniques which can be used for numerical solution of the inverse problem and put the technique developed in this thesis in the context of prior art.

We start our overview from the Minimum Norm solution (MNS). The MNS constructs the sought image in terms of such functions that are guaranteed not to include any contribution from the null-space of the pertinent integral operator in the formulation of the inverse problem [16]. Since the MNS by definition does not allow for the null space contributions to be present it spares the solution from having unphysical contributions with unconstrained magnitudes. However, when the MNS method forms a system of lin-

ear algebraic equations with respect to the coefficients of the functions expanding the solution the resultant matrix equation is often in itself is ill-posed due to ill-conditioning of its matrix. As a result, the coefficients of expansion of the sought solution may acquire contributions from the matrix operator null-space. Thus, MNS representation of the solution in terms of functions orthogonal to the null-space of the continuous operator of the integral equation does not guarantee an accurate solution. In practice the MNS method results in reconstruction of contrast sources with relatively poor quality.

Another technique allowing for numerical solution of the inverse problem is the Regularized Least Squares (RLS) method. This method introduces a regularization term that adds diagonal component to the originally ill-conditioned matrix resulting from discretization of the pertinent ill-posed integral equation. The size of the added diagonal term is chosen through the balancing of the error resulting from the ill-conditioning and the error caused by deviation of the solution from the solution of Maxwell Equations. The balance is achieved by plotting the errors due to both of the above mechanisms as functions of the regularization parameter (weight of the added diagonal term) and finding its optimal value balancing the two errors. The method is commonly called ‘L-curve’ due to the shape of the dependence in the two error terms as a function of regularization parameter. The solution resulting from the balancing of the errors is termed as the regularized least-squares solution [4], [17]. In practice, regularized least squares solution is close to minimum norm solution and has a similar quality. Permittivity reconstructed using the MNS and RLS methods is typically not as accurate as the one obtained by full non-linear inver-

sion methods such as the Distorted Born Iterative Method (DBIM) and Contrast Source Inversion (CSI) method.

Alternative technique to the solution of the inverse problem is the Diffraction Tomography method. The method relies on the Born approximation and can cast the inverse problem into the form of a perfectly well-conditioned matrix equation with diagonal matrix. The problem with this method is it works only for lower contrasts between the object of interest and the background medium required by the Born approximation. The description of the method can be found in [18] and [19]. It's important to note here that when the field within the object of interest is similar to incident field, and the Born approximation applies, this method is the method of choice for the solution of the inverse problem. The reason is that this method reconstructs the object with controlled precision limited only by the frequency at which the imaging experiment is conducted. This allows obtaining high-quality image reconstruction by simply increasing the frequency to the level that the level of desired imaged details is comparable to the wavelength of the interrogating field.

When the Born approximation does not hold and the field inside the object is not close to the interrogating field the reconstruction of the object property can be done using Extended Born approximation approach. The method makes an additional modification to the field inside the object by projecting the incident field onto a scattering function. This scattering function is constructed under assumption that the total field within the object of interest varies smoothly. If this is indeed the case, this method allows us to get one step beyond Born approximation in quality of object reconstruction. The requirement of

smooth variation of total field in the object though is typically violated in the practical imaging problems. For example, if the object features a large permittivity discontinuity a rapid field variation may be observed near the material interface. This is demonstrated in various numerical experiments [20]. There are some new approaches where extended Born approximation can be derived without requirement of field smoothness. In the recent work by Prof. Vechi's group at the University of Torino the contrast source inversion (CSI) method is generalized to work under the extended Born approximation without assumption of the field smoothness inside the object. Such method has been shown to present some advantages compared to the standard contrast source inversion (CSI) approach.

Often times the rapid variation of the field inside an object violating requirements of extended Born approximation arises due to proximity of the object to the sources of the interrogating field. To mitigate the effect of the non-smoothness of the field in the object due to closeness of the interrogating sources the modified extended Born approximation method can be used. By an approximation to the Green's function analogous to the extended Born approximation the method allows to negate the effect of rapid variation of field due to close proximity of the interrogating sources.

In the class of imaging techniques reliant on the full non-linear inversion the most popular approaches are the Distorted Born Iterative Method (DBIM) and the Contrast Source Inversion (CSI) method discussed below.

The DBIM technique was first proposed in [21]. It can reconstruct object properties with substantial contrasts to the background medium. The method is iterative in nature and can be shown to be exactly equivalent to the Gauss-Newton optimization technique. The main idea of the DBIM is to attribute prior information about the object to the background and use the corresponding Green's function of that background in the solution of the inverse problem under Born approximation to get an update to the object permittivity. As such the method requires the solution of both the forward scattering problem and the inverse problem at each iteration. The inverse problem of finding an update to the background requires regularization due to its inherent ill-posedness. The inverse problem formulation within this method turns out to be no less ill-posed at each iteration as the initially stated inverse problem. The solution of the ill-posed inverse problem at each iteration is typically found using L-curve approach and Regularized Least Squares method discussed earlier.

Contrast source inversion (CSI) method is getting increasingly popular compared to the DBIM. This is mainly because CSI unlike the DBIM does not require solution of the forward scattering problem at each iteration. In CSI field translations from the object of interest in imaging domain to observation region is calculated at every iteration instead. So, the field translations are found from the sources that we assume to be the right sources at a given iteration. From the difference, we come up with an update to the contrast sources, but we never find total field inside the object based on a given distribution of permittivity that would require solution of the forward scattering problem. The numerical experiments show however that the DBIM converges substantially faster than CSI

and the overall time required for the solution of the inverse problem is comparable in the two methods. The explanation for this fact is that if we were to solve the forward problem in DBIM iteratively the overall number of field translations would be comparable to the number of field translations featured in the CSI method for the solution of the same problem.

In the method proposed in this thesis the inherent ill-posedness of inverse source problem is eliminated without addition of regularizing constant. This is achieved by staging imaging experiment in a media with focusing properties. It concentrates scattered field from distinct regions of the object of interest (pixels) onto different observation locations thus leading to a well-posed formulation of the inverse problem. The required medium is realized by the well-known Maxwell Fish Eye lens. By placing the object in a conformal manner to the lens its scattered field is concentrated at the observation location diametrically opposite to the location of the contrast source of the object. So, upon discretization of the object each of the observation locations has a major contribution from the diametrically opposite pixel of the discretized object. This eliminates ill-posedness of inverse source problem leading to well-conditioned matrix form. Direct inversion provides contrast source values within object of interest. The contrast source values are used to find total field at discretized pixel centers and are subsequently used to determine contrast within the object of interest.

In this thesis, Chapter 2 is composed of mathematical formulation. We start with time-domain Maxwell's equations and obtain frequency-domain Maxwell's equations. It

is followed by Helmholtz equation derivation and its commonly used solution in cylindrical co-ordinate system. In addition, Green's function is introduced. Commonly used solution to Green's function for a filament current in homogeneous background medium is discussed. Also, integral equation, used in method of moment calculation, has been derived.

Chapter 3 describes imaging experiment setup followed by forward problem solving techniques. It also discusses Mie series solution of multi-layered Maxwell fish-eye lens used for finding incident field and total field.

Chapter 4 introduces inverse source problem and contrast source calculation. Volumetric equivalence principle is discussed. This chapter compares conventional imaging to focusing media imaging. The comparison also illustrates diagonal dominance of matrix to be inverted leading to well-conditioned formulation. Also, the focal width of the field in the focusing media is obtained.

Chapter 5 discusses numerical results from inverse problem solution. Studies are conducted by varying lens background, frequency of interrogating time-harmonic field, and number of interrogating sources. Also, numerical results illustrate imaging experiment conducted at higher resolution. In a section of this chapter, we have used COMSOL to verify some of our results validating forward problem solution using Mie series and method of moment.

Chapter 6 concludes our contributions and provides an outline for future work.

Chapter 2

Mathematical Formulation

2.1 Maxwell's Equations

When linear dimensions are assumed to be larger than atomic dimensions and charge magnitudes are assumed to be larger than atomic charges, we view electromagnetic phenomena from the “macroscopic” standpoint [2]. Upon foretold assumptions, Maxwell's equations have strong predictive power of electromagnetic phenomena. In differential form, Maxwell's equations are as follows:

$$\nabla \times \mathbf{E}(\mathbf{r}, t) = -\frac{\partial \mathbf{B}(\mathbf{r}, t)}{\partial t} \quad (2.1.1)$$

$$\nabla \times \mathbf{H}(\mathbf{r}, t) = \frac{\partial \mathbf{D}(\mathbf{r}, t)}{\partial t} + \mathbf{J}(\mathbf{r}, t) \quad (2.1.2)$$

$$\nabla \cdot \mathbf{B}(\mathbf{r}, t) = 0 \quad (2.1.3)$$

$$\nabla \cdot \mathbf{D}(\mathbf{r}, t) = q_v(\mathbf{r}, t) \quad (2.1.4)$$

where, $\mathbf{E}(\mathbf{r}, t)$ is electric field intensity (volts per meter), $\mathbf{H}(\mathbf{r}, t)$ is magnetic field intensity (amperes per meter), $\mathbf{D}(\mathbf{r}, t)$ is electric flux density (coulombs per square meter), $\mathbf{B}(\mathbf{r}, t)$ is magnetic flux density (webers per square meter), $\mathbf{J}(\mathbf{r}, t)$ is electric current density (amperes per square meter), $q_v(\mathbf{r}, t)$ is electric charge density (coulombs per cubic meter). The position vector in (x, y, z) spatial axes is defined as \mathbf{r} . “ $\nabla \times$ ” represents curl operation. “ $\nabla \cdot$ ” represents divergence operation. $\mathbf{J}(\mathbf{r}, t)$ represents summation of the conduction current $\mathbf{J}_c(\mathbf{r}, t)$ and impressed current $\mathbf{J}_i(\mathbf{r}, t)$.

Only two of the four Maxwell’s equations are independent in electrostatics [3]. Thus, we only require the equations (2.1) and (2.2). We have two equations with four unknowns \mathbf{E} , \mathbf{H} , \mathbf{B} and \mathbf{D} . Sufficient number of equations can be achieved using following constitutive relationships:

$$\mathbf{D}(\mathbf{r}, t) = \varepsilon_0 \varepsilon_r(\mathbf{r}) \mathbf{E}(\mathbf{r}, t) \quad (2.1.5)$$

$$\mathbf{B}(\mathbf{r}, t) = \mu_0 \mu_r(\mathbf{r}) \mathbf{H}(\mathbf{r}, t) \quad (2.1.6)$$

where, ε_0 is permittivity of free space $\cong 8.854 \cdot 10^{-12}$ farads per meter, μ_0 is permeability of free space $\cong 4 \pi \cdot 10^{-7}$ henry per meter, μ_r is relative permeability, $\varepsilon_r(\mathbf{r})$ is relative permittivity for isotropic media [3]. There is also a constitutive relationship for a conductor as follows:

$$\mathbf{J}_c(\mathbf{r}, t) = \sigma(\mathbf{r}) \mathbf{E}(\mathbf{r}, t) \quad (2.1.7)$$

The Maxwell’s equations assume $e^{j\omega t}$ time-harmonic dependence, where $j = \sqrt{-1}$ and ω is the angular frequency (radians per second) given by following expression:

$$\omega = 2\pi f$$

where, f is frequency (Hertz). Therefore, in frequency domain, Maxwell's equations become:

$$\nabla \times \mathbf{E}(\mathbf{r}) = -j\omega\mathbf{B}(\mathbf{r}) \quad (2.1.8)$$

$$\nabla \times \mathbf{H}(\mathbf{r}) = j\omega\mathbf{D}(\mathbf{r}) + \mathbf{J}(\mathbf{r}) \quad (2.1.9)$$

$$\nabla \cdot \mathbf{B}(\mathbf{r}) = 0 \quad (2.1.10)$$

$$\nabla \cdot \mathbf{D}(\mathbf{r}) = q_v(\mathbf{r}) \quad (2.1.11)$$

where, $\mathbf{E}(\mathbf{r}, t) = \sqrt{2} \operatorname{Re}\{\mathbf{E}(\mathbf{r}) e^{j\omega t}\}$

Here, $\sqrt{2}$ may be omitted and is a matter of convention [2].

2.2 Helmholtz equation

The term wave is commonly used to denote solution of wave equation [2]. Electro-magnetic waves can be described by the scalar wave equation or Helmholtz equation [2]. The Helmholtz equation can be derived taking curl of equation (2.1.8) and substituting it in equation (2.1.9) for $\nabla \times \mathbf{H}$:

$$\nabla \times \nabla \times \mathbf{E}(\mathbf{r}) - \omega^2 \mu \epsilon \mathbf{E}(\mathbf{r}) = 0 \quad (2.2.1)$$

This is frequency domain form of the vector wave equation for a source-free homogeneous isotropic medium. Using following identity:

$$\nabla \times \nabla \times \mathbf{E} = \nabla(\nabla \cdot \mathbf{E}) - \nabla^2 \mathbf{E} \quad (2.2.2)$$

where, $\nabla \cdot \mathbf{E} = 0$ for a homogeneous source-free medium. Equation (2.2.1) becomes vector Helmholtz equation [2]:

$$\nabla^2 \mathbf{E}(\mathbf{r}) + k^2 \mathbf{E}(\mathbf{r}) = 0 \quad (2.2.3)$$

where, $k^2 = \omega^2 \mu \epsilon$. In a source free, lossless homogeneous medium, rectangular components of \mathbf{E} , that is, E_x, E_y, E_z , satisfy following complex scalar Helmholtz equation [7]:

$$(\nabla^2 + k^2)\psi(\mathbf{r}) = 0 \quad (2.2.4)$$

In cylindrical coordinates, the Helmholtz equation is as follows:

$$\left(\frac{1}{\rho} \frac{\partial}{\partial \rho} \rho \frac{\partial}{\partial \rho} + \frac{1}{\rho^2} \frac{\partial^2}{\partial \phi^2} + \frac{\partial^2}{\partial z^2} + k^2 \right) \psi(\mathbf{r}) = 0 \quad (2.2.5)$$

One of the solutions of Helmholtz equation is of following form [3]:

$$\psi(\mathbf{r}) = F_n(\rho) e^{jn\phi + jk_z z} \quad (2.2.6)$$

where, n is an integer showing the field is 2π periodic in ϕ . Substituting equation (2.2.6) into (2.2.5) results in the expression:

$$\left(\frac{1}{\rho} \frac{\partial}{\partial \rho} \rho \frac{\partial}{\partial \rho} - \frac{n^2}{\rho^2} + k_\rho^2 \right) F_n(\rho) = 0 \quad (2.2.7)$$

where, $k_\rho^2 = k^2 - k_z^2$. Commonly used solution of (2.2.7) is superposition of any two of four special functions. The four special functions are:

- a. the Bessel function: $J_n(k_\rho \rho)$,
- b. the Neumann function: $N_n(k_\rho \rho)$,
- c. the Hankel function of the first kind: $H_n^{(1)}(k_\rho \rho)$,
- d. the Hankel function of the second kind: $H_n^{(2)}(k_\rho \rho)$.

Only two of the four special functions are independent. They are related to each other in following manner:

$$J_n(k_\rho \rho) = \frac{1}{2} [H_n^{(1)}(k_\rho \rho) + H_n^{(2)}(k_\rho \rho)] \quad (2.2.8a)$$

$$N_n(k_\rho \rho) = \frac{1}{2j} [H_n^{(1)}(k_\rho \rho) - H_n^{(2)}(k_\rho \rho)] \quad (2.2.8b)$$

or

$$H_n^{(1)}(k_\rho \rho) = J_n(k_\rho \rho) + j N_n(k_\rho \rho) \quad (2.2.8c)$$

$$H_n^{(2)}(k_\rho \rho) = J_n(k_\rho \rho) - j N_n(k_\rho \rho) \quad (2.2.8d)$$

2.3 Green's function

Solution of Helmholtz equation for a point source is known as the Green's function [3]. Using principle of superposition, solution due to a general source can be obtained. A general source can be represented by a superposition of point sources. To obtain solution of following scalar wave equation:

$$(\nabla^2 + k^2)\psi(\mathbf{r}) = s(\mathbf{r}) \quad (2.3.1)$$

at first, we seek the Green's function by finding solution of the following equation:

$$(\nabla^2 + k^2)g(\mathbf{r}, \mathbf{r}') = \delta(\mathbf{r} - \mathbf{r}') \quad (2.3.2)$$

When equation (2.3.2) is solved, we have $g(\mathbf{r}, \mathbf{r}')$ [3]. $\psi(\mathbf{r})$ can be found easily from the principle of superposition. Since principle of superposition for source $s(\mathbf{r})$ states:

$$s(\mathbf{r}) = \int_S s(\mathbf{r}') \delta(\mathbf{r} - \mathbf{r}') d\mathbf{r}' \quad (2.3.3)$$

$\psi(\mathbf{r})$ can be expressed by the following expression:

$$\psi(\mathbf{r}) = \int_S g(\mathbf{r}, \mathbf{r}') s(\mathbf{r}') d\mathbf{r}' \quad (2.3.4)$$

To obtain Green's function of a line source located at the origin, let us consider following scalar wave equation:

$$\left(\frac{\partial^2}{\partial x^2} + \frac{\partial^2}{\partial y^2} + k^2 \right) \varphi(x, y) = \delta(x)\delta(y) \quad (2.3.5)$$

Using cylindrical symmetry of the problem, i.e. $n = 0$ in equation 2.2.7, we can rewrite equation (2.3.5) in cylindrical coordinates as follows:

$$\left[\frac{\partial^2}{\partial \rho^2} + \frac{1}{\rho} \frac{\partial}{\partial \rho} + k^2 \right] \varphi(\rho) = \delta(\rho) \quad (2.3.6)$$

where, $\delta(\rho) = \delta(x)\delta(y)$. With $e^{j\omega t}$ time dependence and satisfying radiation condition, one of the solutions of an outgoing wave is Hankel function of the second kind [7]. Therefore, one of the solutions can be written as follows:

$$\varphi(\rho) = CH_0^{(2)}(k\rho)$$

Value of constant C can be found by matching singularity of Hankel function at $\rho = 0$ [3]. Hence the solution is the following expression:

$$\varphi(\rho) = -\frac{1}{4j}H_0^{(2)}(k\rho) \quad (2.3.7)$$

Considering translational invariance of the Green's function the above solution can be rewritten for arbitrary location of the source point $\boldsymbol{\rho}'$ and observation point $\boldsymbol{\rho}$ as follows:

$$\varphi(\boldsymbol{\rho}, \boldsymbol{\rho}') = -\frac{1}{4j}H_0^{(2)}(k|\boldsymbol{\rho} - \boldsymbol{\rho}'|) \quad (2.3.8)$$

2.4 Integral equation

Scattering solution of an inhomogeneous object can be obtained using volume integral equation [3]. The unknowns are expressed in terms of volume polarization current flowing in the inhomogeneous medium. The volume current is summation of conduction current and the displacement current induced by total electric field [3]. An integral equa-

tion is formulated as outlined below. Taking curl of equation (2.1.8) results in the equation below:

$$\nabla \times \nabla \times \mathbf{E} = -j\omega\mu\nabla \times \mathbf{H} \quad (2.4.1)$$

Substituting equation (2.1.9) in equation (2.4.1) results in following expression:

$$\nabla \times \nabla \times \mathbf{E} = \omega^2\mu\varepsilon\mathbf{E} - j\omega\mu\mathbf{J}$$

Using the vector calculus identity written below:

$$\nabla \times \nabla \times \mathbf{A} = -\nabla^2\mathbf{A} + \nabla(\nabla \cdot \mathbf{A})$$

the equation results in the following equation:

$$-\nabla^2\mathbf{E} + \nabla(\nabla \cdot \mathbf{E}) - k^2\mathbf{E} = -j\omega\mu\mathbf{J} \quad (2.4.2)$$

where, $k^2 = \omega^2\mu\varepsilon$. From continuity equation [7], we have the following expression:

$$\nabla \cdot \mathbf{J} = -j\omega q_v$$

$$\text{or, } q_v = \frac{j}{\omega}(\nabla \cdot \mathbf{J}) \quad (2.4.3)$$

From equation (2.1.11) we know the relationship shown below:

$$\nabla \cdot \mathbf{D}(\mathbf{r}) = q_v(\mathbf{r})$$

Substituting equation (2.4.3) gives rise to:

$$\nabla \cdot \varepsilon\mathbf{E} = \frac{j}{\omega}(\nabla \cdot \mathbf{J}) = \frac{j}{\omega}(\nabla \cdot (\mathbf{J}^e + \mathbf{J}^c))$$

where, \mathbf{J}^c is conduction current and \mathbf{J}^e is impressed current. So, the equation becomes:

$$\nabla \cdot \varepsilon\mathbf{E} - \frac{j}{\omega}(\nabla \cdot \sigma\mathbf{E}) = \frac{j}{\omega}(\nabla \cdot \mathbf{J}^e)$$

$$\text{or, } \nabla \cdot (-j\omega\varepsilon - \sigma)\mathbf{E} = \nabla \cdot \mathbf{J}^e$$

$$\text{or, } -\nabla \cdot (\hat{\sigma}\mathbf{E}) = \nabla \cdot \mathbf{J}^e$$

where, $\hat{\sigma} = j\omega\varepsilon + \sigma$

$$\text{or, } -[\hat{\sigma}(\nabla \cdot \mathbf{E}) + \mathbf{E} \cdot (\nabla \hat{\sigma})] = \nabla \cdot \mathbf{J}^e$$

$$\text{or, } \nabla \cdot \mathbf{E} = -\mathbf{E} \cdot \frac{\nabla \hat{\sigma}}{\hat{\sigma}} - \frac{1}{\hat{\sigma}} \nabla \cdot \mathbf{J}^e \quad (2.4.4)$$

Substituting value from equation (2.4.4) in equation (2.4.2) results in following equation:

$$\nabla^2 \mathbf{E} + \nabla \left(\frac{\nabla \hat{\sigma}}{\hat{\sigma}} \cdot \mathbf{E} \right) + k^2 \mathbf{E} = j\omega\mu \mathbf{J}^e - \nabla \left(\frac{1}{\hat{\sigma}} \nabla \cdot \mathbf{J}^e \right)$$

For homogeneous lossless medium, the expression simplifies to:

$$\nabla^2 \mathbf{E} + k^2 \mathbf{E} = j\omega\mu \mathbf{J}^e \quad (2.4.5)$$

With no variation in z axis, that is, $\frac{\partial}{\partial z} = 0$, for transverse magnetic (TM) scattering problem, equation (2.4.5) can be written down as following three complex scalar equations:

$$\nabla^2 E_x + k^2 E_x = 0 \quad (2.4.6a)$$

$$\nabla^2 E_y + k^2 E_y = 0 \quad (2.4.6b)$$

$$\nabla^2 E_z + k^2 E_z = j\omega\mu J_z^e \quad (2.4.6c)$$

In case of 2D point source excitation equation (2.4.6c) becomes:

$$\nabla^2 E_z + k^2 E_z = j\omega\mu I_z^e \delta(z - z') \quad (2.4.6d)$$

As we have already discussed in section 2.3, the solution of the equation below:

$$(\nabla^2 + k_0^2)g(\mathbf{r}, \mathbf{r}') = \delta(\mathbf{r} - \mathbf{r}') \quad (2.4.7)$$

is given by following expression [7]:

$$g(\mathbf{r}, \mathbf{r}') = -\frac{1}{4j} H_0^{(2)}(k|\mathbf{r} - \mathbf{r}'|) \quad (2.4.8)$$

Rewriting (2.4.6c) in the form matching in its left hand side the operators of equation (2.4.7) as given below:

$$\nabla^2 E_z + k_0^2 E_z = j\omega\mu I_z^e \delta(z - z') + (k_0^2 - k^2)E_z \quad (2.4.9)$$

We can use the principle of superposition to obtain solution of equation (2.4.6c) as follows:

$$E_z(\mathbf{r}) = \int_{S'} g(\mathbf{r}, \mathbf{r}') (j\omega\mu J_z^e) d\mathbf{r}' + \int_S g(\mathbf{r}, \mathbf{r}') (k^2 - k_0^2) E_z(\mathbf{r}') d\mathbf{r}' \quad (2.4.10)$$

In equation (2.4.10), S' signifies source region outside domain S . The equation becomes:

$$E_z = E_i + E_s \quad (2.4.11)$$

where, E_z is total field, E_i is incident field, and E_s is scattered field. The incident field and scattered field are given by following expressions:

$$E_i(\mathbf{r}) = \int_{S'} g(\mathbf{r}, \mathbf{r}') (j\omega\mu J_z^e) d\mathbf{r}' \quad (2.4.12)$$

$$E_s(\mathbf{r}) = \int_S g(\mathbf{r}, \mathbf{r}') (k^2 - k_0^2) E_z(\mathbf{r}') d\mathbf{r}' \quad (2.4.13)$$

It can be further simplified to the equation below:

$$E(\mathbf{r}) = E_i(\mathbf{r}) + \int_S g(\mathbf{r}, \mathbf{r}') O(\mathbf{r}') E_z(\mathbf{r}') d\mathbf{r}' \quad (2.4.14)$$

where, $O(\mathbf{r}') = \omega^2\mu [\varepsilon(\mathbf{r}') - \varepsilon_b] = k^2(\mathbf{r}') - k_b^2$

In this chapter, we have presented Maxwell's equations and constitutive relationships. From these equations, we derive Helmholtz equation. We have presented common solutions of the Helmholtz equation in cylindrical coordinates. In addition, we introduced Green's function. We have also derived the integral equation used to find total field within the object of interest using method of moment, i.e. equation (2.4.14).

Chapter 3

Forward problem

3.1 Imaging setup

In this thesis, we have chosen a very thin slab of dielectric material as an object of interest. Our goal is to reconstruct permittivity variation within the object of interest along its length. Maxwell fish-eye lens is utilized as a background medium to cast the pertinent inverse problem into well-posed form. Object of interest is a thin slab conformal to lens shape as shown in Figure 3.1. To achieve better illustration, the figure shows thicker slab than that used in the numerical experiments. In all our experiments, we use 11-layer realization of the Maxwell fish-eye lens unless otherwise mentioned.

3.2 Technique

Numerical experiment setup has been discussed in section 3.1. In the provided experimental setup, we need to know field values at certain observation locations. Forward problem solution provides us field values at observation locations.

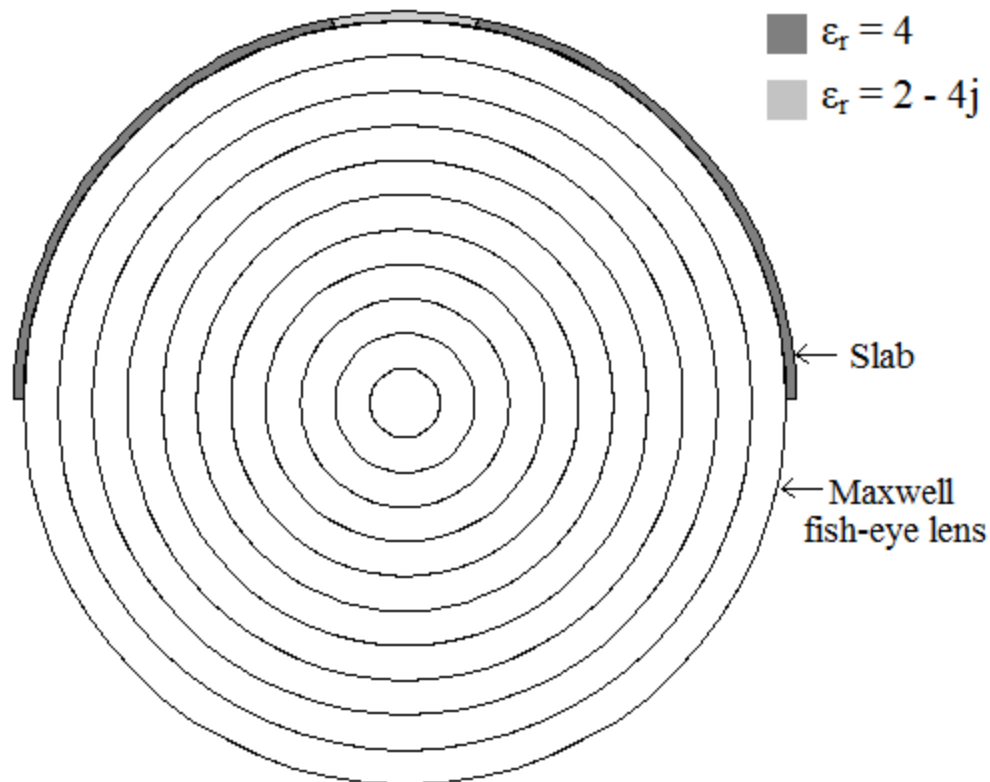


Figure 3.1: Imaging setup: thin slab conformal to 11-layered Maxwell fish-eye lens.

Forward scattering problem solution can be obtained in both time-domain and frequency-domain. Our forward problem solution is calculated in frequency-domain. There are many numerical techniques to solve the forward problem, for example: method of moments, finite element method, finite difference method and others. We use method of

moment [5] for its simplicity of implementation. In this method, we require Green's function computation for Maxwell fish-eye lens. The Mie series solution for the fields in cylindrical layered medium is utilized to obtain the Maxwell fish-eye lens Green's function as explained in section 3.3 below.

3.3 Green's function calculation using Mie series

Maxwell fish-eye lens' Green's function is calculated using Mie series. In our numerical experiment, we model the lens with 11 layers of permittivity defined by [6]:

$$\varepsilon(\rho) = [2/(1 + (\rho/a)^2)]^2 \cdot \varepsilon_b \quad (3.3.1)$$

where, a is lens radius, ε_b is background dielectric, and ρ is distance from lens center. Solution is sought for a 1 Ampere filament current positioned parallel to z-axis at a distance half of slab thickness away from lens circumference. The value of E_z is found from:

$$E_z = -j\omega\mu A_z \quad (3.3.1a)$$

where,

$$A_z = \frac{I_z}{4j} \left[\sum_{n=-\infty}^{\infty} e^{-jn(\phi-\phi')} R_n(\rho) + \begin{cases} H_0^{(2)}(k_b\rho); & \text{if } \rho > a \\ 0; & \text{otherwise} \end{cases} \right]$$

a is lens radius; ρ is observation location distance from lens center; ϕ is observation point angle; ϕ' is source point angle; k_b is wavenumber in homogeneous part of background; and $H_0^{(2)}$ is Hankel function of the second kind of order zero as discussed in section 2.2. We present here Mie series solution of 4-layered Maxwell fish-eye lens solution to conserve space. The lens we demonstrate solution for is illustrated in Figure 3.2.

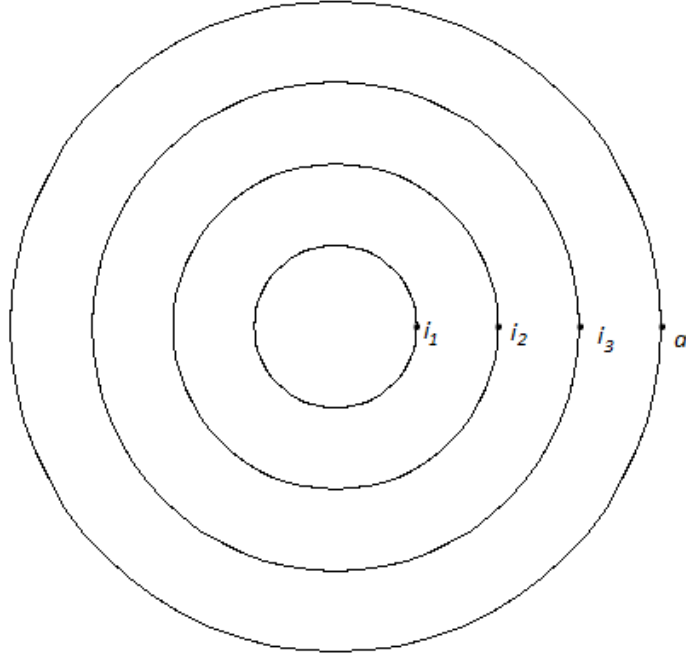


Figure 3.2: Maxwell fish-eye lens discretized with 4 layers of permittivity.

Here,

$$R_n(\rho) = \begin{cases} C_1 J_n(k_1 \rho); & \text{if } 0 \leq \rho \leq i_1 \\ C_{2a} H_n^{(1)}(k_2 \rho) + C_{2b} H_n^{(2)}(k_2 \rho); & \text{if } i_1 < \rho \leq i_2 \\ C_{3a} H_n^{(1)}(k_3 \rho) + C_{3b} H_n^{(2)}(k_3 \rho); & \text{if } i_2 < \rho \leq i_3 \\ C_{4a} H_n^{(1)}(k_4 \rho) + C_{4b} H_n^{(2)}(k_4 \rho); & \text{if } i_3 < \rho \leq a \\ C_5 H_n^{(2)}(k_b \rho); & \text{if } \rho > a \end{cases}$$

where,

$C_1, C_{2a}, C_{2b}, C_{3a}, C_{3b}, C_{4a}, C_{4b}$ and C_5 refer to appropriate coefficients for following boundary conditions at every interface, i_1, i_2, i_3 , and a :

$$\lim_{\Delta\rho \rightarrow 0} \frac{dR_n}{d\rho} + \Delta\rho = \lim_{\Delta\rho \rightarrow 0} \frac{dR_n}{d\rho} - \Delta\rho$$

$$\lim_{\Delta\rho \rightarrow 0} R_n + \Delta\rho = \lim_{\Delta\rho \rightarrow 0} R_n - \Delta\rho$$

Normalized Green's function calculated using Mie series for discretized Maxwell fish-eye lens is compared to analytic Green's function for continuous permittivity distribution [6] is illustrated in Figure 3.3. COMSOL simulation of this setting is illustrated in Figure 3.4. This figure shows logarithmic electric field variation in x-y plane.

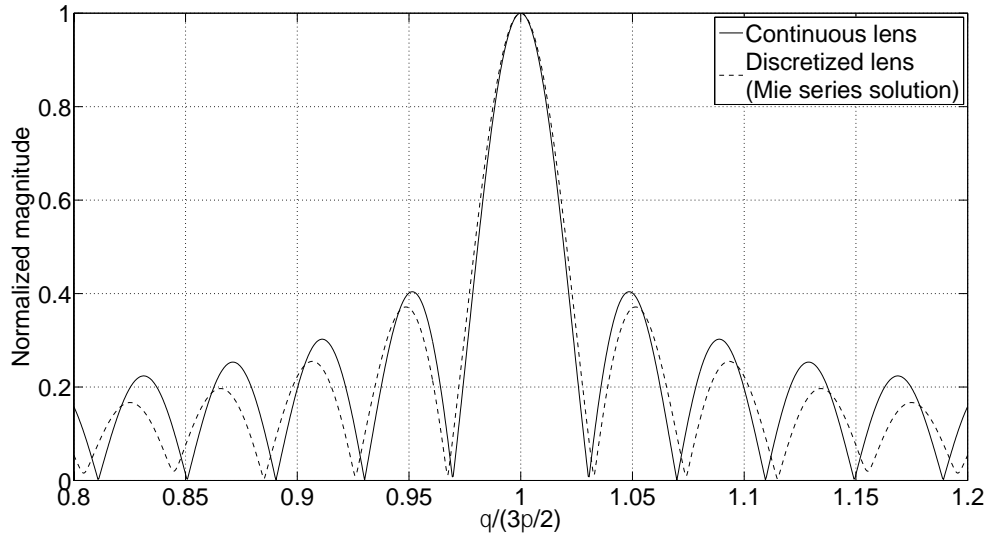


Figure 3.3: Normalized analytic solution of Green's function with continuous variation of lens' permittivity from [6] compared to Mie series solution with discretized Maxwell fish-eye lens using equation (3.3.1a).

3.4 Incident field calculation

In electromagnetic scattering, incident field refers to field in absence of object of interest [2]. Forward problem is solved for two different situations: in absence of object of

interest and in presence of object of interest. These values are used to calculate scattered field as shown below:

$$E_s = E_t - E_i$$

where, E_s is scattered electric field, E_t is total electric field, and E_i is incident field.

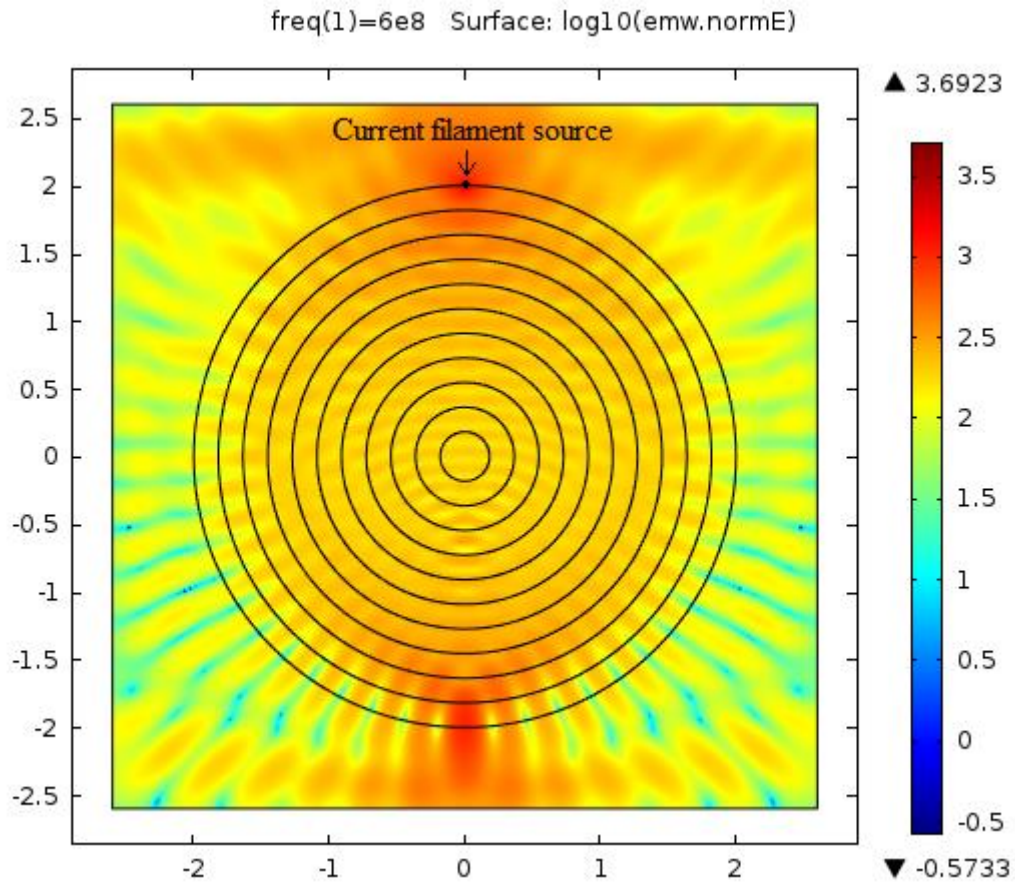


Figure 3.4: Logarithmic electric field magnitude distribution when a filament current of 1 ampere radiates at 2.5 mm away from the circumference of the 11-layered Maxwell fish-eye lens.

A lens radius of 2 meters and slab thickness of 0.005 meters is used. We have placed 400 filament current sources parallel to z axis at a distance of 0.5 meters away from the circumference of the lens evenly on an arc extending from 0 to π as shown in Figure 3.5.

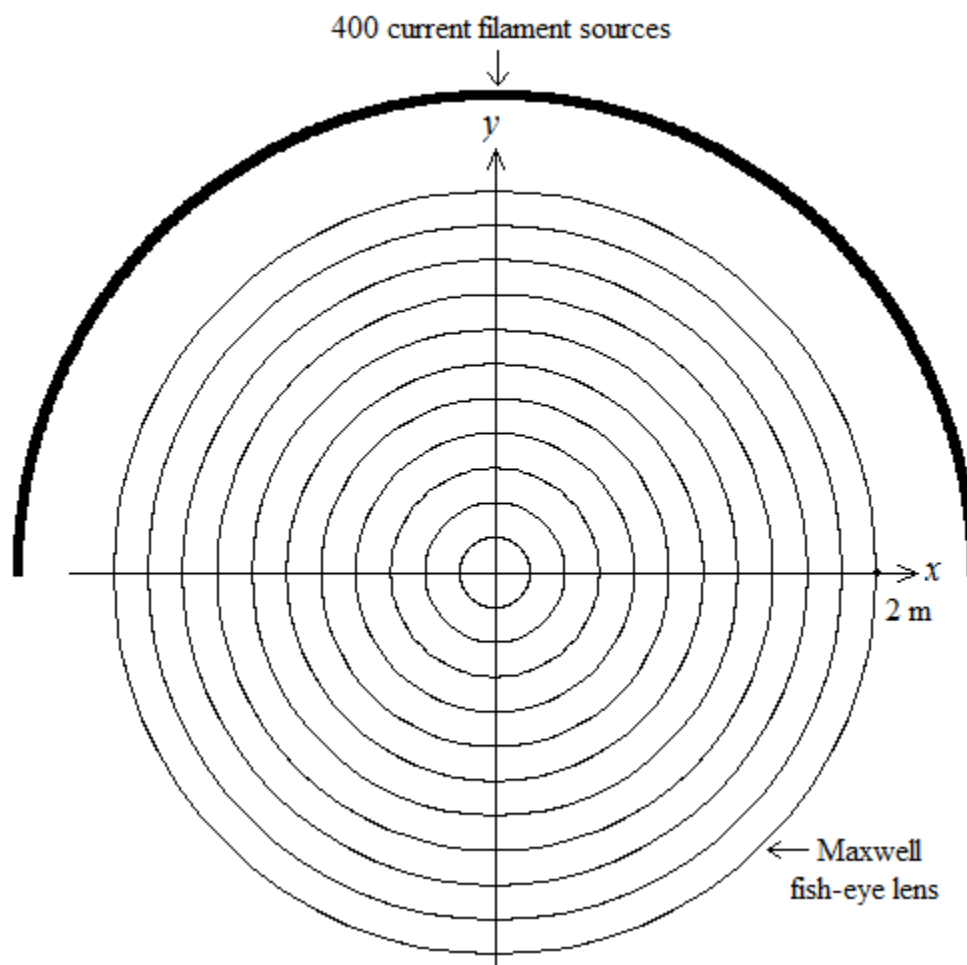


Figure 3.5: Position of Maxwell fish-eye lens and 400 filament sources in x - y plane.

At first, we calculate electric field in absence of object of interest. Observation points are located diametrically opposite to pixel locations. We use Mie series to find field value at observation locations when the sources are positioned 0.5 meters away from lens sur-

face. This value of electric field is denoted as “incident field”, E_i . Figure 3.6 shows COMSOL simulation result demonstrating incident field distribution in x-y plane.

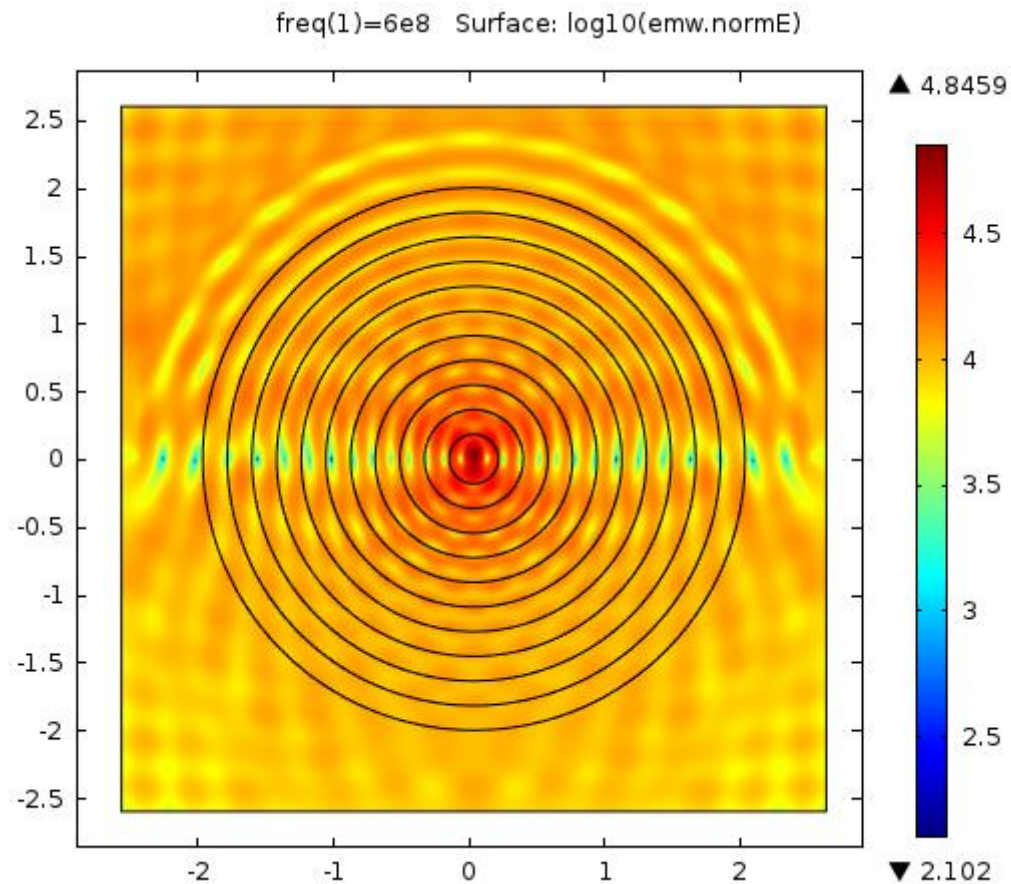


Figure 3.6: COMSOL simulation result of electric field norm distribution is illustrated, in logarithmic scale, in absence of object of interest when 400 filament sources are evenly placed from 0 to π .

3.5 Total field calculation

We use method of moment to find total field. At first, we discretize object of interest into P pixels. Each pixel has a length of $\frac{\lambda_b}{2}$, where, λ_b is wavelength in homogeneous part of background. As described by Richmond in [5], integral equation (2.4.11) can be discretized to form a system of linear algebraic equations in the form:

$$\sum_{n=1}^P C_{mn} \cdot E_n = E_m^i; m = 1, 2, \dots, P$$

C_{mn} is a P by P matrix of known values, E_n is a P by 1 vector of unknown total field values, and E^i is also a P by 1 vector of known coefficients containing incident field. Figure 3.7 shows COMSOL simulation of total field norm variation, in logarithmic scale.

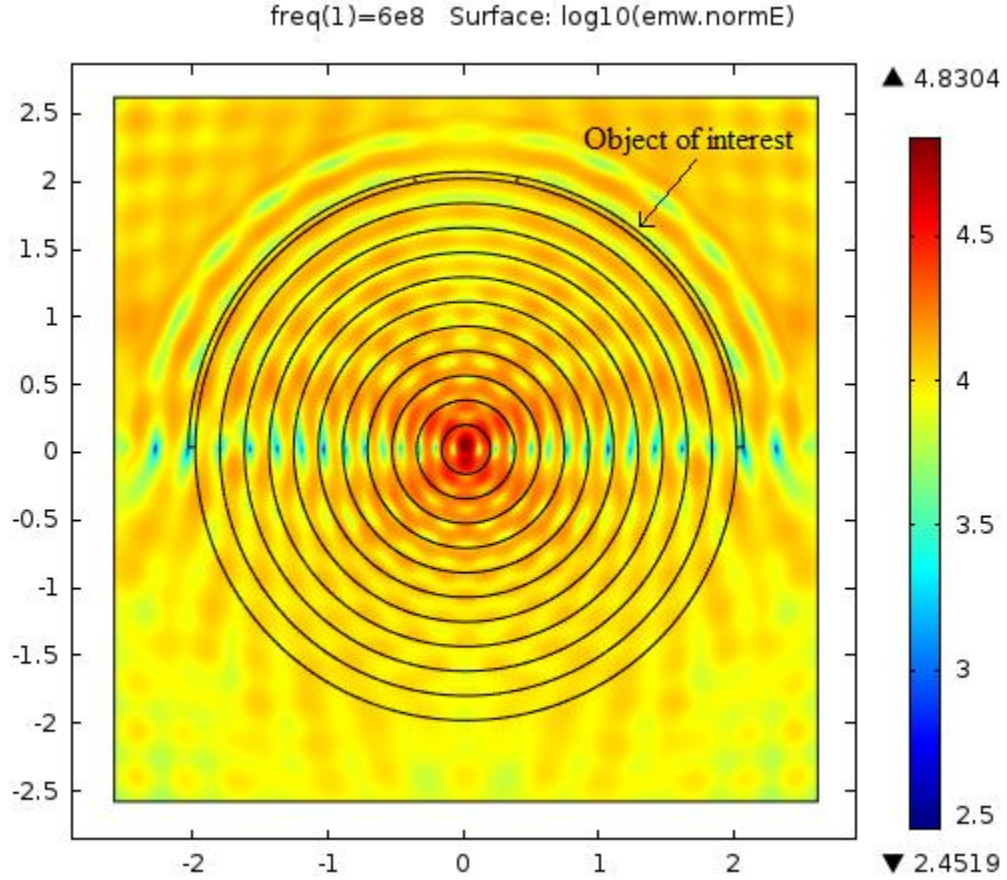


Figure 3.7: Logarithmic total electric field norm when 400 filament sources located uniformly on an arc spaced from 0 to π are used for interrogation.

In this chapter, we have discussed imaging setup for our proposed method. We have also discussed method of moment technique to solve forward problem. Green's function calculation using Mie series for cylindrically symmetric Maxwell fish-eye lens has been explained in detail. The incident field and total field calculation has been also discussed. This chapter has detailed on forward problem solutions. We use these solutions to solve for inverse problem as discussed in Chapter 4.

Chapter 4

Inverse problem

4.1 Introduction

Inverse problem solution predicts internal construction of an object of interest. In conventional imaging method, inverse problem is ill-posed. Conventional experiment setup for solving inverse problem is shown in Figure 4.1. Our proposed method of inverse problem solution casts it into a well-posed form. In our method, Maxwell fish-eye lens provides focused Green's function necessary for elimination of inverse problem ill-posedness. This setup is shown in Figure 4.2. The object of interest is the thin slab placed conformal to the lens.

As Figure 4.2 illustrates, filament sources I_1, I_2, \dots, I_{21} produce excitation. When the slab is absent, field collected at distinct observation locations is known as incident field.

The figure illustrates 21 sources for presentation clarity. Numerical results, presented in Chapter 5, have 400 filament sources unless mentioned otherwise. The filament sources are 0.5 meters away from lens circumference. We collect total field in presence of object of interest. It should be noted that Figure 4.2 shows a thicker slab compared to numerical experiment slab thickness. This is done for presentation clarity. Subsequently, scattered field is calculated from equation (2.4.11):

$$E_t = E_i + E_s$$

where, E_i is incident field with object of interest absent, E_t is total field when object of interest is present, and E_s is scattered field.

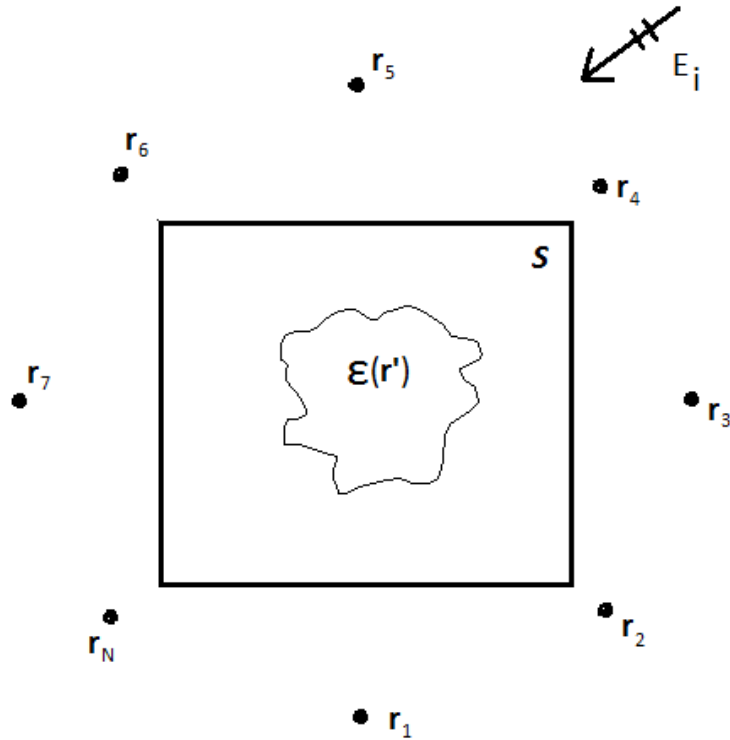


Figure 4.1: Conventional setup to excite object of interest. Field values are recorded at positions marked r_1, r_2, \dots, r_N .

As derived in Chapter 2 in equation (2.4.14), scattered field produced by contrast sources W is calculated as shown below:

$$E_s = k_0^2 \int_S G(\mathbf{r}, \mathbf{r}') W(\mathbf{r}') d\mathbf{r}' \quad (4.1.1)$$

where, $G(\mathbf{r}, \mathbf{r}')$ is Green's function of background medium, and $W(\mathbf{r}')$ is contrast source given by the following expression:

$$W(\mathbf{r}') = [\varepsilon(\mathbf{r}') - \varepsilon_b] E(\mathbf{r}') \quad (4.1.2)$$

Our primary goal is to find W . Details of the procedure is discussed in section 4.2.

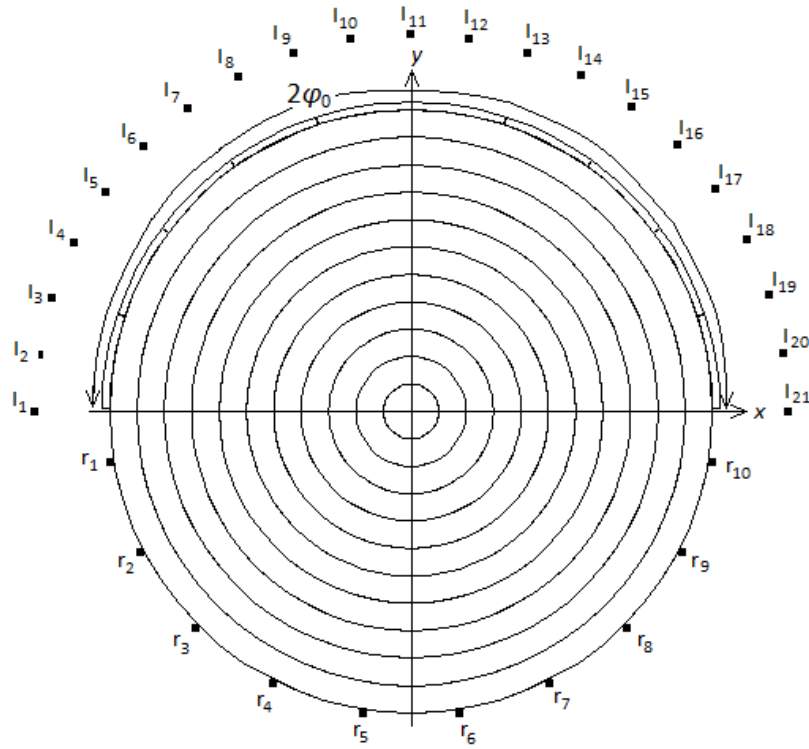


Figure 4.2: Maxwell fish-eye lens is used in our proposed method of imaging. The lens is modeled using 11 layers of dielectric. The imaging domain S contains object of interest, the thin slab, placed conformal to the lens. r_1, r_2, \dots, r_N signifies the observation locations.

4.2 Contrast source calculation

We discretize $W(\phi')$ on the interval $\phi' \in [\frac{\pi}{2} - \phi_0, \frac{\pi}{2} + \phi_0]$ with P piece-wise basis functions $b_p(\phi')$. Angular width of each basis function is $\Delta\phi = \frac{2\phi_0}{P}$ centered at angular locations $\phi_p = \frac{\pi}{2} - \phi_0 + \Delta\phi (p - \frac{1}{2})$. Contrast source W with P piece-wise basis functions can be written in discretized form as follows:

$$W(\phi') = \chi(\phi')E(\phi') \cong \sum_{p=1}^P \chi_p E_p b_p(\phi') = \sum_{p=1}^P W_p b_p(\phi') \quad (4.2.1)$$

where, $b_p(\phi')$ is 1, when $\phi' \in [\phi_n - \frac{\Delta\phi}{2}, \phi_n + \frac{\Delta\phi}{2}]$ and is 0 otherwise. Contrast, $\chi(\phi') = \varepsilon(\phi') - \varepsilon_b$, is the function to be found. Substituting equation (4.2.1) into equation (4.1.1), we get a set of linear algebraic equations in matrix form as follows:

$$\mathbf{G} \cdot \mathbf{W} = \mathbf{E} \quad (4.2.3)$$

where, \mathbf{E} is a P by 1 vector of scattered field, \mathbf{W} is a P by 1 vector of unknown contrast source values, and \mathbf{G} is a P by P matrix defined by:

$$G_{pp'} = k_0^2 \int_{\phi_{p'} - \frac{\Delta\phi}{2}}^{\phi_{p'} + \frac{\Delta\phi}{2}} G(\phi_p - \phi') d\phi'; \quad p, p' = 1, 2, \dots, P \quad (4.2.4)$$

Integral in equation (4.2.4) contains singularity. To evaluate it numerically, the singularity is extracted. Extracted singularity is evaluated analytically according to technique described in [14]. The residual non-singular part is evaluated using Gauss-Legendre quadrature rule.

From direct inversion of \mathbf{G} , contrast source samples \mathbf{W} can be found at P discrete locations. In order to find \mathbf{W} , system of equations needs to be invertible [13]. Typically, \mathbf{G}

is ill-conditioned, however in such scenarios, regularization must be applied in order to invert \mathbf{G} [8]. In section 4.4 of this Chapter, we show how to make the system of equations well-conditioned without resorting to regularization. When \mathbf{G} is well-conditioned, \mathbf{W} can be found via direct inversion of \mathbf{G} . Using volumetric equivalence principle, we can subsequently find contrast χ if \mathbf{W} has been found as described in the following section.

4.3 Volumetric equivalence principle

When contrast sources, \mathbf{W} , are known, volumetric equivalence principle can be applied to relate contrast source to total field within object of interest. This can be expressed as:

$$E_t(\mathbf{r}) = E_i(\mathbf{r}) + k_0^2 \int_S W(\mathbf{r}') G(\mathbf{r}, \mathbf{r}') d\mathbf{r}'; \quad \mathbf{r} \in S \quad (4.3.1)$$

where, E_i is incident field, E_t is total field, and S signifies imaging domain. As shown in Figure 4.2, the thin slab is the imaging domain in our case. When W is known, we can find electric field samples at centroids of basis function elements. The discretized contrast, χ , is obtained from the following relation:

$$\chi(\mathbf{r}') = \frac{W(\mathbf{r}')}{E(\mathbf{r}')} ; \quad \mathbf{r}' \in S$$

To find total field E_p at each pixel center, the contrast source coefficients of equation (4.2.1) are substituted in equation (4.3.1) as given below:

$$E_p = E(\phi_p) = E_i(\phi_p) + k_0^2 \sum_{p'=1}^P W_{p'} \int_{\phi_p - \phi_0}^{\phi_p' + \phi_0} G(\phi_p - \phi') d\phi' \quad (4.3.2)$$

Dividing contrast source values W_p with respective values of E_p gives us:

$$\chi_p = \frac{W_p}{E_p}; p = 1, 2, \dots, P$$

We can obtain dielectric distribution, ε_p by:

$$\varepsilon_p = \chi_p + \varepsilon_b; p = 1, 2, \dots, P$$

where, ε_b is homogeneous part of background permittivity.

4.4 Inverse Problem Ill-posedness: Imaging in Non-focusing vs. Focusing media

In conventional inverse problems, Green's function is non-directional. This leads to ill-conditioning of matrix \mathbf{G} defined in equation (4.2.4). Ill-conditioned matrix \mathbf{G} produces non-unique solution of matrix equation (4.2.3), and, as a result, non-unique solution of inverse problem is obtained as well. Conventional method of eliminating ill-conditioning in inverse problem is through regularization [8]. One of the methods is to artificially add a diagonal matrix to \mathbf{G} before inversion as shown below:

$$(\alpha \mathbf{I} + \mathbf{G}) \cdot \mathbf{W} = \mathbf{E} \quad (4.4.1)$$

where, \mathbf{I} is an identity matrix. Regularization parameter α makes \mathbf{G} diagonally dominant. Hence, $(\alpha \mathbf{I} + \mathbf{G})$ can be made well-conditioned by taking a sufficiently large parameter α . The larger is regularization parameter α , however, the further is our solution from true

solution dictated by Maxwell's equations. In [1], a different approach is presented to obtain well-conditioned \mathbf{G} when scattered field from object's different pixels is concentrated at distinct locations. Our approach also concentrates scattered field from separate pixels onto diametrically opposite side of lens as illustrated by Figure 4.3. This increases diagonal component of \mathbf{G} significantly and without artificial addition of the regularization term. Hence, \mathbf{G} becomes well conditioned.

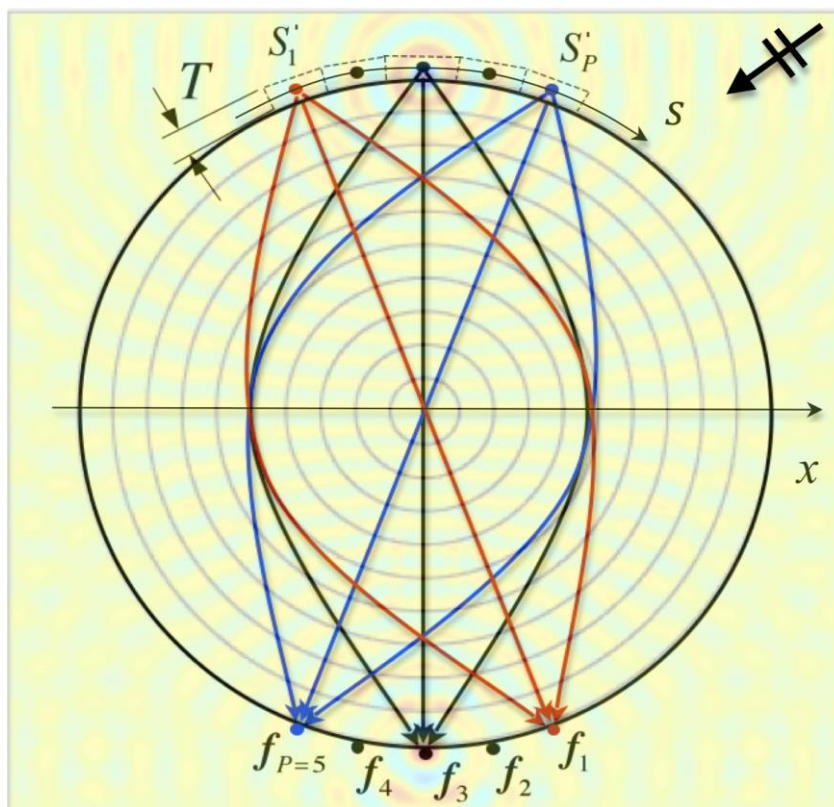


Figure 4.3: Scattered field from different pixels are concentrated over to diametrically opposite side of lens.

4.5 Comparison of \mathbf{G} matrix

In conventional imaging method, homogeneous background is used. Figure 4.4 illustrates matrix \mathbf{G} formed using equation (4.2.4) for conventional imaging method. On the other hand, our proposed method utilizes Maxwell fish-eye lens as the background medium forming desired focused Green's function. The \mathbf{G} matrix shown in Figure 4.5 is created from our proposed method of imaging in the presence of Maxwell fish-eye lens. In both cases, homogeneous part of background has relative permittivity 9. Figure 4.5 shows diagonally dominant matrix \mathbf{G} . It is a 75 by 75 matrix with condition number 8.01. If this experiment is conducted in a homogeneous background, in absence of lens, condition number of matrix \mathbf{G} is $5.4 \cdot 10^{15}$, making matrix inversion impossible. Hence, if imaging experiment is conducted in homogeneous background, non-unique solution is obtained.

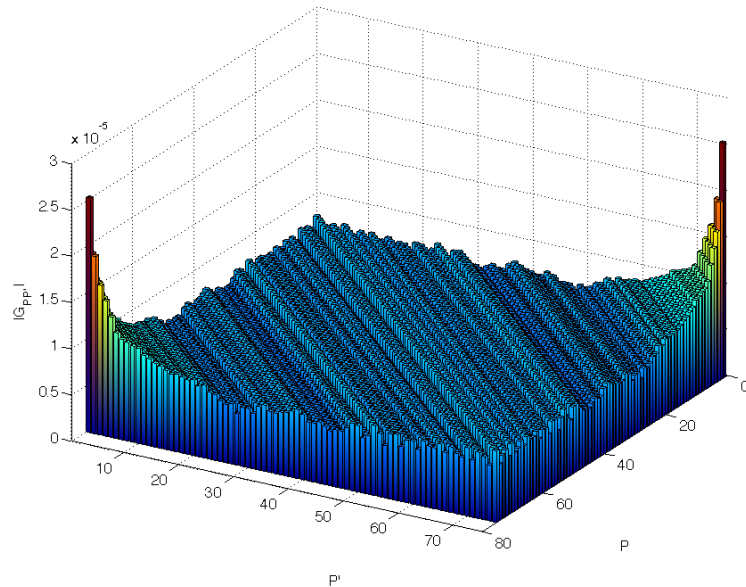


Figure 4.4: The matrix \mathbf{G} element magnitudes corresponding to the imaging experiment with conventional homogeneous background (condition number $5.4 \cdot 10^{15}$).

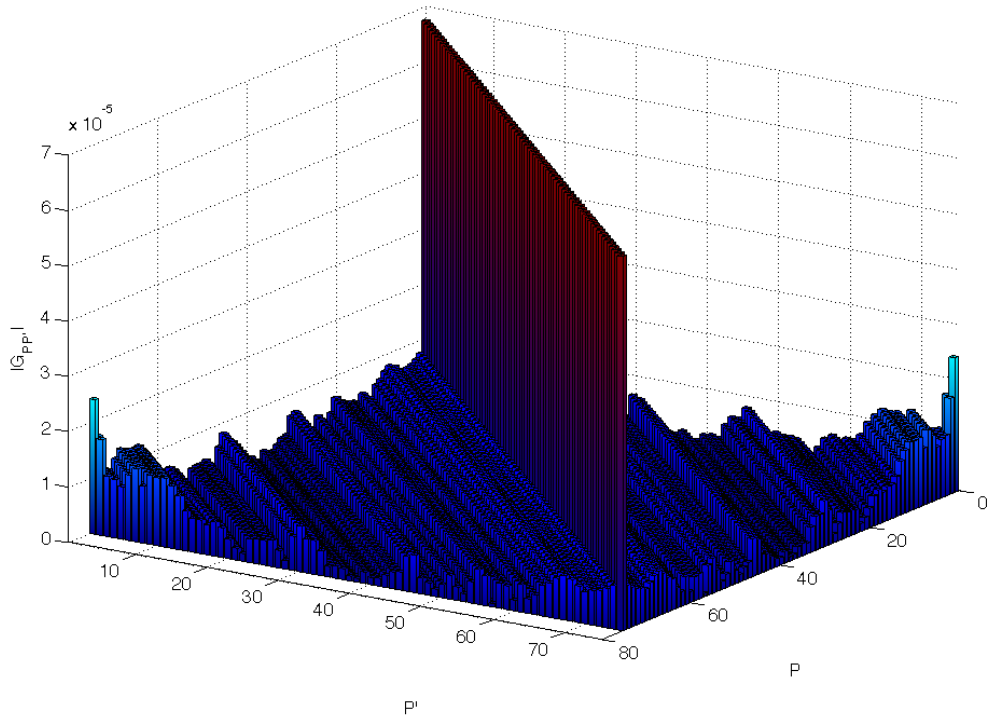


Figure 4.5: The matrix \mathbf{G} element magnitudes corresponding to the imaging experiment with proposed Maxwell fish-eye lens background (condition number 8.01).

4.6 Focal width

From [6], we know that analytic expression of Maxwell fish-eye lens with continuous variation of permittivity is as follows:

$$G(\mathbf{r}, \mathbf{r}') = \frac{1}{4 \sin(\pi\nu)} P_\nu \left(-1 + \frac{2a^2(\mathbf{r}-\mathbf{r}')^2}{(r^2+a^2)(r'^2+a^2)} \right) \quad (4.6.1)$$

where, \mathbf{r} is observation location, \mathbf{r}' is source location, P_ν is Legendre polynomial, and ν is given by following expression [6]:

$$\nu = \frac{-1 + \sqrt{1 + 4k_b^2 a^2}}{2} \quad (4.6.2)$$

k_b is wave number in homogeneous part of background and is given by:

$$k_b = k_0 \sqrt{\varepsilon_b}$$

where, k_0 is free space wave number. Let us consider an inverse scattering problem with a very thin slab of length $2a\phi_0$ placed conformally to the lens; where a is lens radius.

Classical Lipman-Schwinger integral equation can be written as:

$$\int_{\frac{\pi}{2}-\phi_0}^{\frac{\pi}{2}+\phi_0} G(\phi - \phi') W(\phi') d\phi' = E_s(\phi) \quad (4.6.3)$$

where, contrast source is given by following expression:

$$W(\phi') = E(\phi') [\varepsilon(\phi') - \varepsilon_b]$$

In our proposed method, the object of interest is very thin and located conformal to the Maxwell fish-eye lens and the observation locations are located at the same radial distance diametrically opposite to the lens. In such a case, $(\mathbf{r} - \mathbf{r}')^2$ can be written as given below:

$$(\mathbf{r} - \mathbf{r}')^2 = (a \cos \phi \mathbf{u}_x + a \sin \phi \mathbf{u}_y - a \cos \phi' \mathbf{u}_x - a \sin \phi' \mathbf{u}_y)^2$$

where, \mathbf{u}_x is unit vector in x direction, and \mathbf{u}_y is unit vector in y direction. It can be simplified to following expression:

$$(\mathbf{r} - \mathbf{r}')^2 = a^2 (\cos \phi - \cos \phi')^2 + a^2 (\sin \phi - \sin \phi')^2$$

Few algebraic manipulations reduce this expression down to the equation given below:

$$(\mathbf{r} - \mathbf{r}')^2 = 2a^2 [1 - \cos(\phi - \phi')] \quad (4.6.3a)$$

Using this expression, argument of Legendre polynomial, P_ν , can be simplified further.

Argument of Legendre polynomial is shown below:

$$-1 + \frac{2a^2(\mathbf{r} - \mathbf{r}')^2}{(r^2 + a^2)(r'^2 + a^2)}$$

Location of object of interest and observation locations allows us to have approximations: $|\mathbf{r}| \cong a$, and $|\mathbf{r}'| \cong a$. The approximations results in simplification of the argument of Legendre polynomial as follows:

$$-1 + \frac{(\mathbf{r} - \mathbf{r}')^2}{2a^2}$$

Using value of $(\mathbf{r} - \mathbf{r}')^2$ from equation (4.6.3a), this expression further reduces to:

$$-\cos(\phi - \phi') = \cos(\theta - \pi)$$

where, θ is the angle between contrast source location and observation location and is given by:

$$\theta = \phi - \phi'$$

Hence, the Green's function reduces down to following expression:

$$G(\theta) = \frac{P_\nu(\cos(\theta - \pi))}{4 \sin(\pi\nu)} \quad (4.6.4)$$

Legendre polynomial can be expressed by the expression [15] given below:

$$P_\nu(x) = {}_2F_1[-\nu, \nu + 1; 1; \frac{1}{2}(1 - x)] \quad (4.6.4a)$$

where, ${}_2F_1$ is hypergeometric function. It can be expressed [15] by the following expression:

$${}_2F_1(a, b; c; z) = \sum_{n=0}^{\infty} \frac{(a)_n (b)_n z^n}{(c)_n n!} \quad (4.6.4b)$$

$(x)_n$ is the pochhammer symbol. It is given by [15] the equation given below:

$$(x)_n \equiv \frac{\Gamma(x+n)}{\Gamma(x)} \quad (4.6.4c)$$

Using definitions in equation (4.6.4a), we write Legendre polynomial in terms of hypergeometric function. Subsequently, we express the Legendre polynomial as a summation over the terms in equation (4.6.4b). Since near the focal region, $(1 - \cos(\theta - \pi))^n$ is very small for $n = 2, 3, \dots, \infty$. We can approximate the summation series using summation for values $n = 0$ and $n = 1$. Hence, using equation (4.6.4c), Legendre polynomial can be simplified to the following expression around the focal region:

$$P_\nu(\theta) = \left[1 - \nu(\nu + 1) \sin^2 \left(\frac{\theta - \pi}{2} \right) \right] \quad (4.6.4d)$$

In equation (4.6.3), $E_s(\phi)$ is scattered field collected at observation location. When observation location is restricted in interval $[\frac{3\pi}{2} - \phi_0, \frac{3\pi}{2} + \phi_0]$, inverse source problem becomes well posed. The observation location $\phi \in [\frac{3\pi}{2} - \phi_0, \frac{3\pi}{2} + \phi_0]$ corresponds to source location $\phi' \in [\frac{\pi}{2} - \phi_0, \frac{\pi}{2} + \phi_0]$. Using equation (4.6.4d), Green's function (4.6.1) can be written as:

$$G(\theta) = \frac{1}{4\sin(\pi\nu)} \left[1 - \nu(\nu + 1) \sin^2 \left(\frac{\theta - \pi}{2} \right) \right] \quad (4.6.5)$$

We approximate $\nu(\nu + 1) \cong \nu^2$. By equating $G(\pi - \Delta\theta)$ to zero, we get following expression:

$$\sin^2 \left(\frac{\theta - \pi}{2} \right) = \frac{1}{\nu(\nu + 1)} \cong \frac{1}{\nu^2} \quad (4.6.5a)$$

Since near the focal point θ tends to π , this expression further reduces to equation given below:

$$\frac{\theta - \pi}{2} = \frac{1}{\nu} \quad (4.6.5b)$$

Since ν is directly proportional to k_b and a , we find focusing width $\Delta\theta$ as follows:

$$\theta - \pi = \Delta\theta = \frac{2}{k_b a} \quad (4.6.6)$$

Note, that $\Delta\theta$ tends to 0 (infinitely strong focusing) when background medium becomes infinitely dense ($k_b a \rightarrow \infty$).

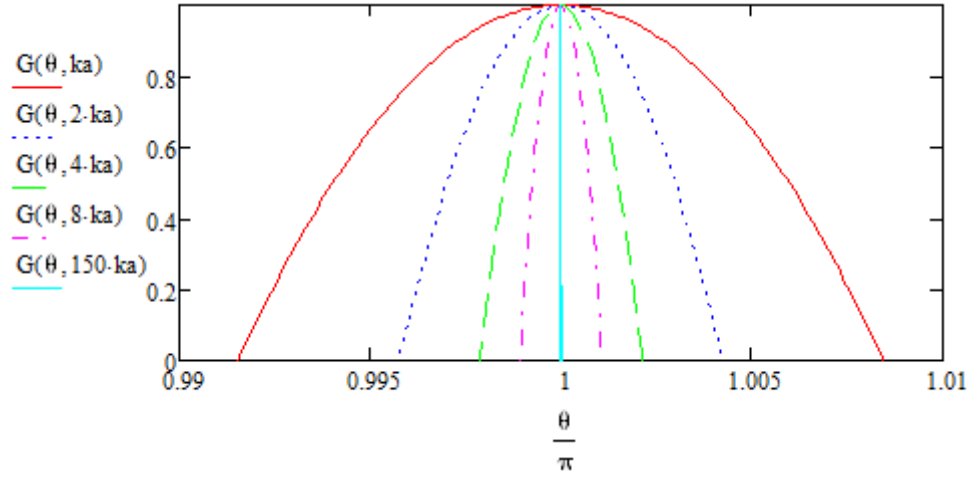


Figure 4.6: Focusing width gets narrower with higher $k_b a$.

Figure 4.6 illustrates narrowing down of focal width as value of $k_b a$ increases. The widest focal width is shown for $k_b a$. The narrower focal width is exhibited by $2k_b a$. As we transitioned to $4k_b a$ and $8k_b a$ values, focal width becomes narrower. We approach infinitely strong focusing as illustrated in Figure 4.6 by the narrowest focus width at $\theta = \pi$ when the background and the radius is set to $150k_b a$.

In the limit of an infinitely strong focusing, Green's function can be written as follows:

$$G(\theta) = \delta(\theta - \pi) + \gamma(\theta) \quad (4.6.7)$$

where, $\gamma(\theta)$ is a smooth function. Substituting equation (4.6.7) in equation (4.6.3), we cast the classical integral equation of the inverse source problem into a well-posed form of the following second-kind integral equation as shown below:

$$W(\phi - \pi) + \int_{\frac{\pi}{2} - \phi_0}^{\frac{\pi}{2} + \phi_0} \gamma(\phi - \phi') W(\phi') d\phi' = E_s(\phi); \phi \in [\frac{3\pi}{2} - \phi_0, \frac{3\pi}{2} + \phi_0] \quad (4.6.8)$$

Note that attaining infinite focusing properties of the medium is not necessary for obtaining well-posedness of the inverse problem formulation. For well-posedness, it is sufficient to make the focusing background dense enough that matrix \mathbf{G} in its discretized form (4.2.3) attains the full rank.

Chapter 5

Numerical Results for the Inverse Problem

This chapter summarizes numerical results obtained from direct inverse problem solution described in Chapter 4. We conduct imaging experiments according to setup shown in Figure 5.1. The imaging domain, S , is the domain of the region fairly thin and conformal to the lens. In the figure, source points are marked I_1 to I_{21} . The figure shows 21 source positions for presentation clarity. In the illustrated results, we use 400 point sources of interrogating field unless otherwise mentioned. In all cases, sources are located at $\rho_s = 2.5$ meters away from lens center evenly spaced on an arc ranging from 0 to π . Each of the filament sources' current is set to 1 Ampere. Also, the figure illustrates observation locations r_1 to r_{10} . Number of observation locations depends on the number of pixels reconstructed. When air is the homogeneous part of background, 25 pixels are reconstructed. When homogeneous part of background's relative permittivity is selected to be 2, 4, 9 and 16, the number of reconstructed pixels is selected to be 35, 49, 75, and 99 respectively. The figure shows 10 of them for presentation clarity. Lens used for image

reconstruction has 2 meters radius. Frequency of excitation is 600 MHz unless otherwise mentioned. Also, we use 5 millimeters thick slab unless otherwise mentioned.

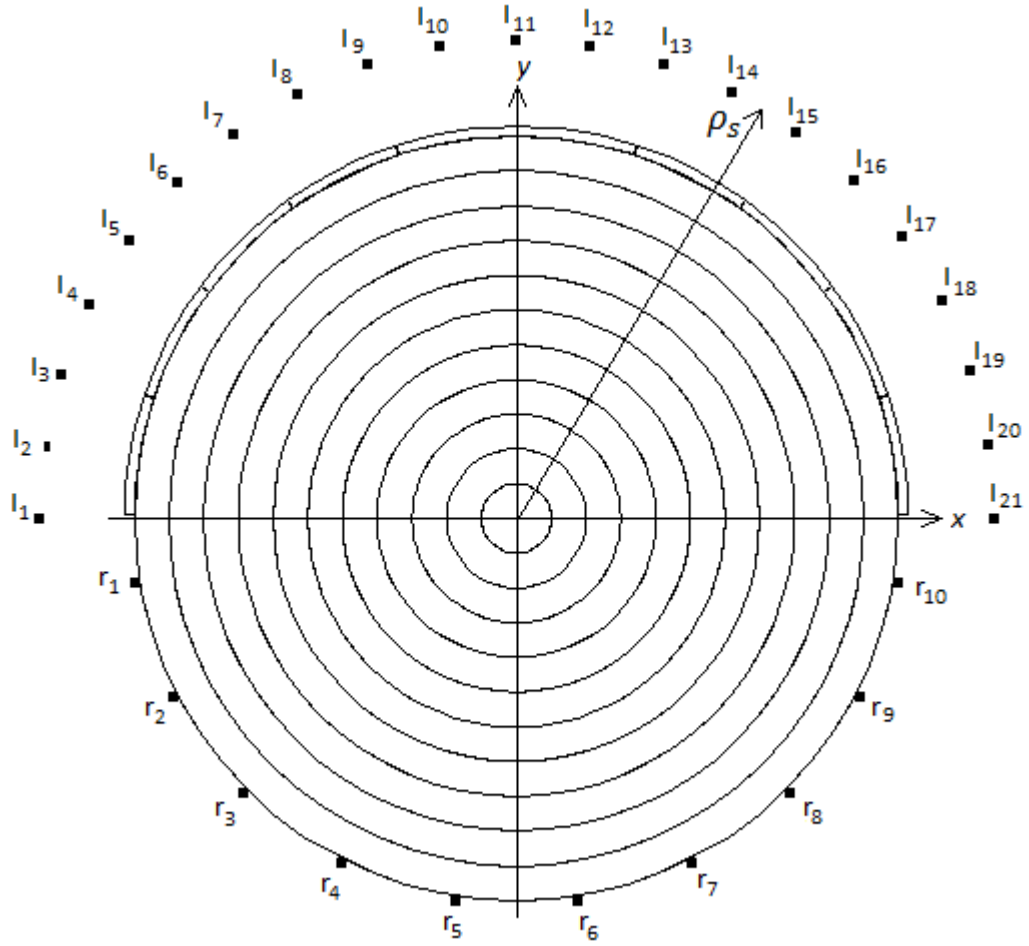


Figure 5.1: Thin slab conforming to Maxwell fish-eye lens is excited with incident wave in imaging domain S .

In particular, we are conducting the studies by varying the background of the lens, frequency of interrogating time-harmonic field, and number of interrogating sources. We also study possibilities for increasing the resolution. Results are obtained in custom writ-

ten method of moments code utilizing Mie series representation of the lens' Green's function [3]. We verify our numerical results by solving the forward problems in COMSOL [12].

5.1 Background variation

As seen from equation (4.6.6), increasing the background permittivity makes the focal width narrower. This allows for reconstruction of object permittivity with higher pixels in its discretization, provided other parameters of imaging experiment remain the same. We have varied the homogeneous part of the background's relative permittivity through values 1, 2, 4, 9, and 16. So, we have also varied dielectric values of each layer of the Maxwell fish-eye lens according to equation (3.3.1). The relative dielectric permittivity at the center of the lens goes over values 4, 8, 16, 36, and 64 in each of those cases respectively. Varying background, we observe that the smallest error of contrast source reconstruction occurs when the contrast, $(\varepsilon(\mathbf{r}) - \varepsilon_b)$, is the lowest. This is illustrated in Figures 5.2, 5.4, 5.6, 5.8, and 5.10. Imaginary part of reconstructed permittivity exhibiting same characteristic is shown in Figures 5.12, 5.14, 5.16, 5.18, and 5.20. It is also shown that when the experiment is conducted in absence of the lens, the image of the object of interest is improperly reconstructed. Real part of reconstructed permittivity is shown in Figures 5.3, 5.5, 5.7, 5.9, and 5.11; and the imaginary reconstructed permittivity are illustrated in Figures 5.13, 5.15, 5.17, 5.19, and 5.21. Reconstructed values have a resolution of $\frac{\lambda_b}{2}$; where, λ_b is the wavelength in the homogeneous part of background.

Figure 5.2 and Figure 5.3 compares image reconstruction when lens is present and when lens is absent, respectively. It is visually evident that lens presence provides better image reconstruction. Numerical results show erroneous reconstruction when lens is absent. This is due to high condition number of the \mathbf{G} matrix. High condition number produces an erroneous solution as shown in Figure 5.3. The background has a relative permittivity 1.

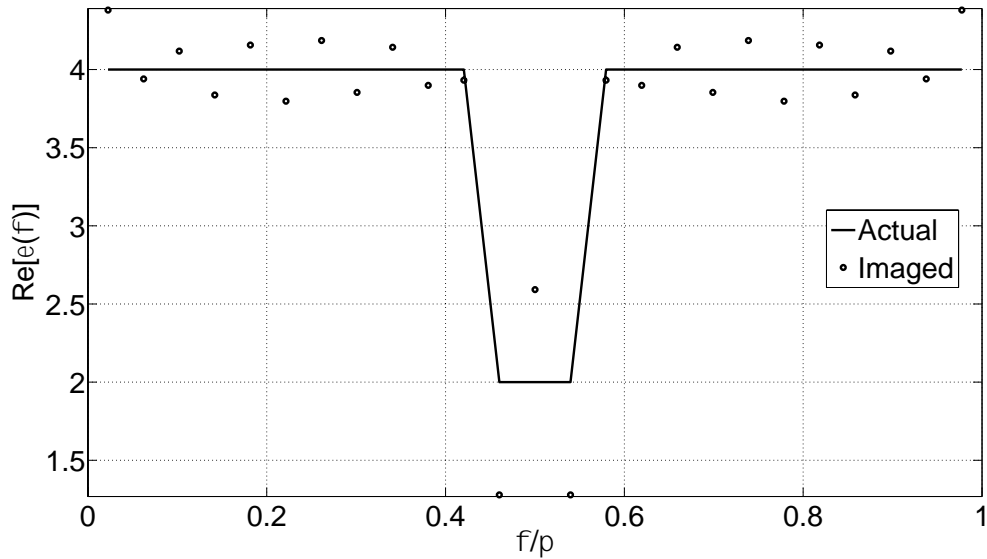


Figure 5.2: Real part of object's relative permittivity and its reconstructed values are illustrated with air in homogeneous part of background. Values shown are reconstructed in presence of lens.

Figure 5.2 shows image reconstruction results in presence of Maxwell fish-eye lens. On the other hand, Figure 5.3 shows reconstructed image when imaging experiment is conducted in absence of lens. It is visually evident that lens presence helps more accurate image reconstruction. This is due to well-posed formulation of the inverse problem.

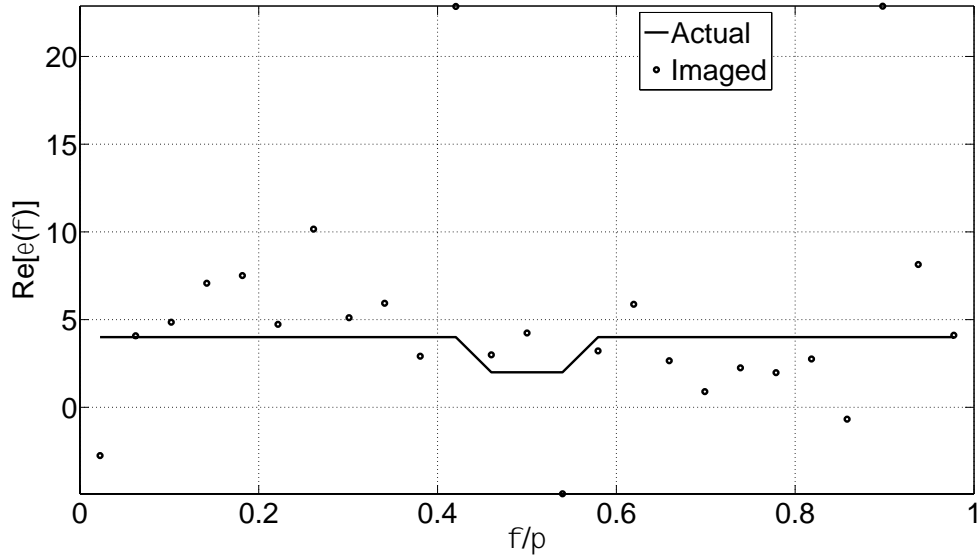


Figure 5.3: In absence of lens, real part of reconstructed relative permittivity is compared to object's relative permittivity when air is the homogeneous background.

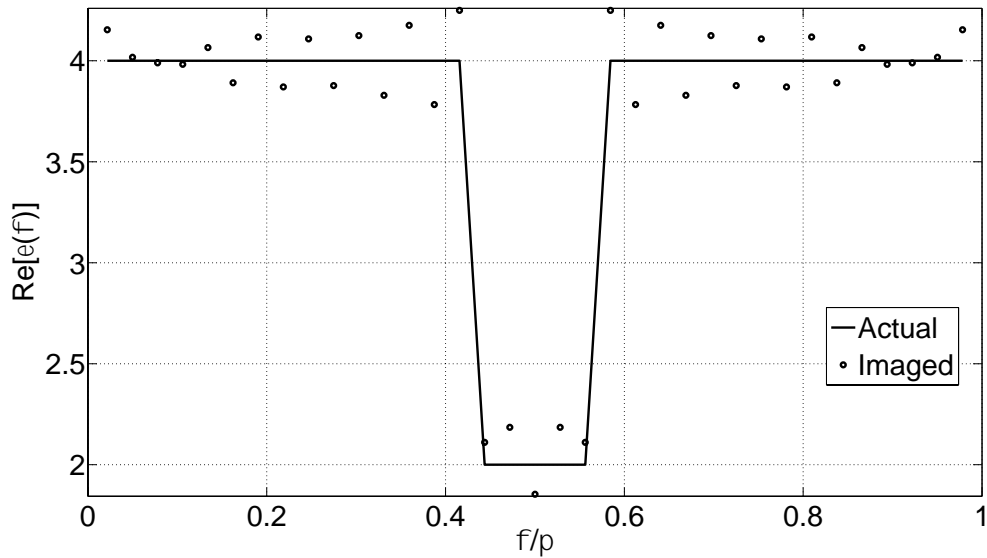


Figure 5.4: Real part of object's relative permittivity and its reconstructed values are illustrated with relative permittivity 2 in homogeneous part of background. Values shown are reconstructed in presence of lens.

When the imaging experiment is conducted with homogeneous part of background permittivity 2, the inverse problem solution in presence and in absence of lens is illustrated in Figure 5.4 and 5.5 respectively. Also in this case, it is visually evident that presence of lens allows for better image reconstruction. Lens presence ensures well-posedness of the inverse problem.

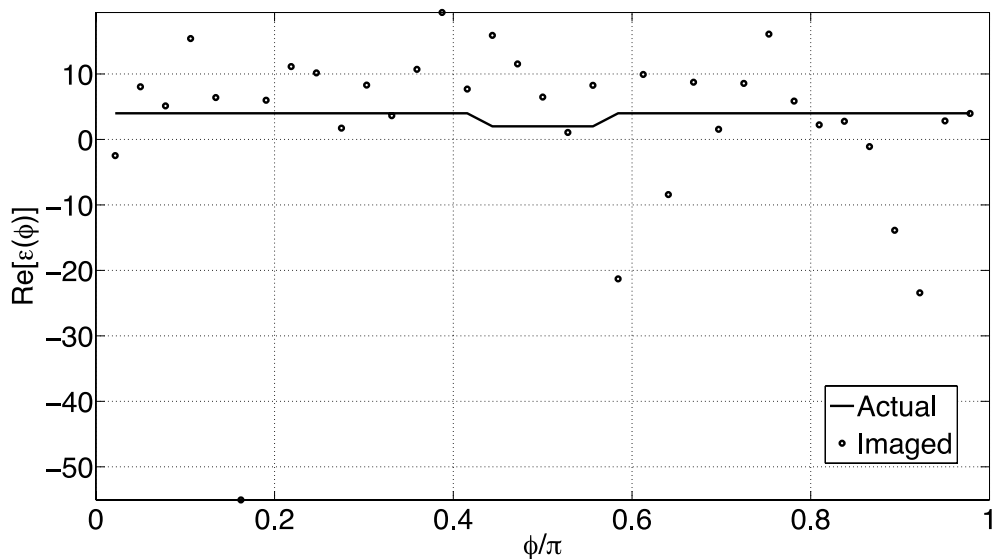


Figure 5.5: When imaging experiment is conducted in absence of lens, real part of object's relative permittivity and its reconstructed values are illustrated, provided relative permittivity of homogeneous background is 2.

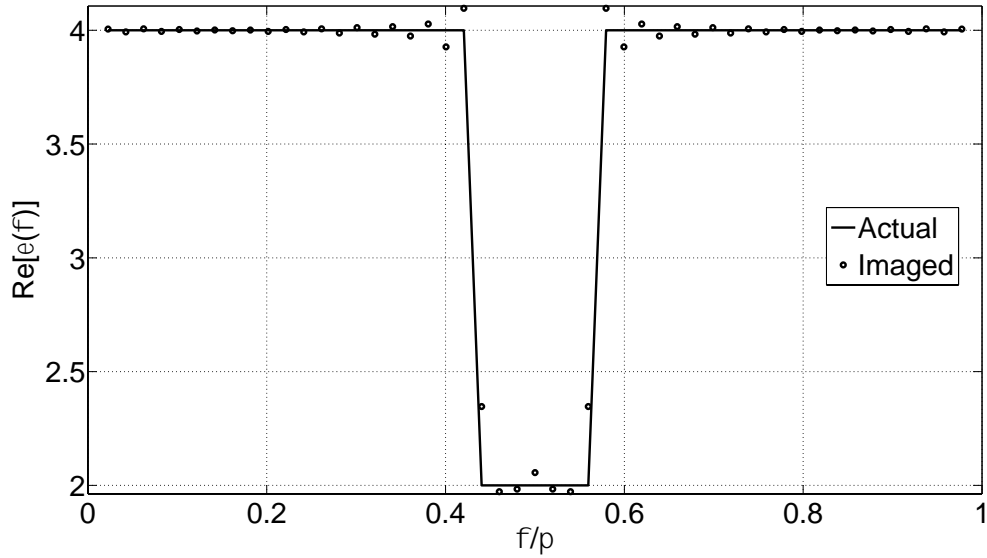


Figure 5.6: Real part of object's relative permittivity and its reconstructed values are illustrated when homogeneous part of background has relative permittivity 4. Values shown are reconstructed in presence of lens.

Figure 5.6 and Figure 5.7 shows image reconstruction with lens present and with lens absent, respectively. Since the contrast of the object with respect to the background is zero, more accurate reconstruction is obtained when lens is present. When lens is absent, we have high inaccuracy in the results as shown in Figure 5.7.

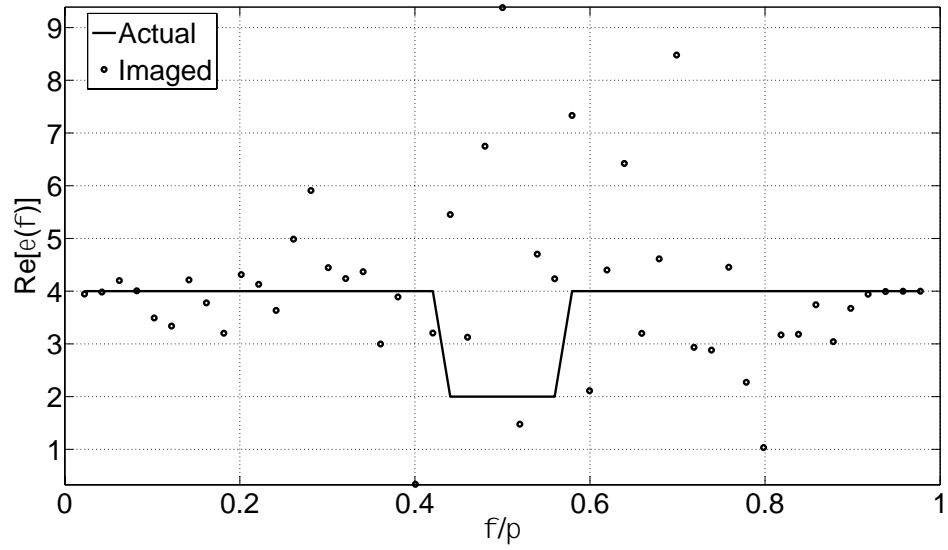


Figure 5.7: When imaging experiment is conducted in absence of lens, real part of object's relative permittivity and its reconstructed values are illustrated, provided relative permittivity of homogeneous background is 4.

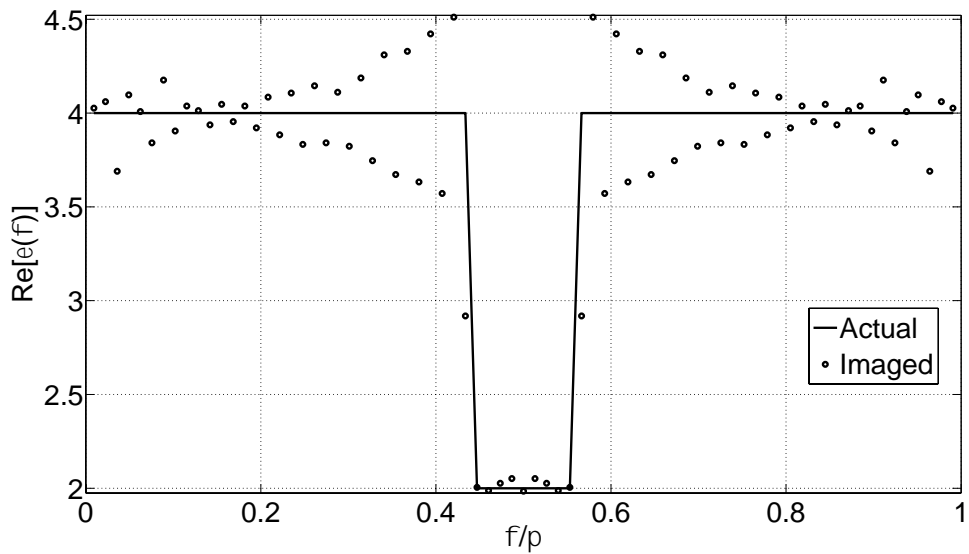


Figure 5.8: Real part of object's relative permittivity and its reconstructed values are illustrated with relative permittivity 9 in homogeneous part of background. Values shown are reconstructed in presence of lens.

Figure 5.8 shows image reconstruction in presence of lens. We can note that higher contrast shows higher Gibbsian oscillations in image reconstruction in presence of lens. Image reconstruction using the same object of interest in absence of lens results in high inaccuracy in reconstructed image as shown in Figure 5.9.

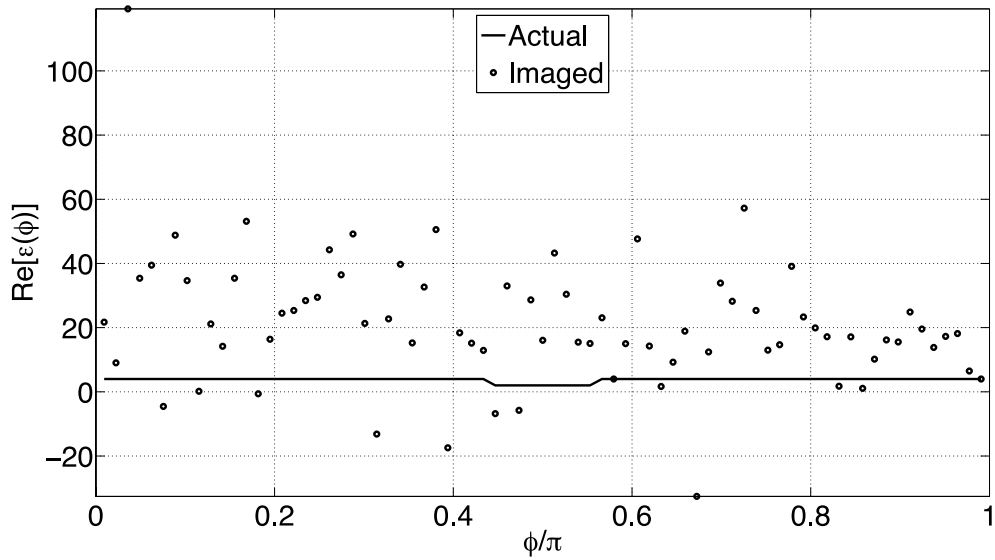


Figure 5.9: When imaging experiment is conducted in absence of lens, real part of object's relative permittivity and its reconstructed values are illustrated, provided relative permittivity of homogeneous background is 9.

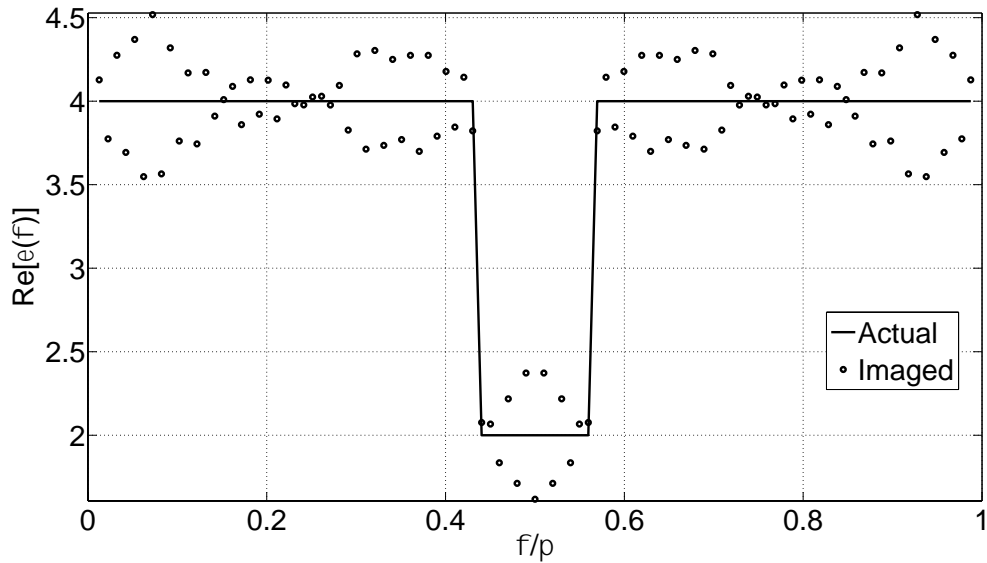


Figure 5.10: Real part of object's relative permittivity and its reconstructed values are illustrated with relative permittivity 16 in homogeneous part of background. Values shown are reconstructed in presence of lens.

Figure 5.10 shows image reconstruction results when numerical experiment is conducted in presence of lens. On the other hand, Figure 5.11 shows reconstructed image when numerical experiment was conducted in absence of the lens. It is visually evident that more accurate image reconstruction is obtained when inverse problem is solved upon scattered field collection through the use of lens.

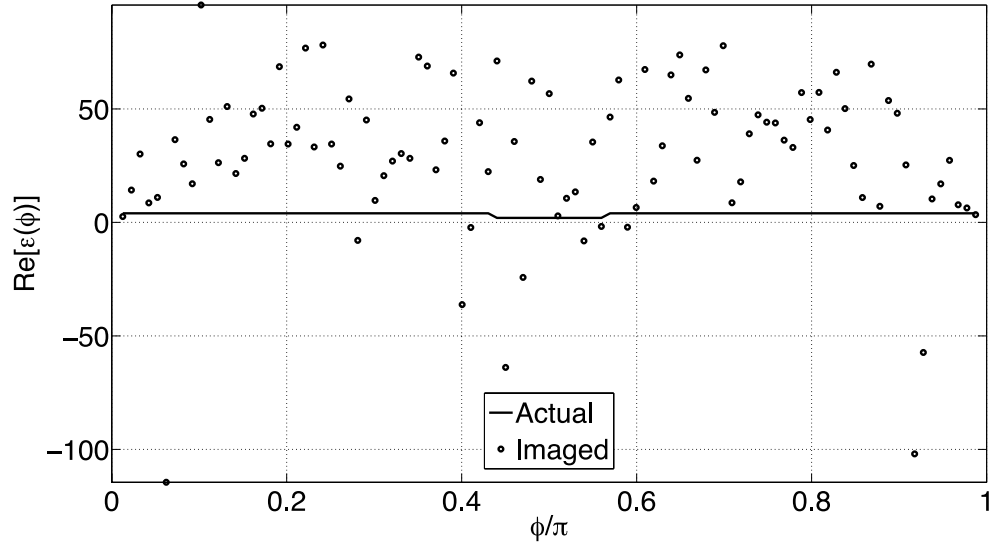


Figure 5.11: When imaging experiment is conducted in absence of lens, real part of object's relative permittivity and its reconstructed values are illustrated, provided relative permittivity of homogeneous background is 16.

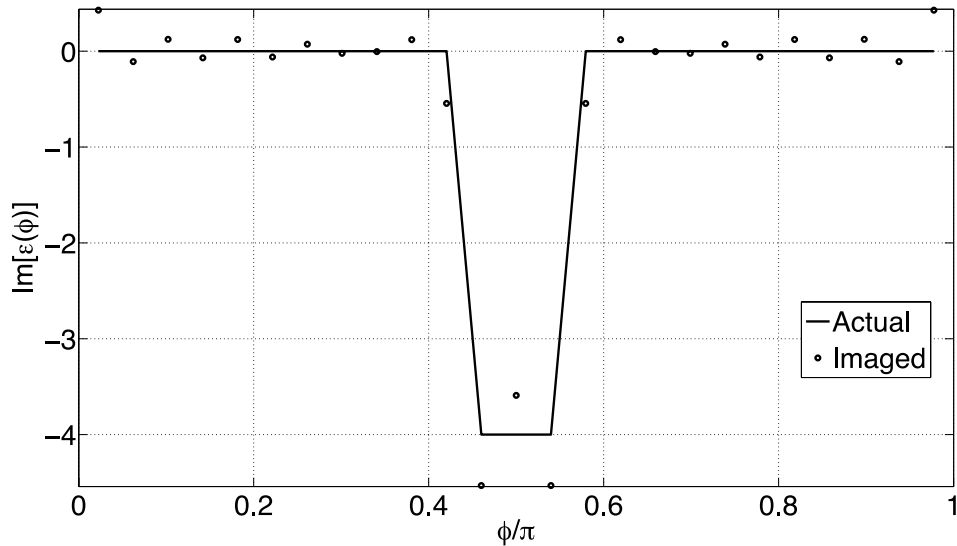


Figure 5.12: Imaginary part of object's relative permittivity and its reconstructed values are illustrated with air in homogeneous part of background. Values shown are reconstructed in presence of lens.

The inverse problem is solved in presence and in absence of the Maxwell fish-eye lens for the same object of interest. Figure 5.12 and Figure 5.13 shows reconstructed image in presence and in absence of lens, respectively. More accuracy in image reconstruction is obtained with lens present in numerical experiment. When lens is absent, reconstructed imaginary part of permittivity shows high inaccuracy in its result as illustrated in Figure 5.13.

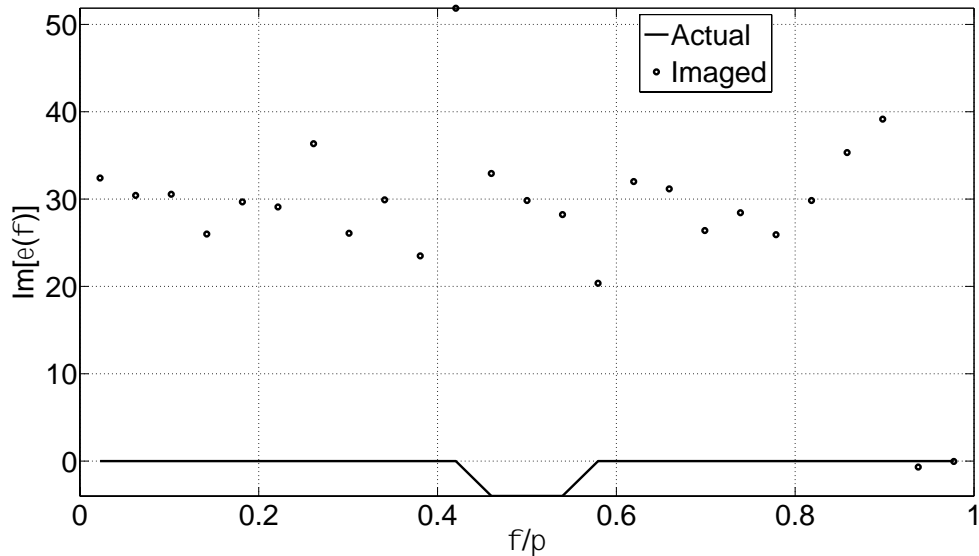


Figure 5.13: When imaging experiment is conducted in absence of lens, imaginary part of object's relative permittivity and its reconstructed values are illustrated, provided air is the homogeneous background.

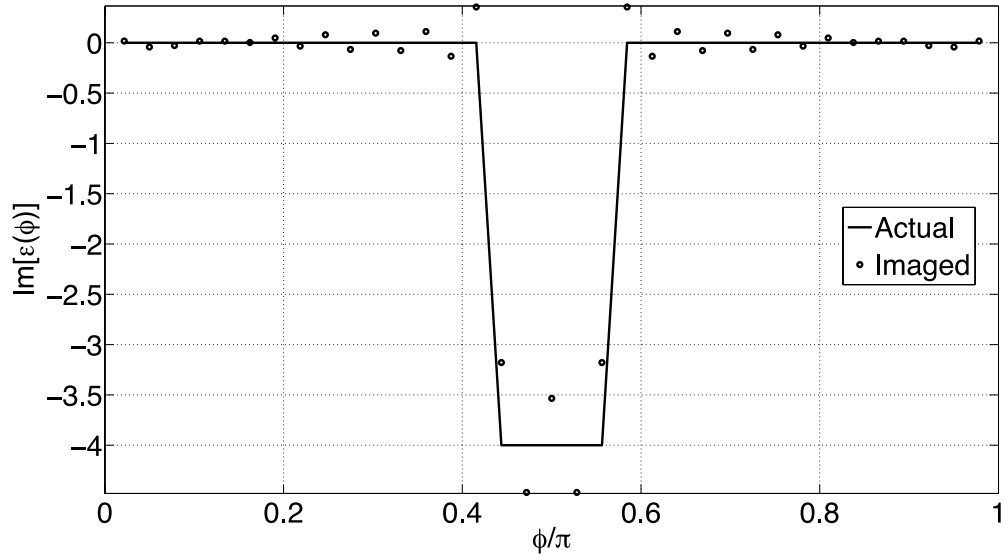


Figure 5.14: Imaginary part of object's relative permittivity and its reconstructed values are illustrated with relative permittivity 2 in homogeneous part of background. Values shown are reconstructed in presence of lens.

Imaginary part of permittivity reconstruction in presence and in absence of lens is illustrated in Figure 5.14 and Figure 5.15 respectively. In the conducted numerical experiments, lens presence shows more accurate image reconstruction. When numerical experiment is conducted in absence of lens, image is reconstructed with high inaccuracy as shown below in Figure 5.15.

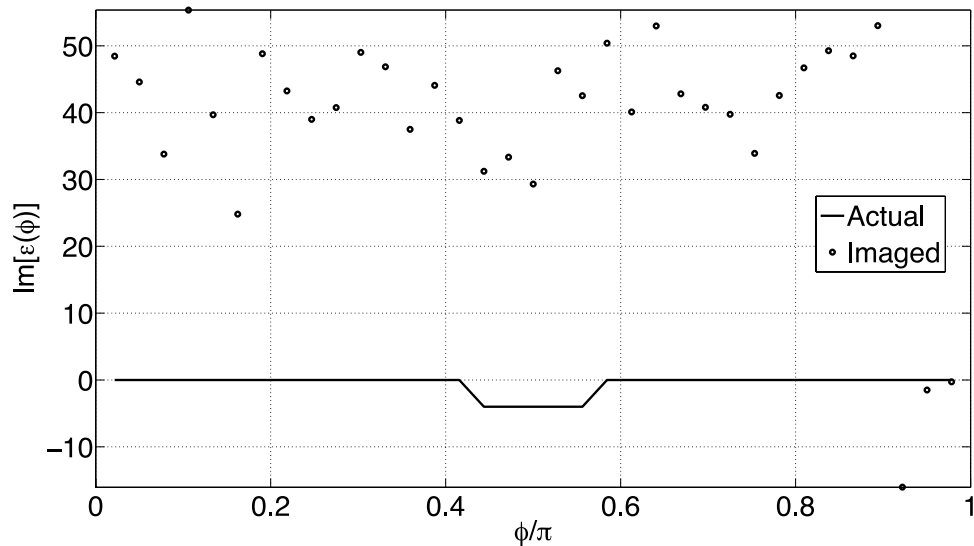


Figure 5.15: When imaging experiment is conducted in absence of lens, real part of object's relative permittivity and its reconstructed values are illustrated, provided relative permittivity of homogeneous background is 2.

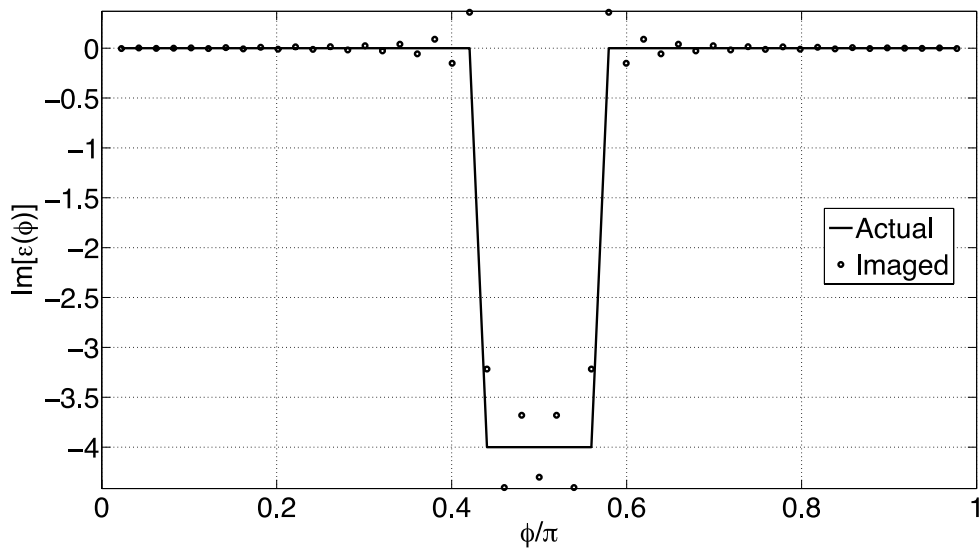


Figure 5.16: Imaginary part of object's relative permittivity and its reconstructed values are illustrated with relative permittivity 4 in homogeneous part of background. Values shown are reconstructed in presence of lens.

When numerical experiment is conducted in presence of lens, we get an accurate reconstruction of permittivity variation within the object of interest. This is illustrated in Figure 5.16. When the same object of interest is reconstructed in absence of the lens, we find high inaccuracy in image reconstruction results. This is illustrated in Figure 5.17. Presence of lens makes invertible matrix well-posed as discussed in Section 4.5 and hence image reconstruction results become more accurate.

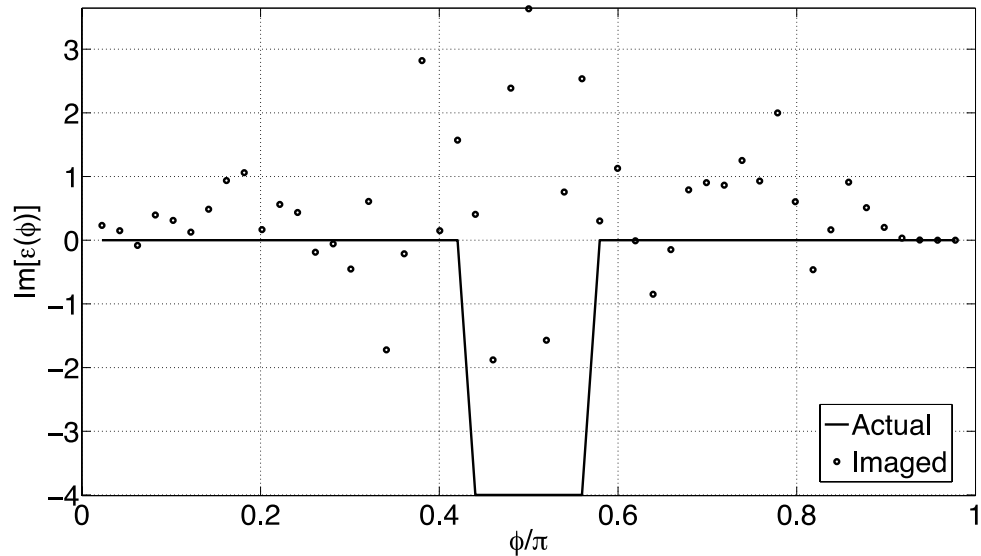


Figure 5.17: When imaging experiment is conducted in absence of lens, real part of object's relative permittivity and its reconstructed values are illustrated, provided relative permittivity of homogeneous background is 4.

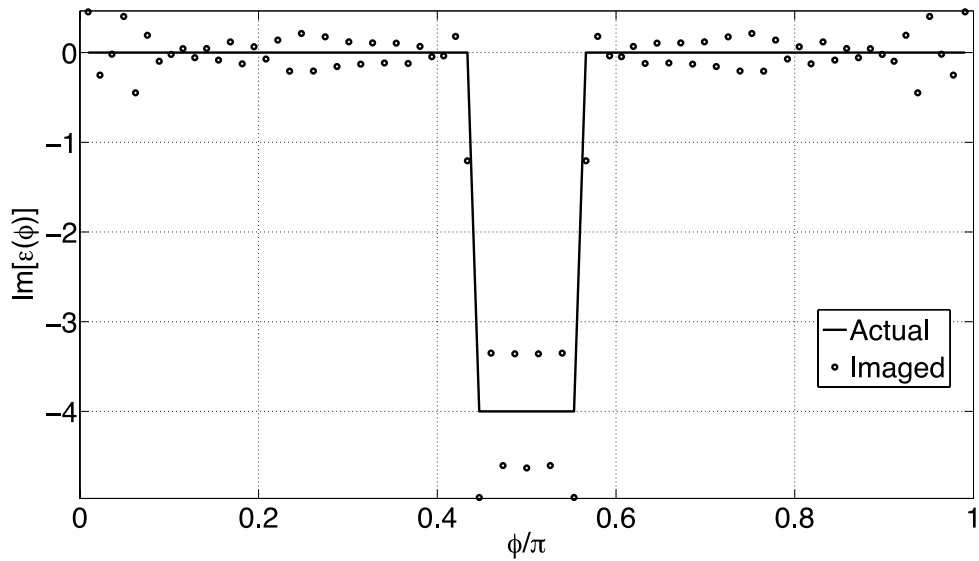


Figure 5.18: Imaginary part of object's relative permittivity and its reconstructed values are illustrated with relative permittivity 9 in homogeneous part of background. Values shown are reconstructed in presence of lens.

Image reconstruction results through inverse problem solution in presence and in absence of Maxwell fish-eye lens is shown in Figure 5.18 and Figure 5.19, respectively. It is visually evident that reconstructed image is found to be more accurate when numerical experiment is conducted in presence of the lens. Lens presence concentrates scattered field from distinct regions of the object of interest to distinct observation locations to cast the inverse problem in well-posed form as discussed in Section 4.4. This results in more accurate results when the numerical experiment is conducted in presence of the lens.

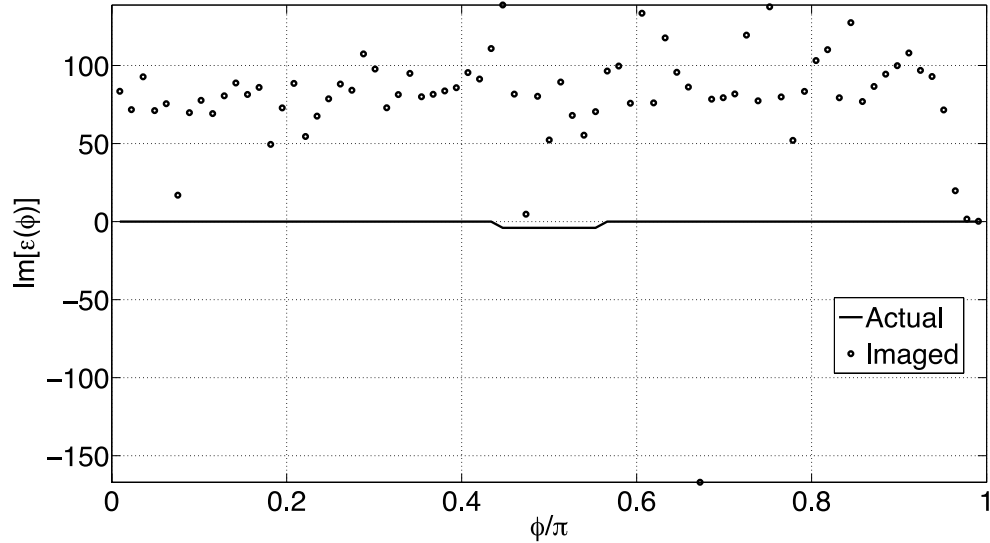


Figure 5.19: When imaging experiment is conducted in absence of lens, real part of object's relative permittivity and its reconstructed values are illustrated, provided relative permittivity of homogeneous background is 9.

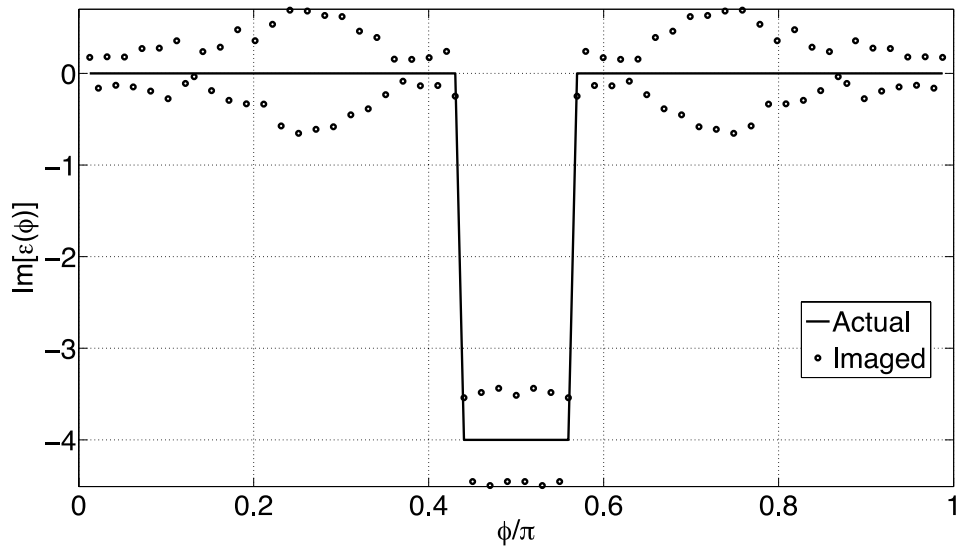


Figure 5.20: Imaginary part of object's relative permittivity and its reconstructed values are illustrated with relative permittivity 16 in homogeneous part of background. Values shown are reconstructed in presence of lens.

Figure 5.20 and Figure 5.21 shows reconstructed image in presence and in absence of lens, respectively. Image reconstruction with lens present shows very high accuracy when compared to image reconstruction in absence of lens. Since presence of lens casts the inverse problem in a well-posed form, more accuracy is obtained.

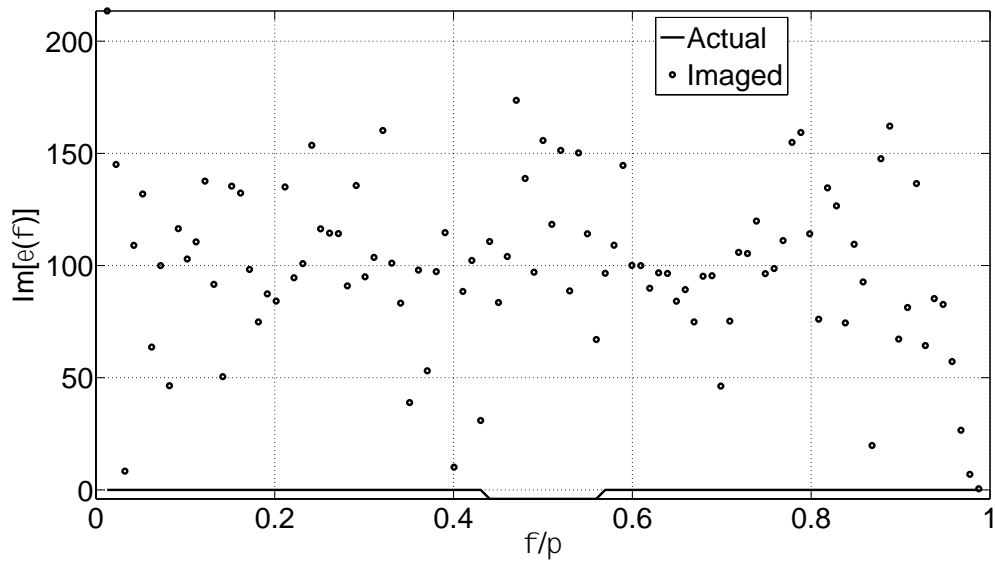


Figure 5.21: When imaging experiment is conducted in absence of lens, real part of object's relative permittivity and its reconstructed values are illustrated, provided relative permittivity of homogeneous background is 16.

We believe surface wave plays an important role in creating higher Gibbsian ringing as the contrast is increased. When the object of interest has less oscillations, we get good accuracy. As the contrast increases, the oscillation within the object of interest also increases. Figures 5.22 to 5.26 shows total electric field variation within object of interest.

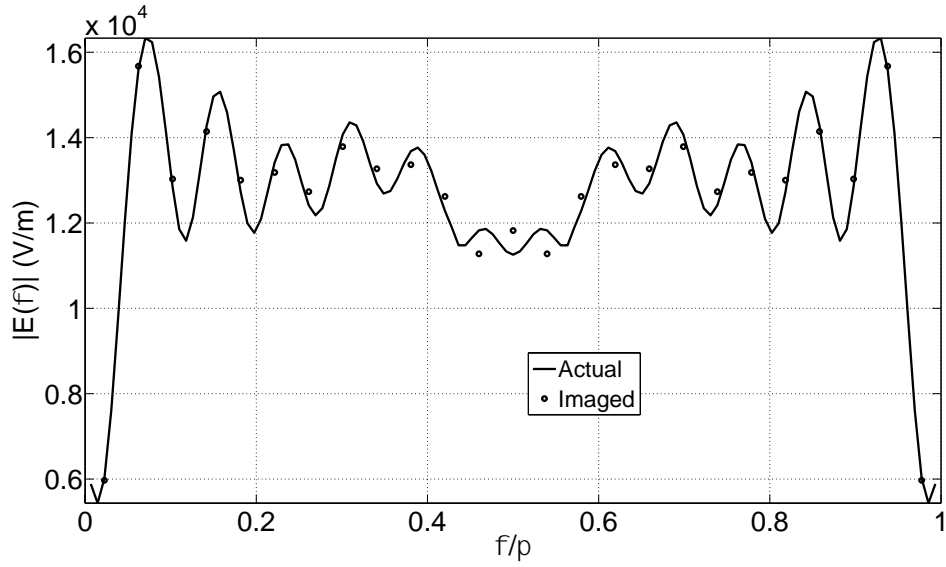


Figure 5.22: Norm of total electric field variation in the object of interest and reconstructed electric field from inverse problem solution in presence of lens when homogeneous part of background permittivity is 1.

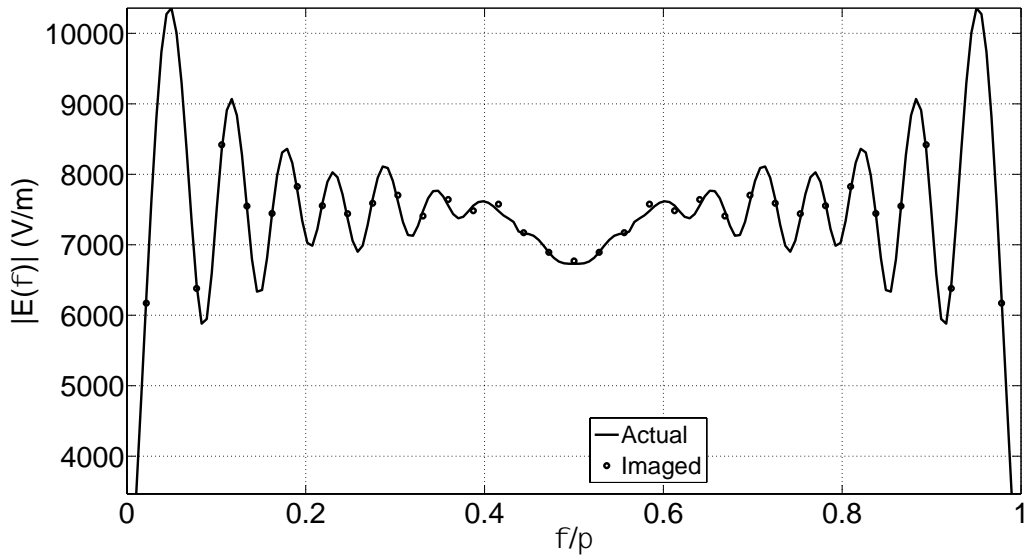


Figure 5.23: Norm of total electric field variation in the object of interest and reconstructed electric field from inverse problem solution when homogeneous part of background permittivity is 2.

Figure 5.22, Figure 5.23 and Figure 5.24 shows total electric field variation within object of interest for homogeneous part of permittivity equal to 1, 2 and 4 respectively. It can be noted that electric field norm oscillations with respect to spatial angle increases with increase in homogeneous part of background permittivity from 1 to 4.

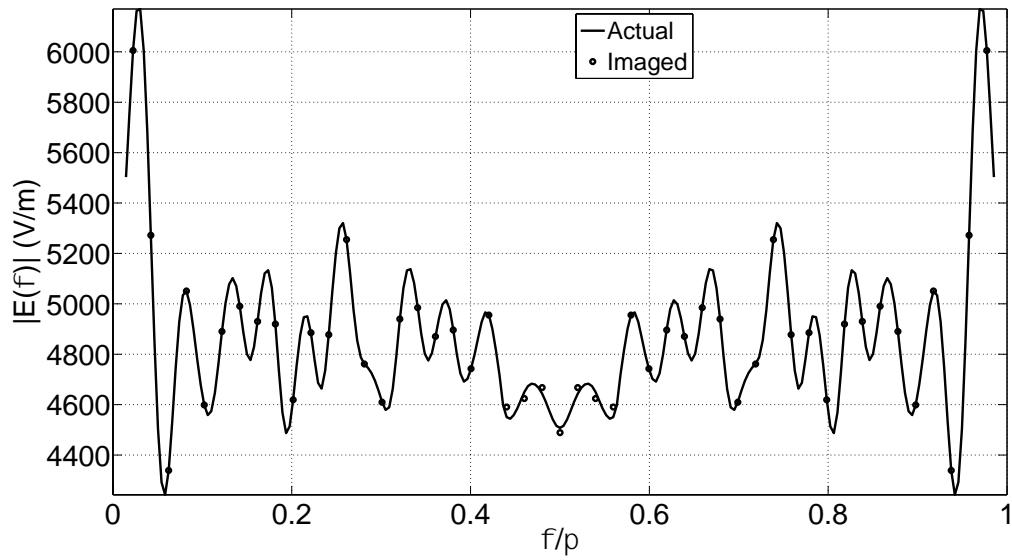


Figure 5.24: Norm of total electric field variation in the object of interest and reconstructed electric field from inverse problem solution when homogeneous part of background permittivity is 4.

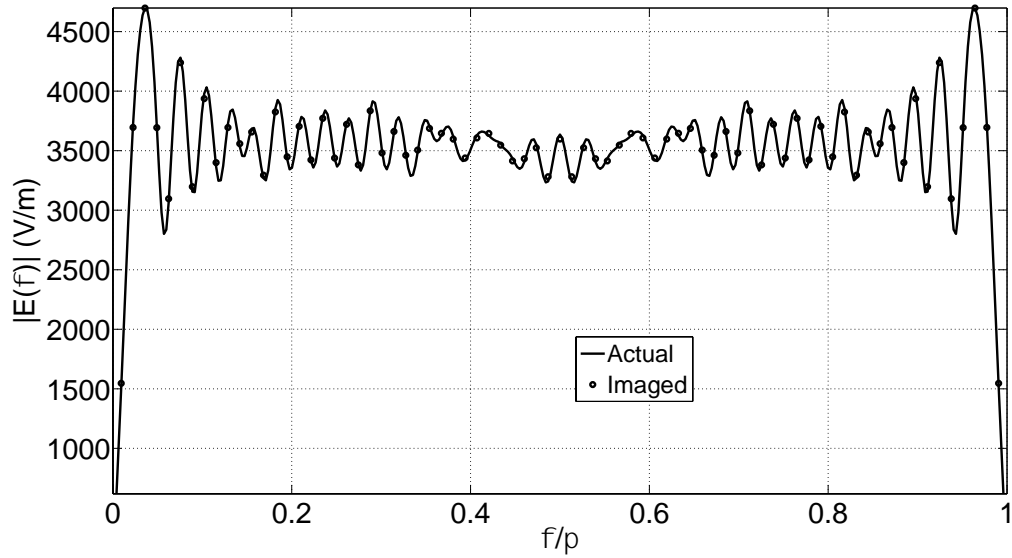


Figure 5.25: Norm of total electric field variation in the object of interest and reconstructed electric field from inverse problem solution when homogeneous part of background permittivity is 9.

Figure 5.25 and Figure 5.26 illustrates total field within object of interest when homogeneous part of background permittivity is 9 and 16, respectively. We can see more electric field norm oscillations with respect to spatial angle increase with increasing background permittivity.

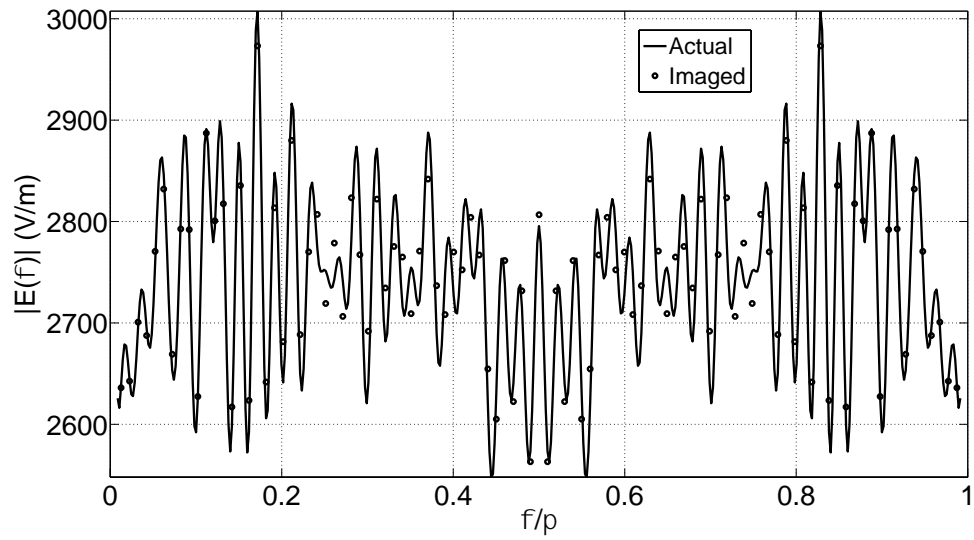


Figure 5.26: Norm of total electric field variation in the object of interest and reconstructed electric field from inverse problem solution when homogeneous part of background permittivity is 16.

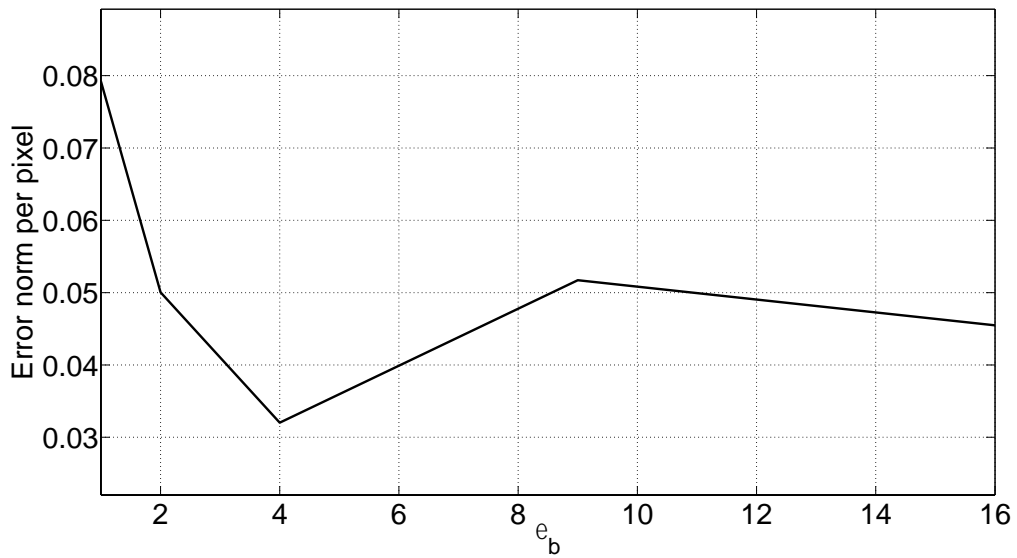


Figure 5.27: Illustration of error norm per pixel variation in presence of lens when background is varied.

Figure 5.27 shows error norm per pixel when object of interest is reconstructed in presence of Maxwell fish-eye lens. Reconstruction in absence of lens yields high inaccuracy as shown in Figure 5.28. The background permittivity is varied to obtain the illustrated behavior.

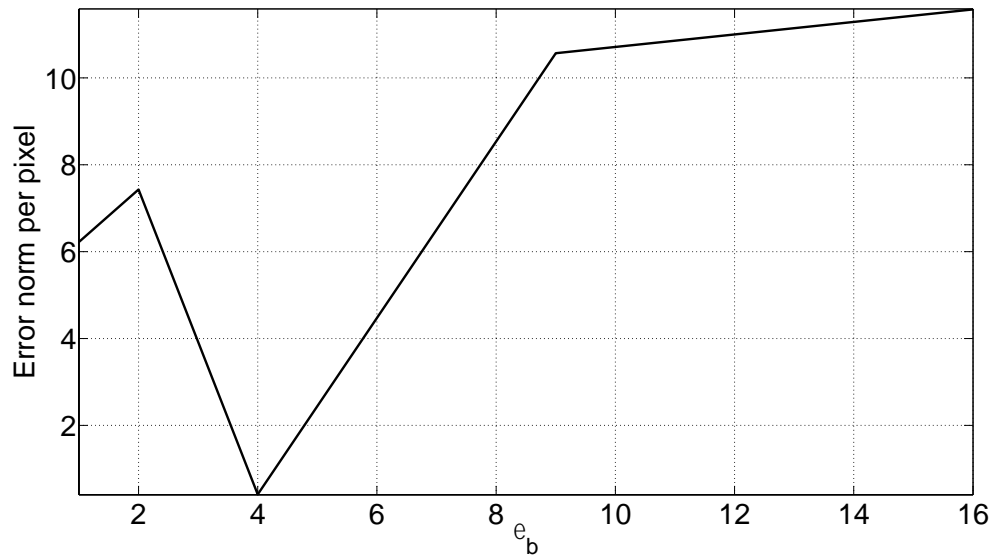


Figure 5.28: Illustration of error norm per pixel variation in absence of lens when background is varied.

In this section, we have observed the following observations:

- Lens presence provides accurate permittivity reconstruction through casting the inverse problem in well-posed form.
- Lower contrast produces lower Gibbsian ringing.
- Higher background contrast produces more oscillations in object of interest.

5.2 Thickness variation

Energy of guided waves is usually confined to a localized region of the waveguide structure and travels in a specific direction. Various types of transmission lines are used to serve this purpose. Dielectric slabs are known to guide waves and hence can serve as transmission lines. Such structures are usually known as dielectric waveguides. Upon electromagnetic wave illumination, surface waves are excited at the discontinuities in the dielectric waveguide.

Upon illumination of an infinitely long slab by a plane wave, no surface wave is produced. The incident plane wave simply refracts at the surface boundaries and passes through the slab material. A surface wave is created within the slab when at least one of the ends of the slab is finite. The surface wave is excited at the finite end and travels along the slab. The magnitude of the surface wave depends on the thickness. Based on conducted experiments, it appears that the thicker is the slab, the higher is the magnitude of the excited surface wave. Figures 5.29 to 5.32 shows the trend with background 9. It should also be noted that the total field obtained from solving the inverse problem gets worse with increase in thickness.

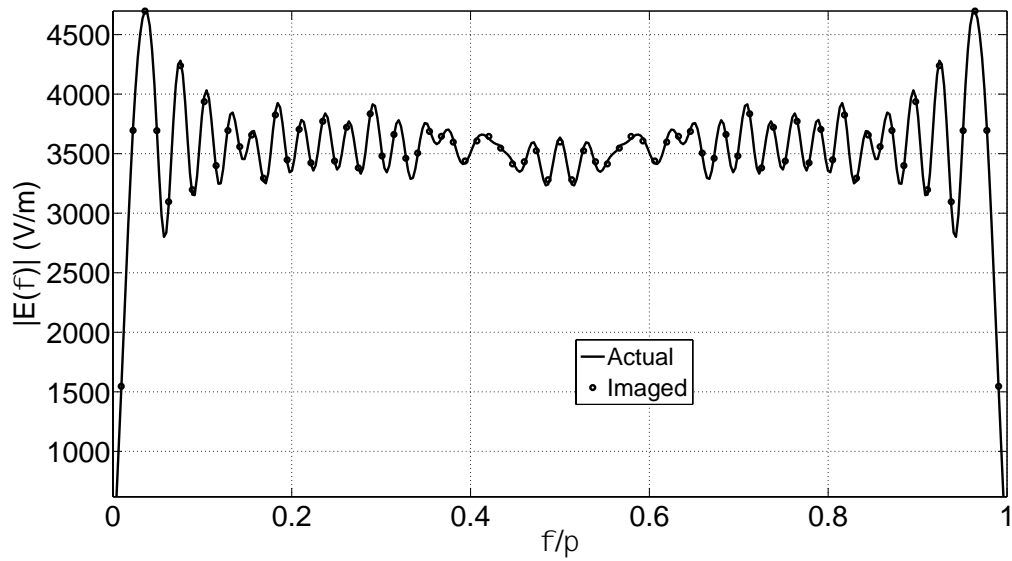


Figure 5.29: Norm of total electric field variation in the slab when thickness is 0.005 meters.

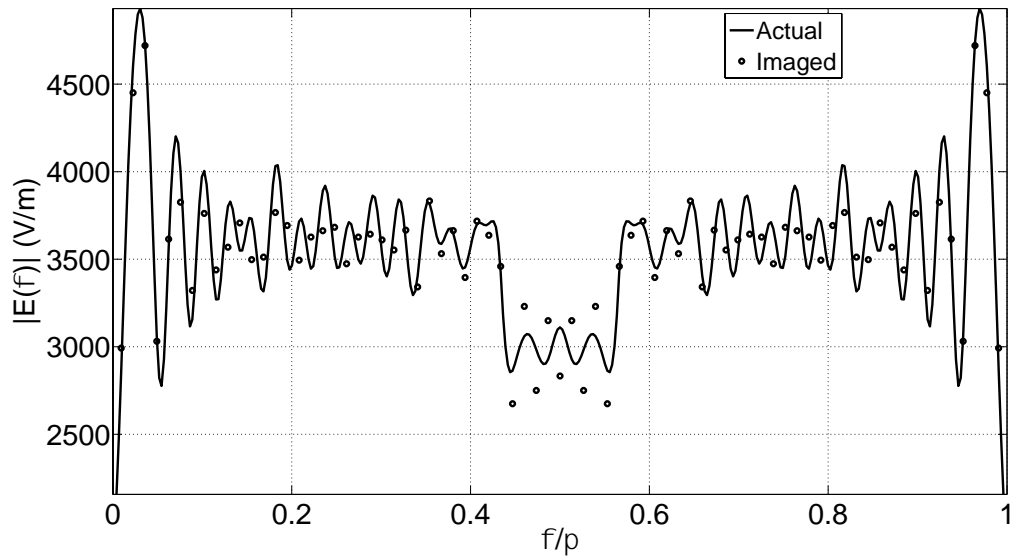


Figure 5.30: Norm of total electric field variation in the slab when thickness is 0.025 meters.

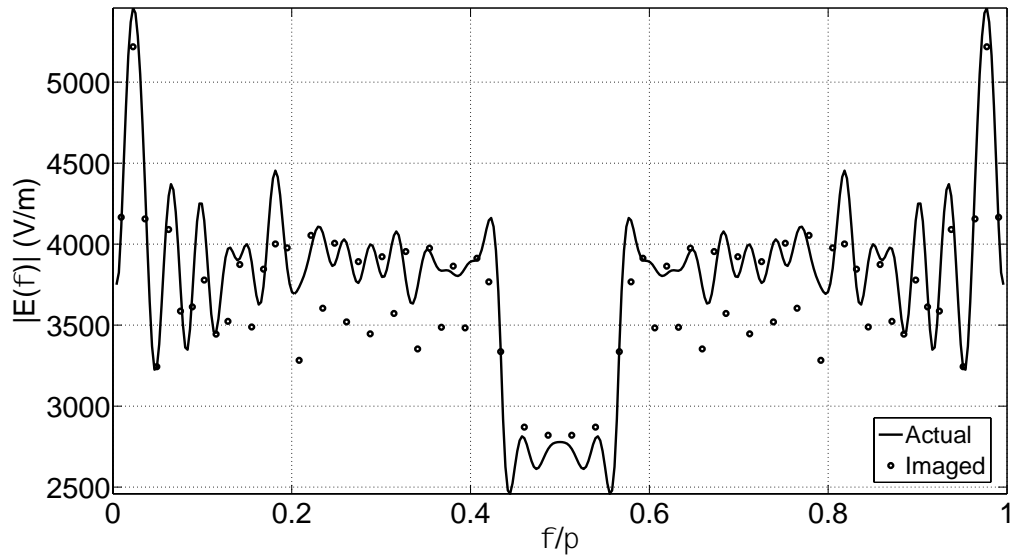


Figure 5.31: Norm of total electric field variation in the slab when thickness is 0.05 meters.

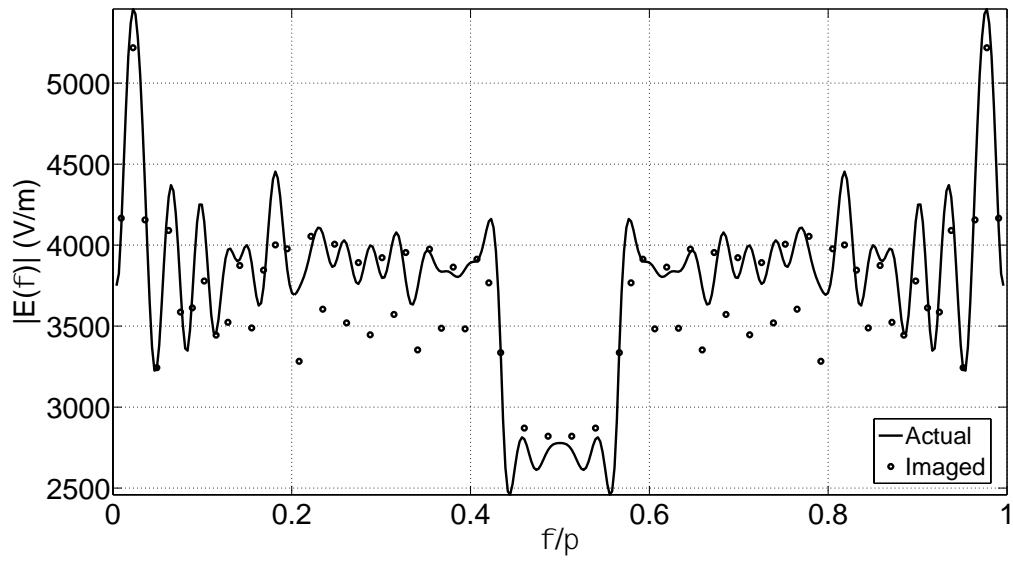


Figure 5.32: Norm of total electric field variation in the slab when thickness is 0.1 meters.

It is also observed that the surface wave excited in the object of interest may have a strong impact on the quality of image reconstruction. The reason is that small magnitude of surface wave produces only insignificant interference with the incident field of the interrogating sources. A surface wave with a large magnitude, on the other hand, will significantly interfere with the incident field. The increased interference between the incident wave and the surface wave excited in the slab results in high variation of field within the slab forming the imaged object. This high variation causes under-sampling of the total field featuring the interference pattern. This leads to increased erroneous Gibbsian oscillations in the reconstructed object profile. A thinner slab produces a better quality of reconstruction due to a weaker presence of the surface waves. This behavior is illustrated in figures 5.33 to 5.40.

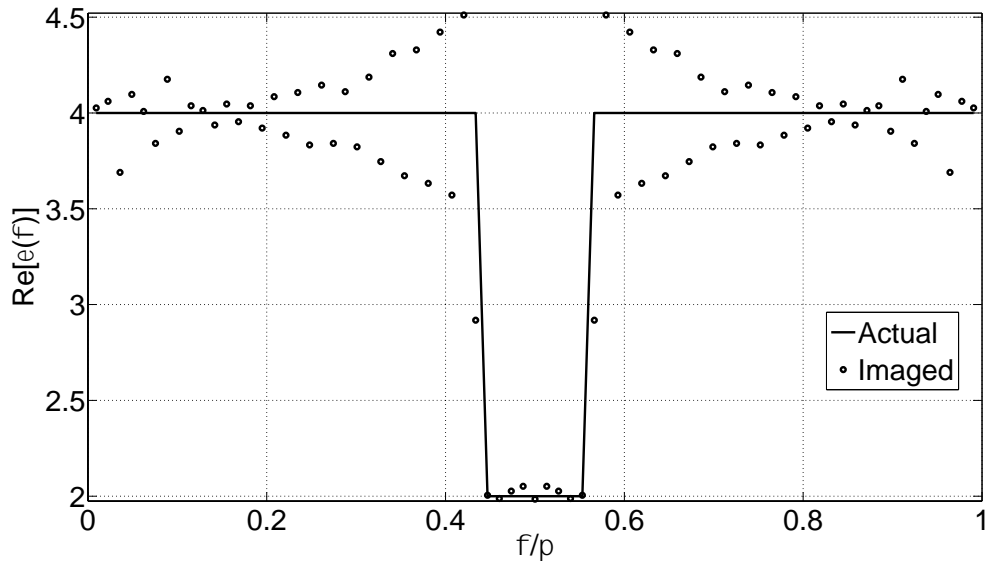


Figure 5.33: When slab thickness is 0.005 meters, real part of reconstructed relative permittivity is compared with the exact relative permittivity in presence of the lens.

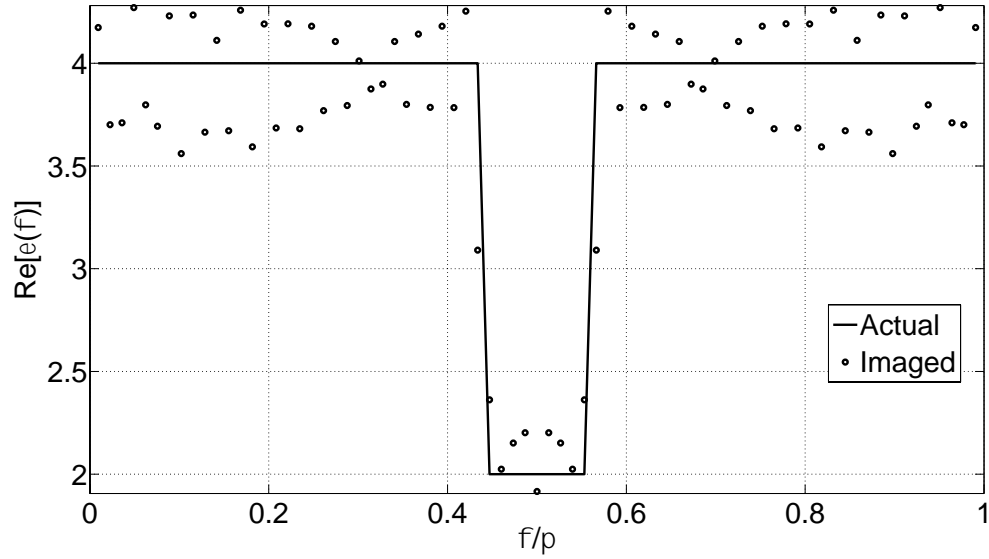


Figure 5.34: When slab thickness is 0.025 meters, real part of reconstructed relative permittivity is compared with the exact relative permittivity in presence of the lens.

Figure 5.33, Figure 5.34 and Figure 5.35 shows real part of reconstructed permittivity for 0.005 meters, 0.025 meters, and 0.05 meters, respectively. We note erroneous Gibbsian oscillations increase with increase in slab thickness. We believe this may be a consequence of surface wave interference with incident field.

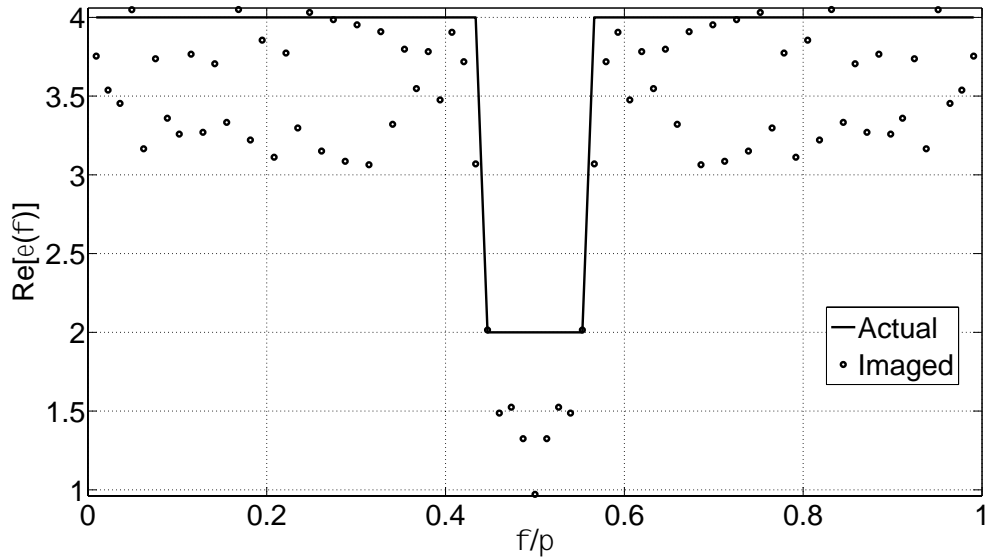


Figure 5.35: When slab thickness is 0.05 meters, real part of reconstructed relative permittivity is compared with the exact relative permittivity in presence of the lens.

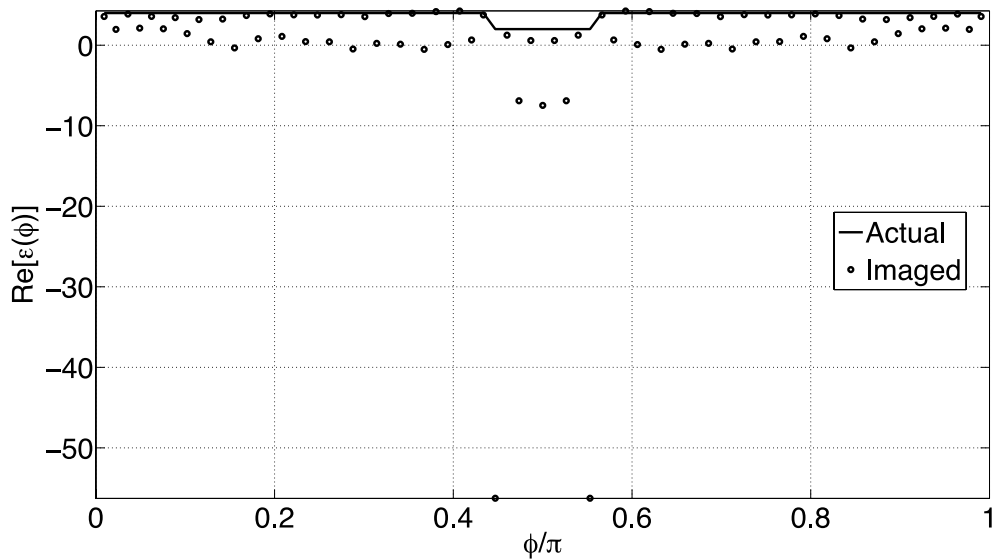


Figure 5.36: When slab thickness is 0.1 meters, real part of reconstructed relative permittivity is compared with the exact relative permittivity in presence of the lens.

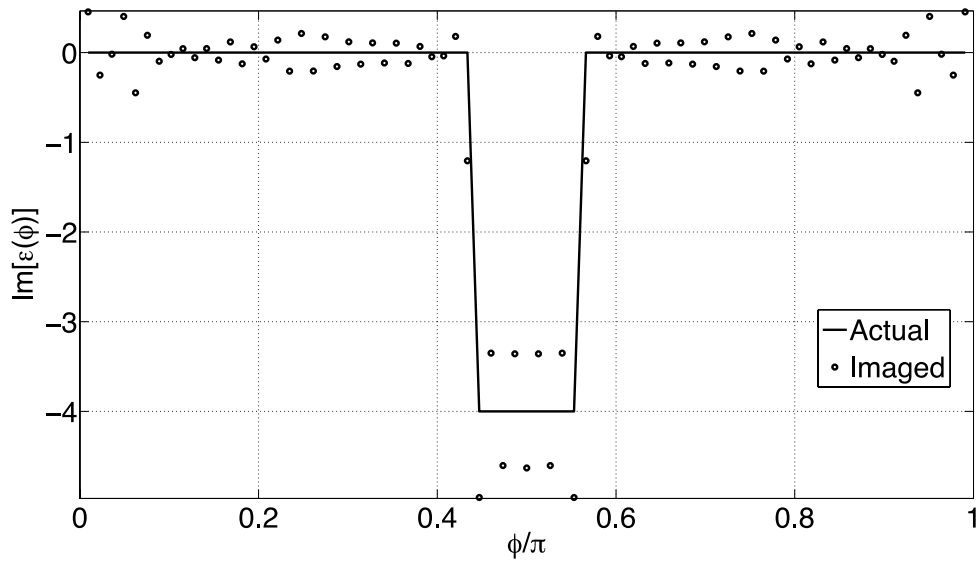


Figure 5.37: When slab thickness is 0.005 meters, imaginary part of reconstructed relative permittivity is compared with the exact relative permittivity in presence of the lens.

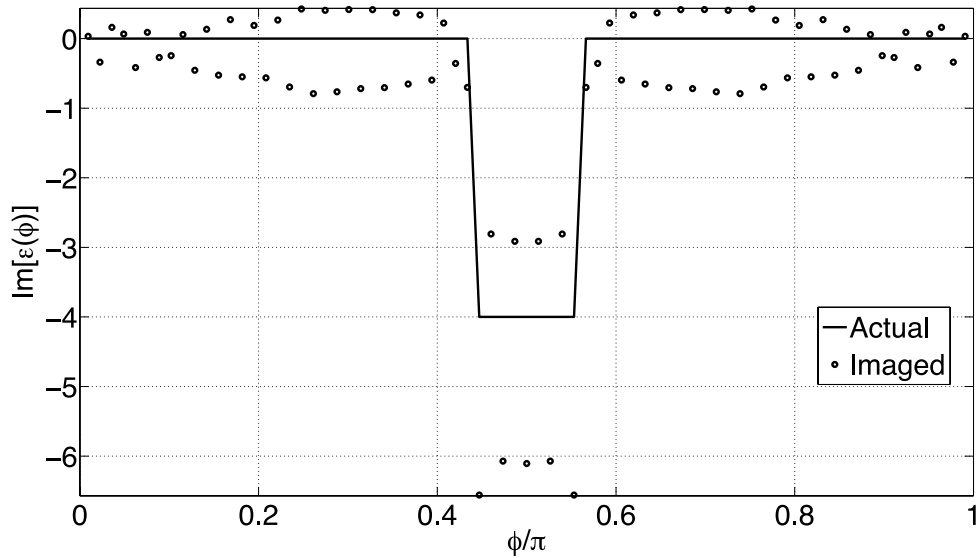


Figure 5.38: When slab thickness is 0.025 meters, imaginary part of reconstructed relative permittivity is compared with the exact relative permittivity in presence of the lens.

Similarly, increased Gibbsian oscillations are also observed in imaginary part of permittivity reconstruction with increase in slab thickness. This is illustrated in Figure 5.37, Figure 5.38, and Figure 5.39 for 0.005 meters, 0.025 meters, and 0.05 meters, respectively. The increased Gibbsian oscillations are believed to be a consequence of increased oscillations within the object of interest. Increased oscillations may be caused by interference of incident field with surface wave excited at the slab ends.

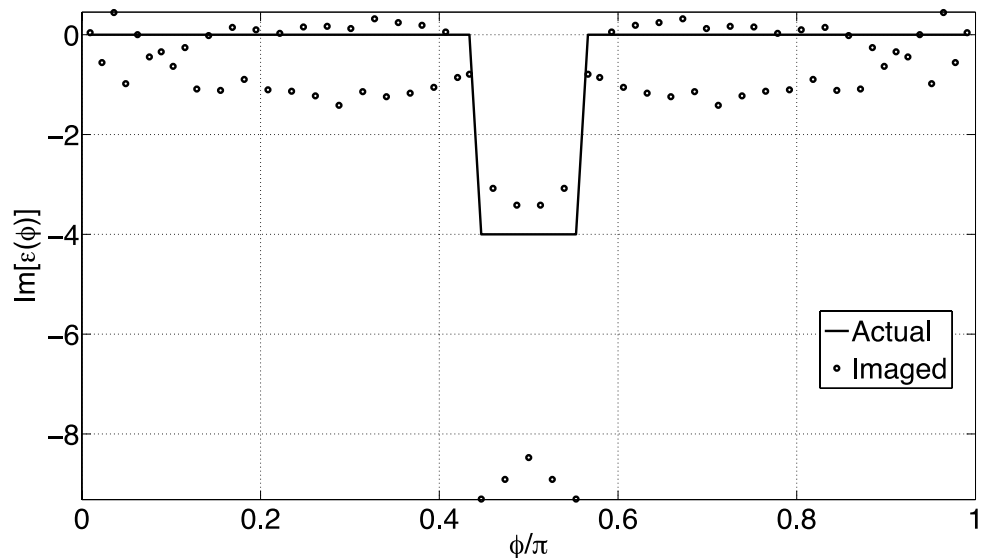


Figure 5.39: When slab thickness is 0.05 meters, imaginary part of reconstructed relative permittivity is compared with the exact relative permittivity in presence of the lens.

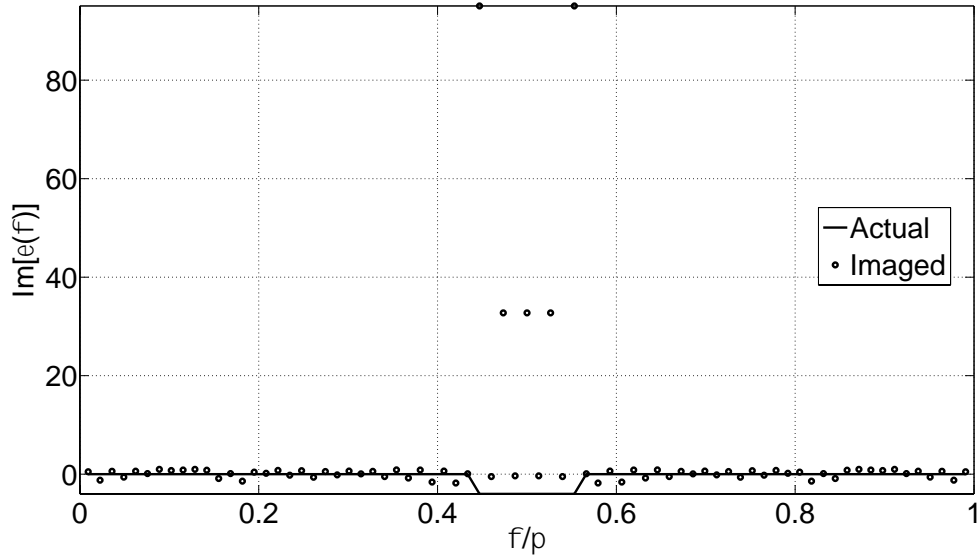


Figure 5.40: When slab thickness is 0.1 meters, imaginary part of reconstructed relative permittivity is compared with the exact relative permittivity in presence of the lens.

The reason we believe is due to a weaker interference caused by surface wave excited in the slab with the incident field. Magnitude of the spatial oscillations becomes low. With the same resolution established by the lens, we can get better capturing of the dielectric distribution over the slab of the imaged object. The effect of surface wave excitation at the edge of a truncated dielectric slab can be found in [9], [10], and [11].

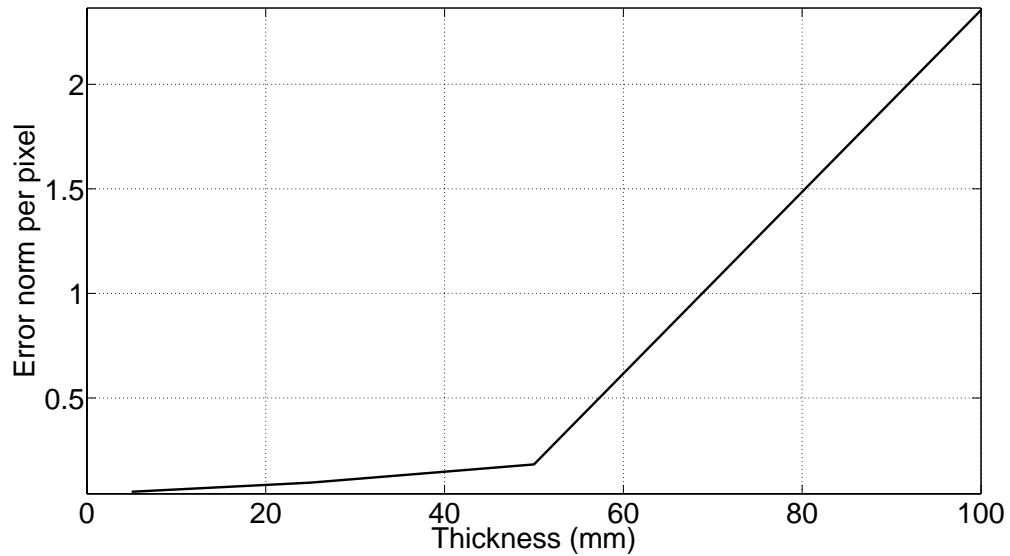


Figure 5.41: Illustration of error norm per pixel variation in presence of lens when thickness is the varied parameter.

In this section, observations listed below are noted:

- Thinner object of interest produces better image reconstruction as shown in Figure 5.41. We believe this is due to surface wave excited at discontinuous ends of the object of interest.
- With increase in thickness of the object of interest, electric field norm within it increases.

5.3 Effect of number of excitation sources

When a single filament source is used for excitation, the result contains very high error as shown in Figure 5.42. We increase sources placing them evenly on an arc ranging

from 0 to π and investigate its effect on the accuracy of reconstruction. We find that with more sources, results are more accurate. We believe, due to fewer oscillations of incident field, fewer electric field oscillations occur in the object of interest. This results in better reconstruction of the permittivity reconstruction. This is illustrated in Figures 5.42 to 5.49.

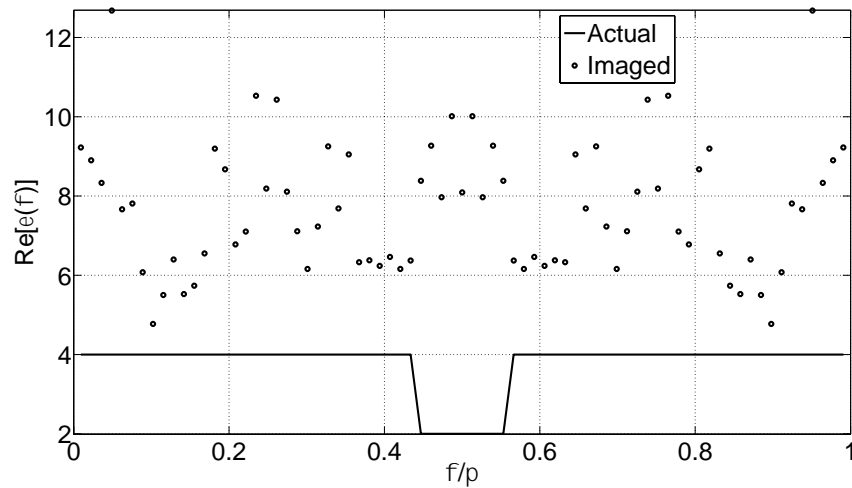


Figure 5.42: Single filament source is used for excitation of the object of interest. The real part of reconstructed relative permittivity is compared to exact relative permittivity.

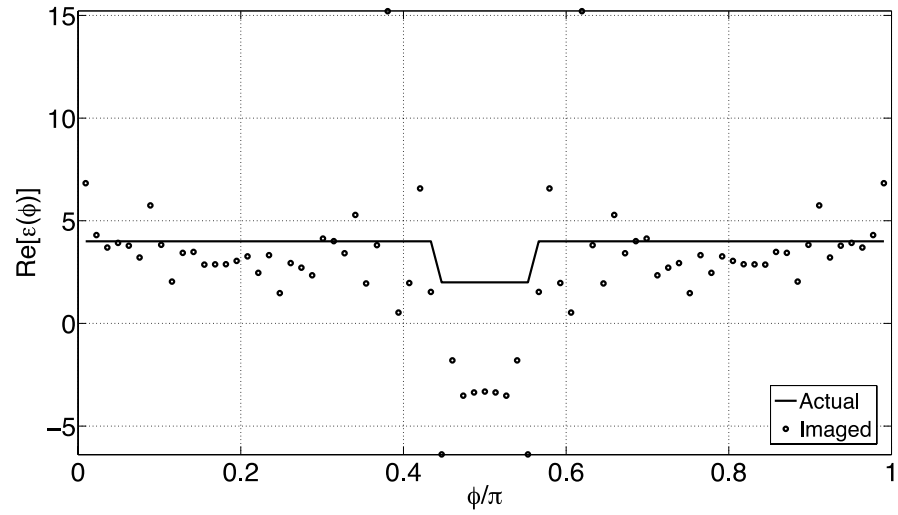


Figure 5.43: 10 filament sources are used for excitation of the object of interest. The real part of reconstructed relative permittivity is compared to exact relative permittivity.

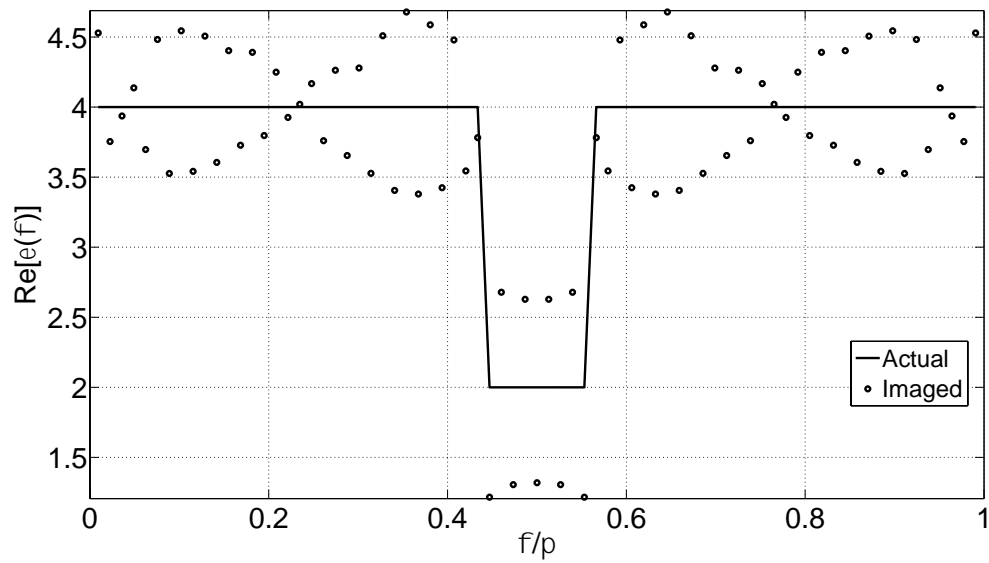


Figure 5.44: 50 filament sources are used for excitation of the object of interest. The real part of reconstructed relative permittivity is compared to exact relative permittivity.

Figures 5.42 to 5.44 shows image reconstruction results with 1 source, 10 sources, and 50 sources interrogating the object of interest, respectively. It can be noted that the image reconstruction accuracy increases with more number of sources placed evenly on the arc ranging from 0 to π .

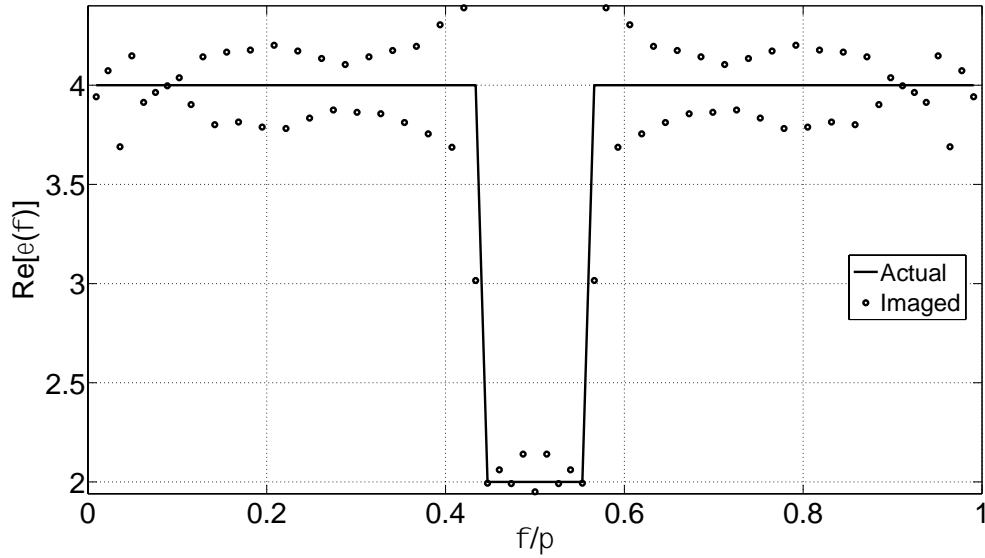


Figure 5.45: 100 filament sources are used for excitation of the object of interest. The real part of reconstructed relative permittivity is compared to exact relative permittivity.

Figure 5.45 and Figure 5.46 shows image reconstruction results when 100 sources and 400 sources are used to excite the object of interest, respectively. Results show more accurate image reconstruction accuracy with respect to the situation when smaller numbers of sources are used for object of interest excitation.

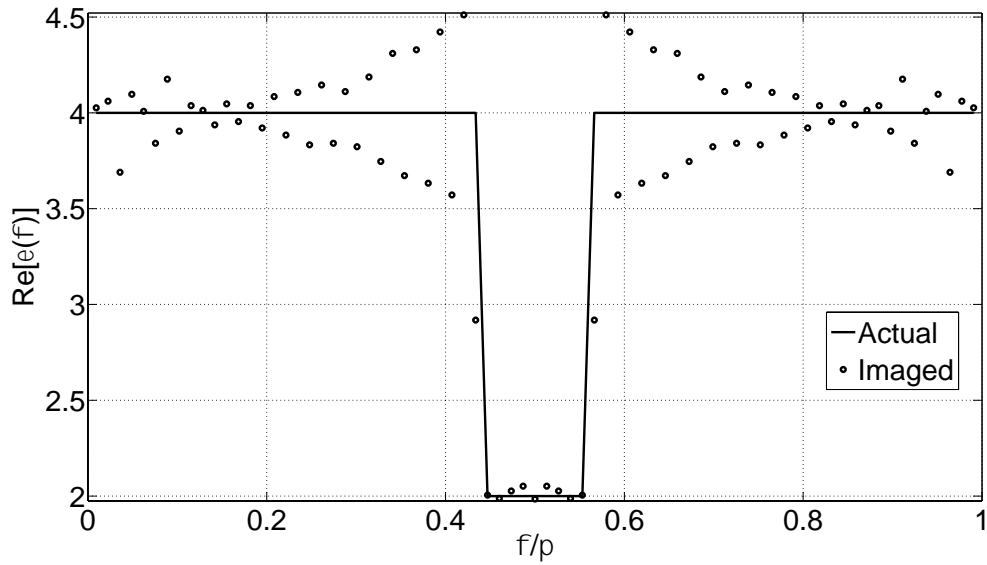


Figure 5.46: 400 filament sources are used for excitation of the object of interest. The real part of reconstructed relative permittivity is compared to exact relative permittivity.

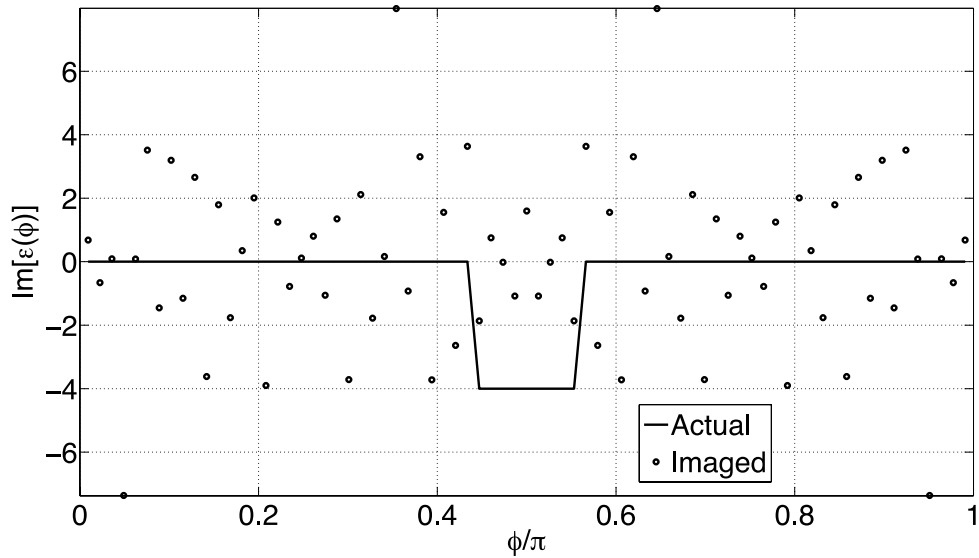


Figure 5.47: Single filament source is used for excitation of the object of interest. The imaginary part of reconstructed relative permittivity is compared to exact relative permittivity.

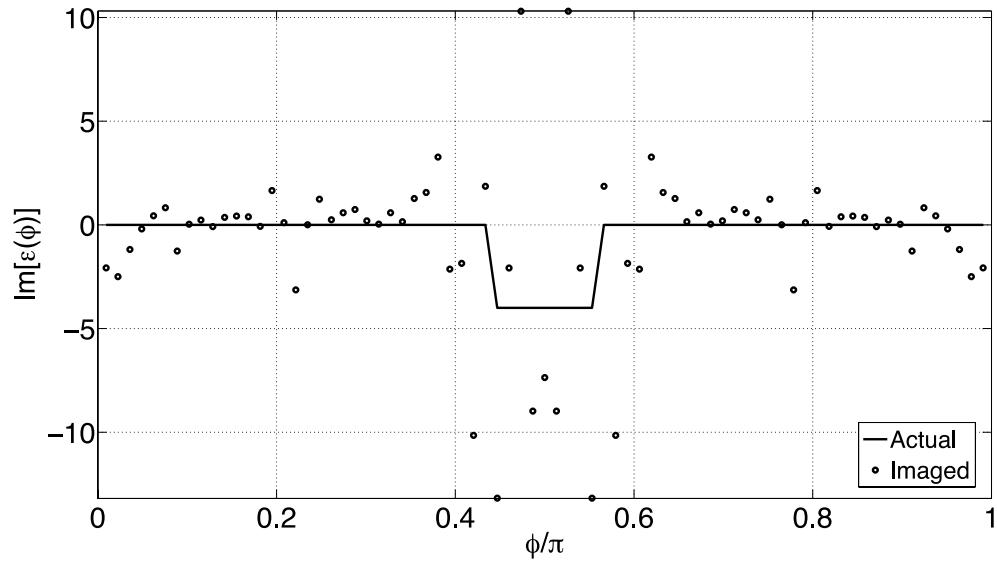


Figure 5.48: 10 filament sources are used for excitation of the object of interest. The imaginary part of reconstructed relative permittivity is compared to exact relative permittivity.

Figure 5.47, Figure 5.48 and Figure 5.49 shows rapid increase in image reconstruction accuracy for 1 source, 10 sources, and 50 sources, respectively. We believe this is due to fewer oscillations in incident field.

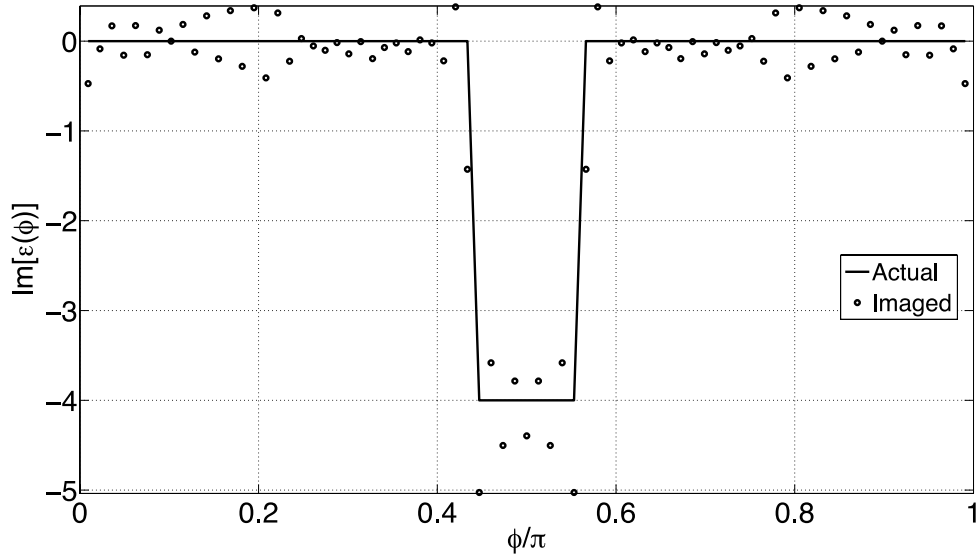


Figure 5.49: 50 filament sources are used for excitation of the object of interest. The imaginary part of reconstructed relative permittivity is compared to exact relative permittivity.

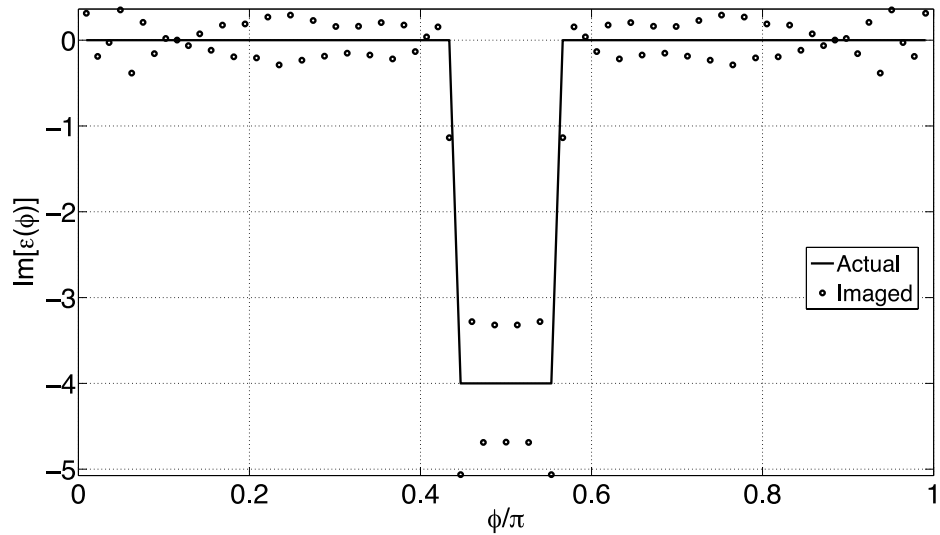


Figure 5.50: 100 filament sources are used for excitation of the object of interest. The imaginary part of reconstructed relative permittivity is compared to exact relative permittivity.

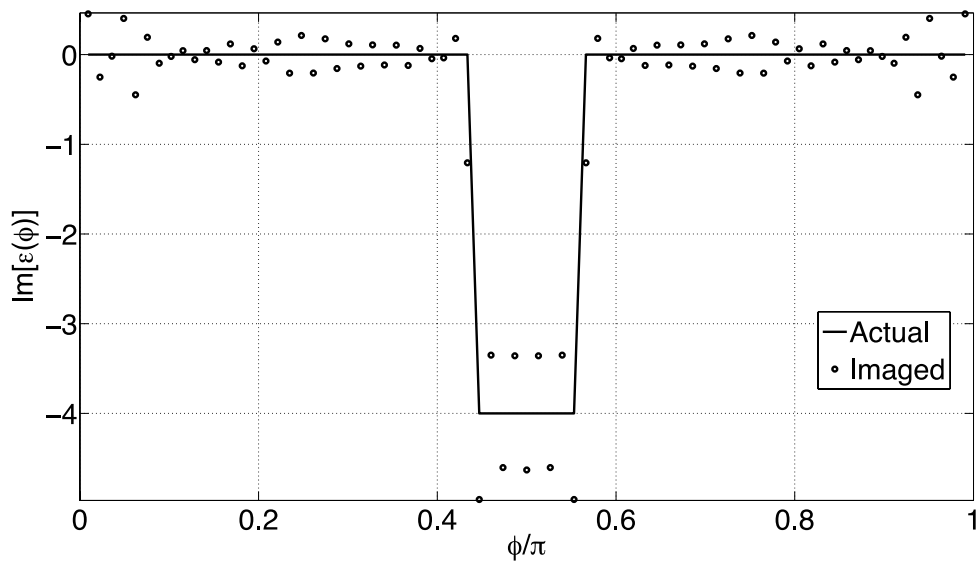


Figure 5.51: 400 filament sources are used for excitation of the object of interest. The imaginary part of reconstructed relative permittivity is compared to exact relative permittivity.

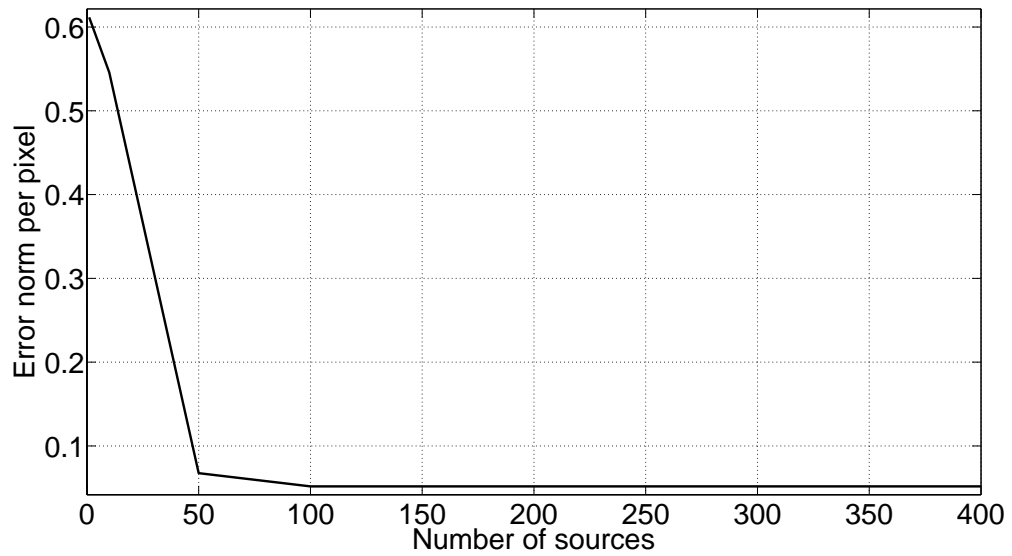


Figure 5.52: Error norm per pixel variation is illustrated when the number of sources is varied.

We have observed incident field has an impact on permittivity reconstruction as illustrated in Figure 5.52. When incident field has less variation on the object of interest, better permittivity reconstruction is observed.

5.4 Effect of frequency variation

In this section, we vary frequency to observe effect on reconstructed image. We take 300 MHz, 450 MHz, and 600 MHz frequency values. When the homogeneous part of background is air, the resolution is 0.25 meters. For homogeneous part of background's relative permittivity 2, 4, 9, and 16, the resolution is 0.1768 meters, 0.1250 meters, 0.0833 meters, and 0.0625 meters, respectively. Results show best reconstruction at high frequency. This is because focal width is narrower at high frequency, as discussed in section 4.6. Focal width is given by equation (4.6.6) as:

$$\Delta\theta = \frac{2}{k_b a}$$

where, a is lens radius, and k_b is wave number in homogeneous part of background. High frequency produces narrow focal width. This produces better reconstruction. Numerical results are illustrated in Figures 5.53 to 5.58.

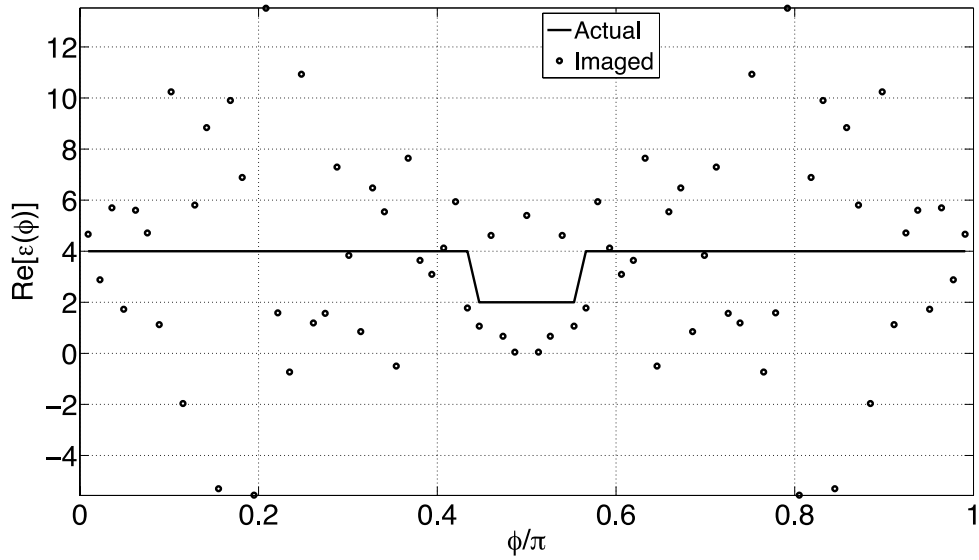


Figure 5.53: When 300 MHz time-harmonic field is used to interrogate object of interest, reconstructed real part of relative permittivity is compared to exact relative permittivity.

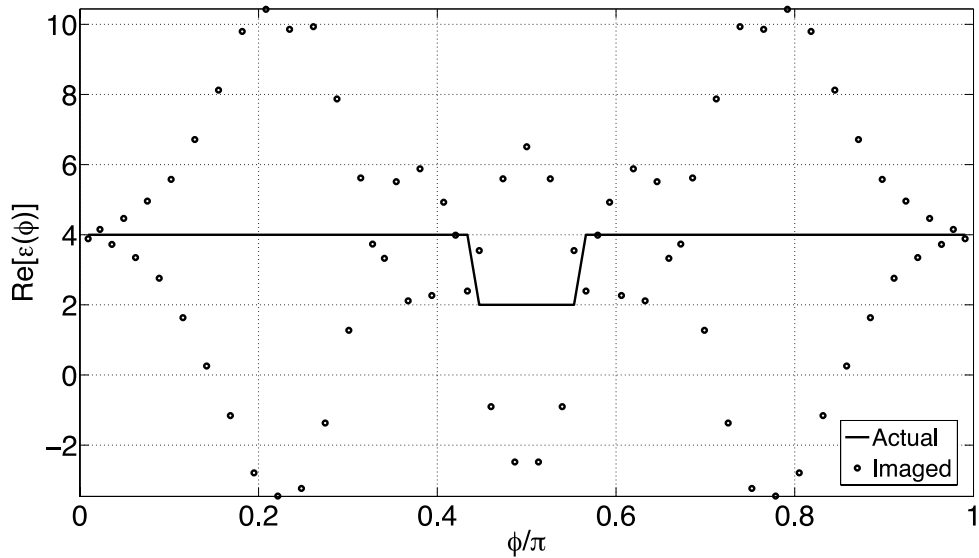


Figure 5.54: When 450 MHz time-harmonic field is used to interrogate object of interest, reconstructed real part of relative permittivity is compared to exact relative permittivity.

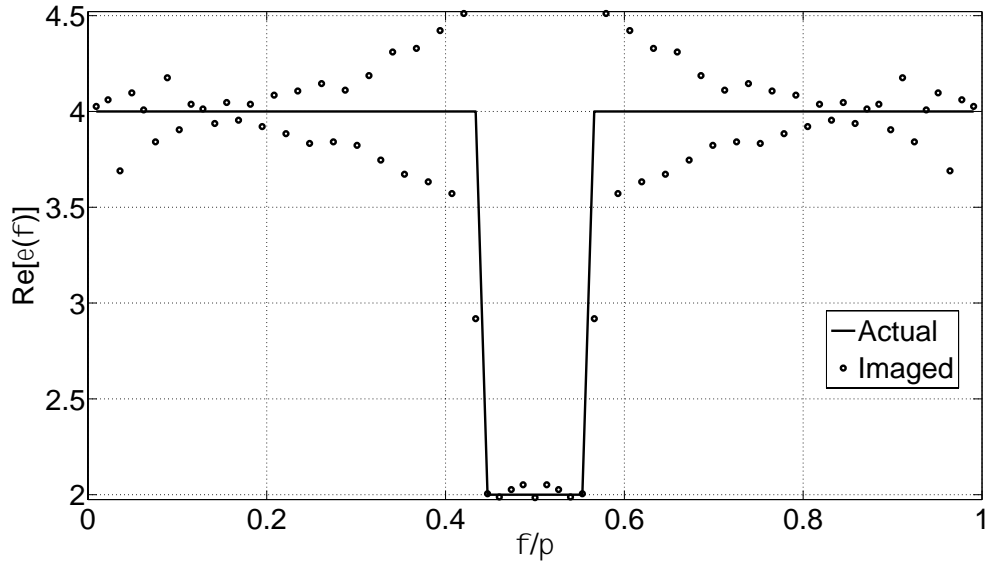


Figure 5.55: When 600 MHz time-harmonic field is used to interrogate object of interest, reconstructed real part of relative permittivity is compared to exact relative permittivity.

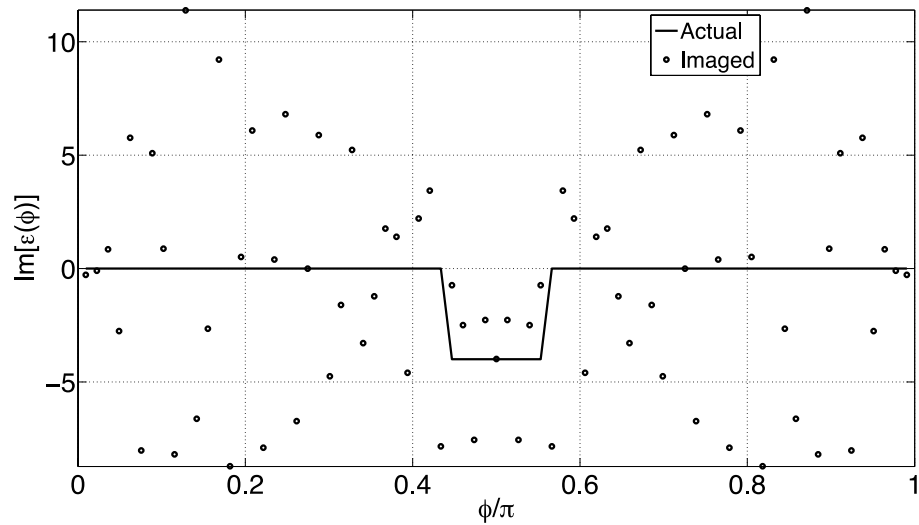


Figure 5.56: When 300 MHz time-harmonic field is used to interrogate object of interest, reconstructed imaginary part of relative permittivity is compared to exact relative permittivity.

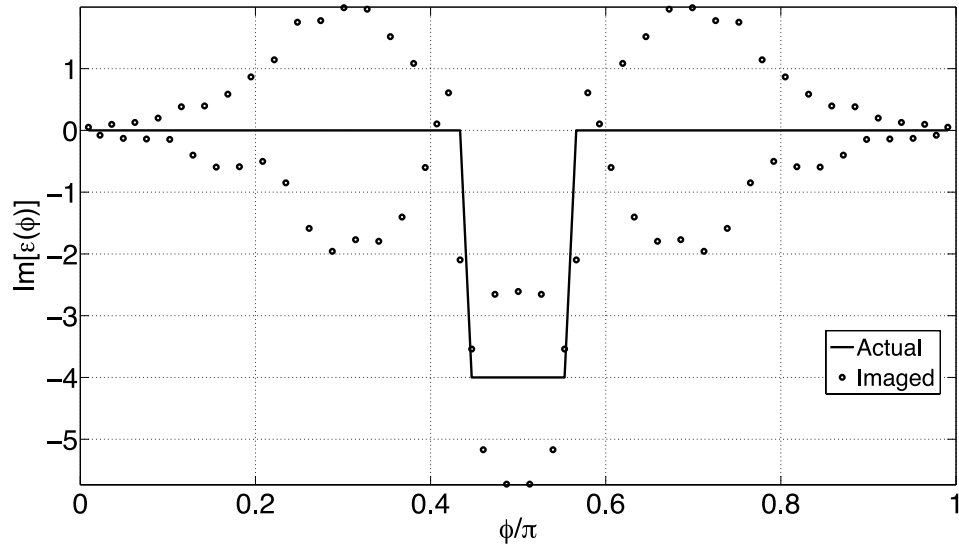


Figure 5.57: When 450 MHz time-harmonic field is used to interrogate object of interest, reconstructed imaginary part of relative permittivity is compared to exact relative permittivity.

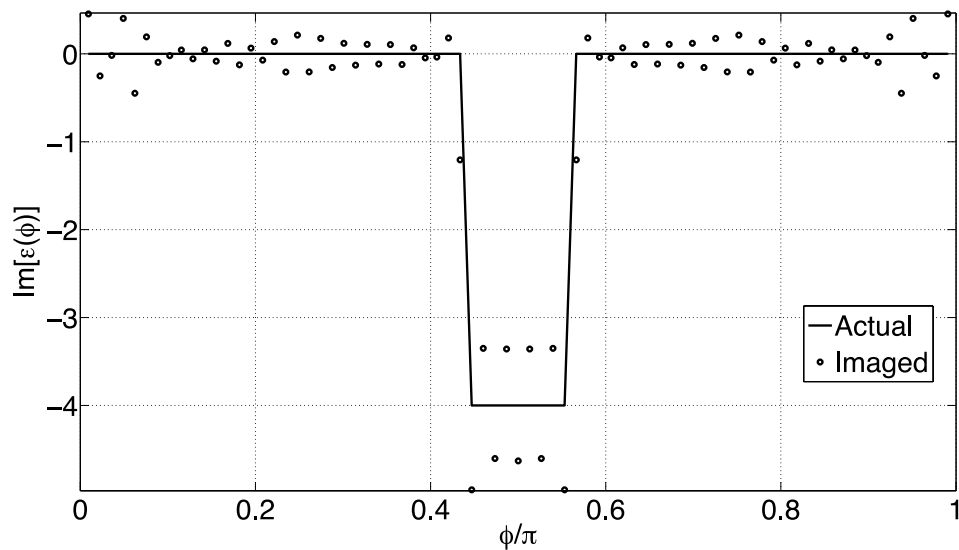


Figure 5.58: When 600 MHz time-harmonic field is used to interrogate object of interest, reconstructed imaginary part of relative permittivity is compared to exact relative permittivity.

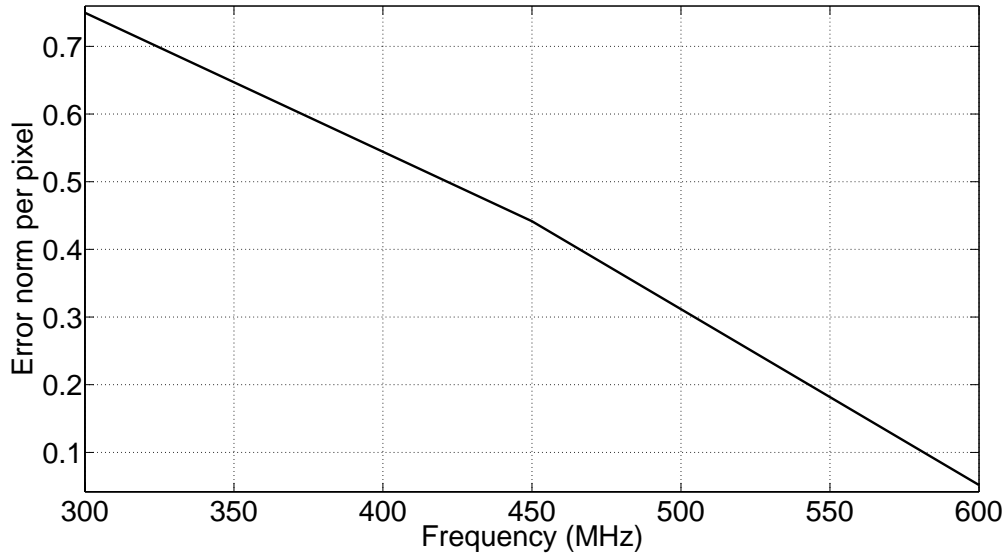


Figure 5.59: Illustration of error norm per pixel variation when different frequencies are employed to reconstruct the object of interest.

We note better permittivity reconstruction at high frequencies. This is illustrated in Figure 5.59. Higher frequency increases electrical size of the Maxwell fish-eye lens used. Hence, focal width is also reduced in high frequency cases as discussed in Section 4.6. This results in better permittivity reconstruction.

5.5 Higher resolution

From section 5.1, we observed acceptable accuracy with $\frac{\lambda_b}{2}$ resolution; where, λ_b is wavelength in homogeneous part of background. Figure 5.60 shows Green's function

norm when resolution is $\frac{\lambda_b}{2}$. The figure shows focal beams well separated at this resolution. Higher resolution will bring the focal beams closer overlapping each other. This will increase higher contribution from adjacent pixels at the observation location. This will decrease achieved well-posedness and hence, result in poor image reconstruction. In this section, we set our resolution to $\frac{\lambda_b}{4}$ and keep the other parameters same. From numerical results, we observe reconstructed image loses accuracy as shown in Figures 5.61 to 5.70.

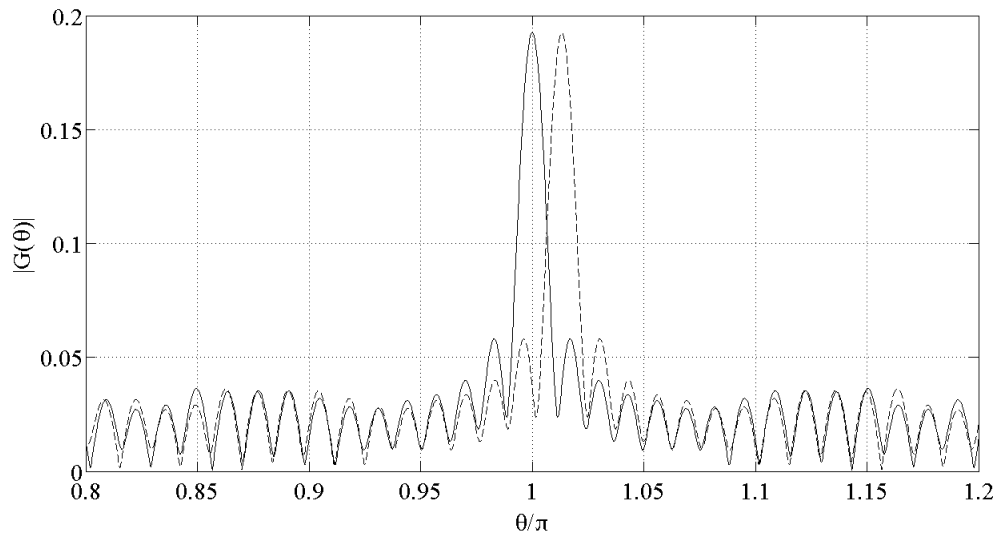


Figure 5.60: Norm of Green's function over angular distribution when the resolution is $\frac{\lambda_b}{2}$; where, λ_b is wavelength in homogeneous part of background.

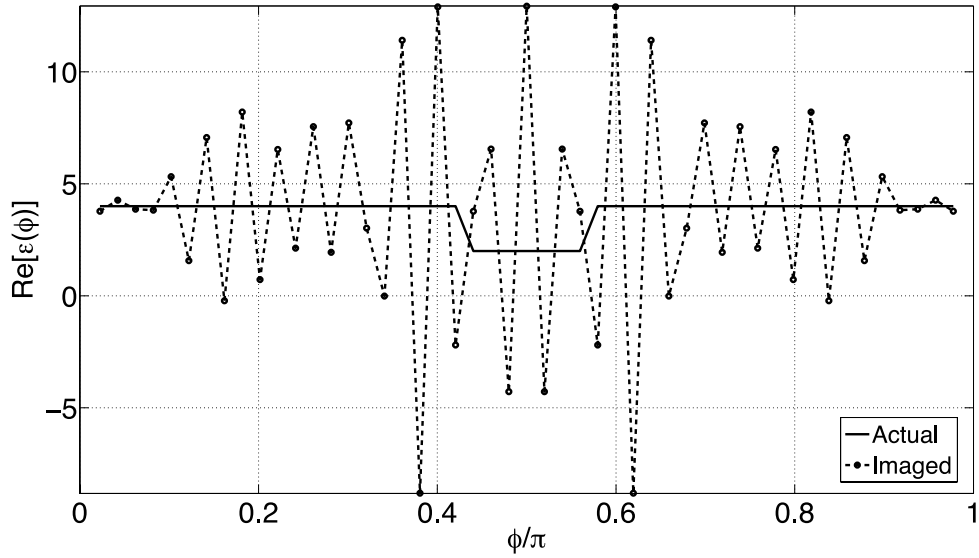


Figure 5.61: When air is in homogeneous part of background, real part of relative permittivity reconstruction is compared to exact relative permittivity.

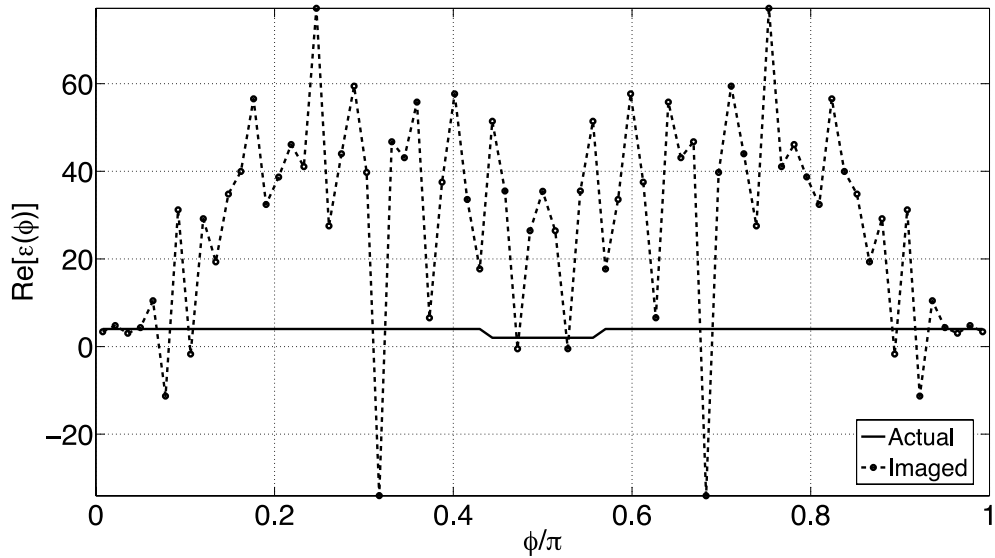


Figure 5.62: Real part of relative permittivity reconstruction is compared to exact relative permittivity when homogeneous part of background has relative permittivity 2.

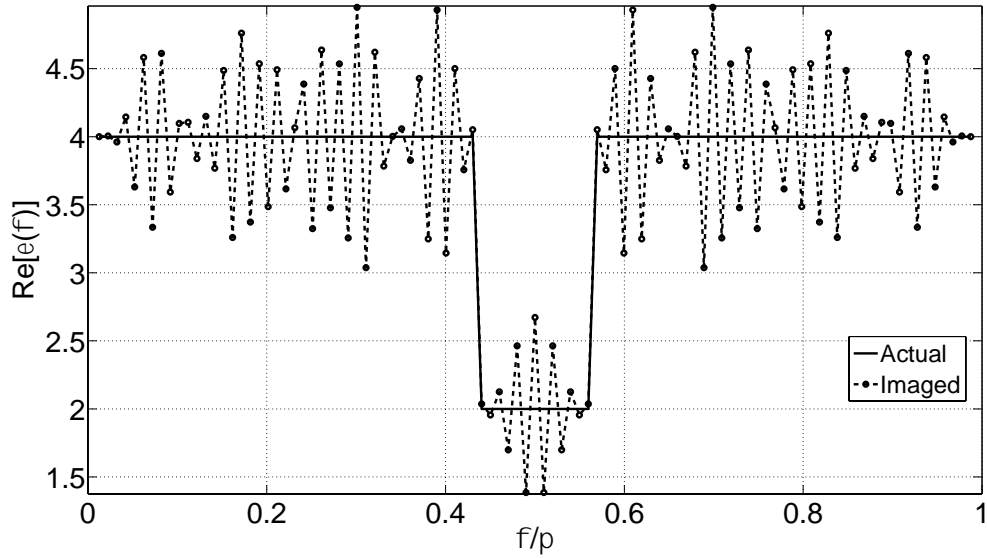


Figure 5.63: Real part of relative permittivity reconstruction is compared to exact relative permittivity when homogeneous part of background has relative permittivity 4.

We note that low contrast produces better image reconstruction. Also, we note that results lose accuracy when contrast is increased. More image reconstruction accuracy was obtained with $\frac{\lambda_b}{2}$ resolution with higher contrast.

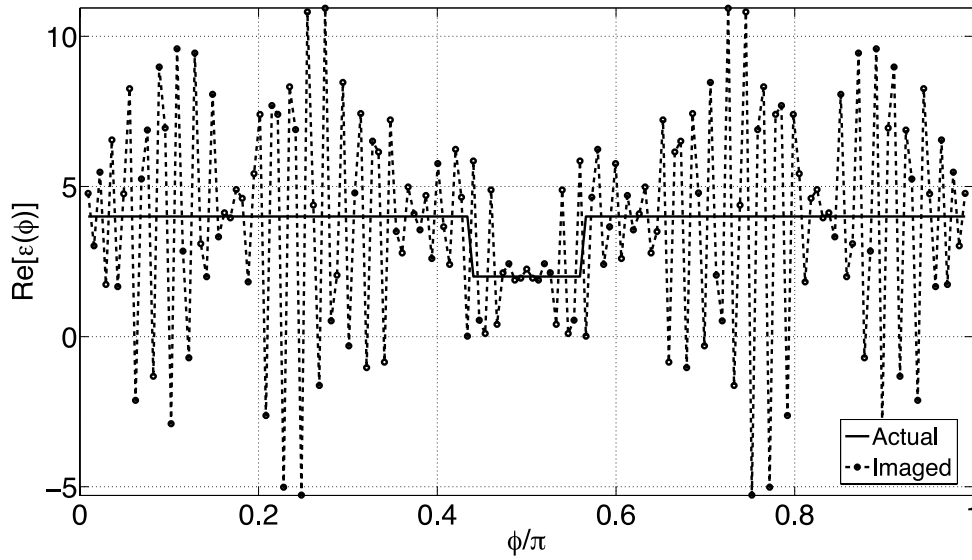


Figure 5.64: Real part of relative permittivity reconstruction is compared to exact relative permittivity when homogeneous part of background has relative permittivity 9.

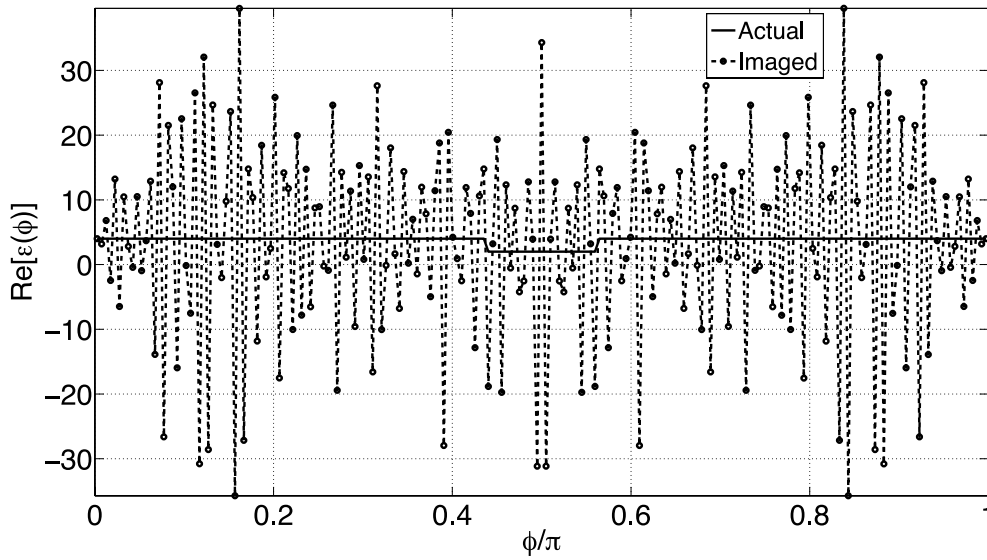


Figure 5.65: Real part of relative permittivity reconstruction is compared to exact relative permittivity when homogeneous part of background has relative permittivity 16.

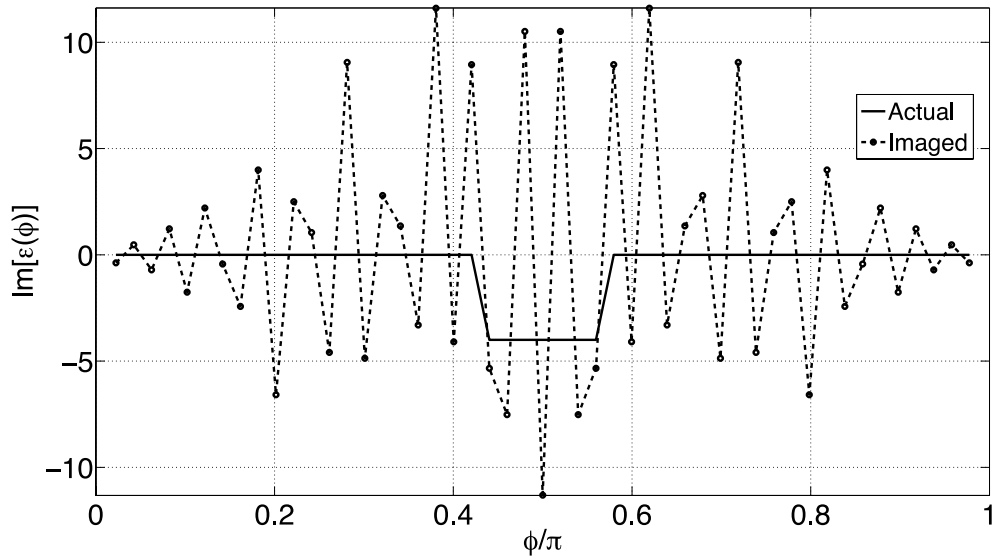


Figure 5.66: When air is in homogeneous part of background, imaginary part of relative permittivity reconstruction is compared to exact relative permittivity.

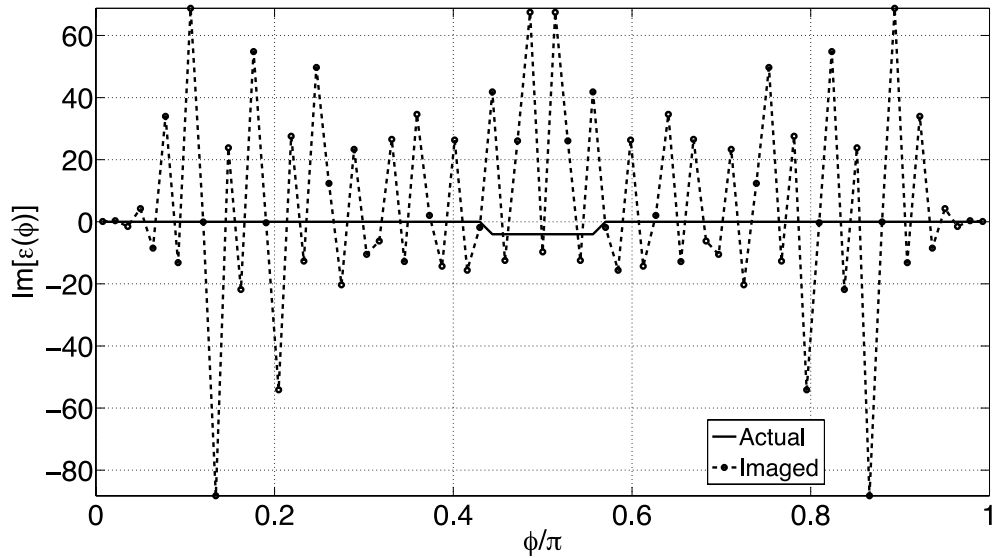


Figure 5.67: Imaginary part of relative permittivity reconstruction is compared to exact relative permittivity when homogeneous part of background has relative permittivity 2.

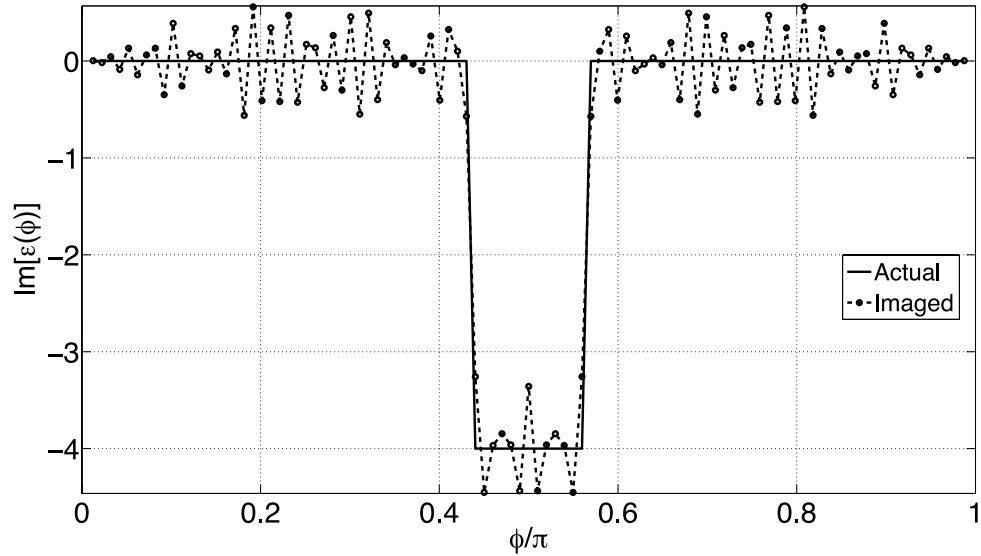


Figure 5.68: Imaginary part of relative permittivity reconstruction is compared to exact relative permittivity when homogeneous part of background has relative permittivity 4.

Imaginary part of permittivity reconstruction exhibits the same characteristics as of real part of permittivity reconstruction. Gibbsian oscillations increase with higher contrast. Low contrast gives more accurate results. With $\frac{\lambda_b}{2}$ resolution, we can reconstruct higher contrast with low inaccuracy in result compared to $\frac{\lambda_b}{4}$ resolution.

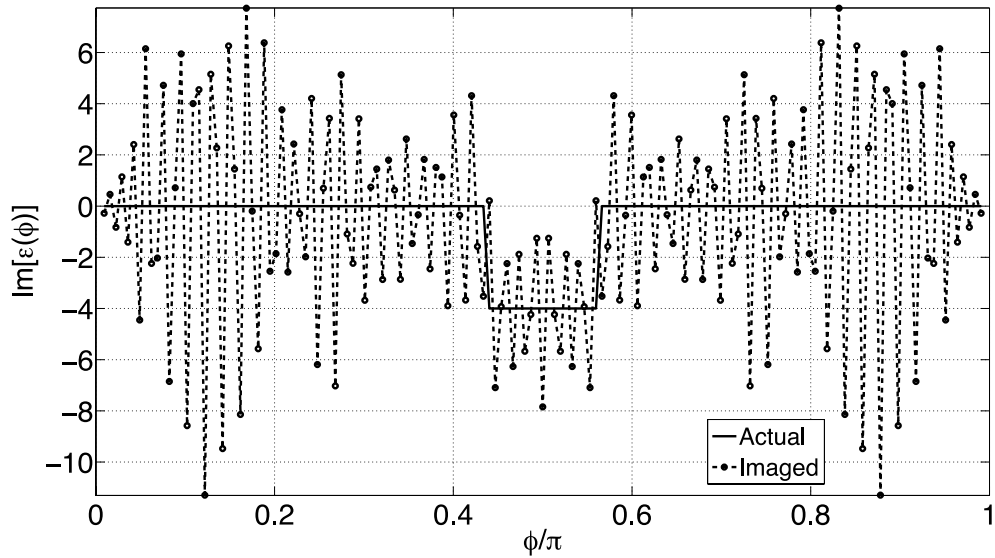


Figure 5.69: Imaginary part of relative permittivity reconstruction is compared to exact relative permittivity when homogeneous part of background has relative permittivity 9.

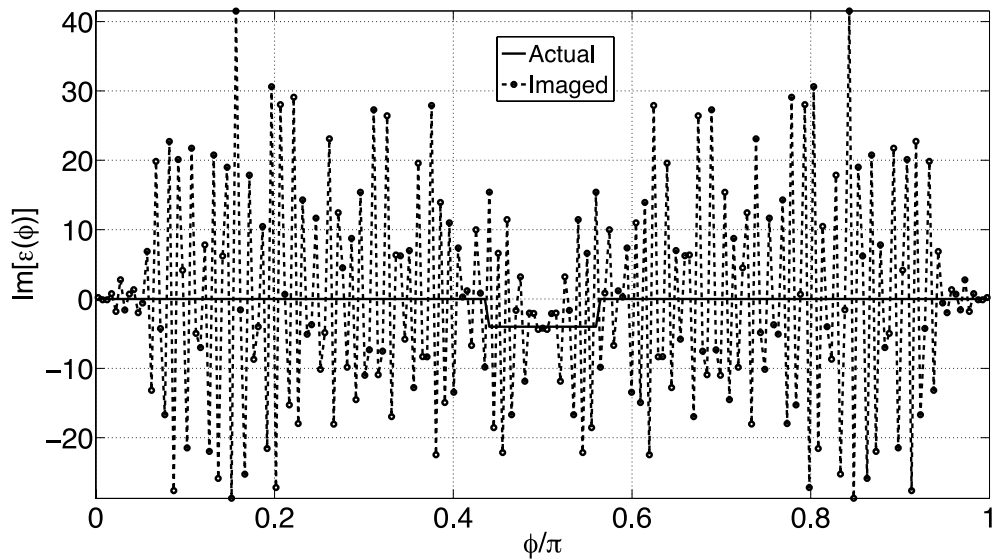


Figure 5.70: Imaginary part of relative permittivity reconstruction is compared to exact relative permittivity when homogeneous part of background has relative permittivity 16.

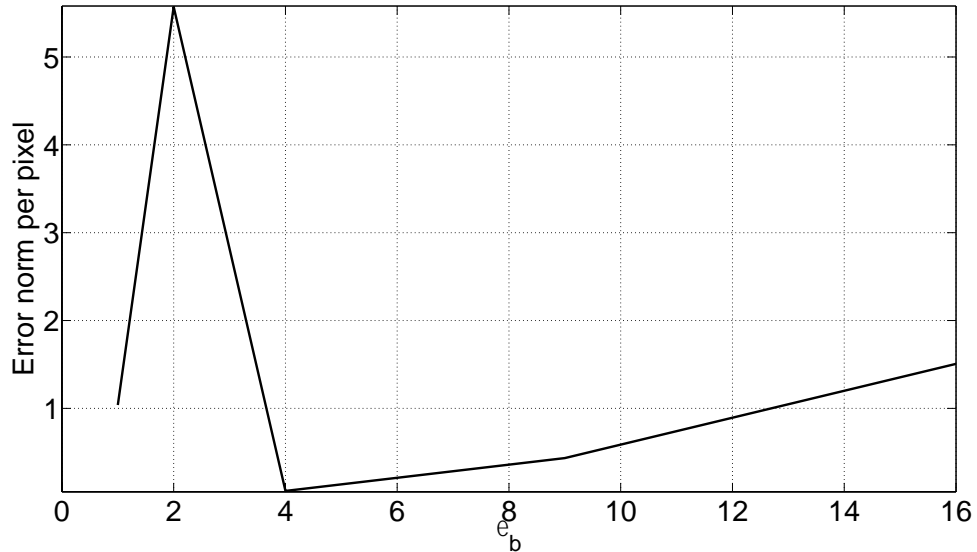


Figure 5.71: When we attempt to reconstruct permittivity at higher resolution, error norm per pixel variation is illustrated.

In the attempts to obtain higher resolution permittivity reconstruction, we have observed the following:

- When we attempt permittivity reconstruction at higher resolution, Gibbsian ringing increases. We believe this is due to loss of well-posedness when resolution is increased.
- Lower contrast exhibits lower Gibbsian ringing.

5.6 COMSOL Verification

We have used custom written method of moment code using Mie series to obtain Green's function for 11-layer Maxwell fish-eye lens to solve forward problem. To verify

the results, we solved the same problem using commercial off-the-shelf software: COMSOL [12].

We used COMSOL to solve forward problems. We use field values from COMSOL to solve inverse source problem. Subsequently, we apply volumetric equivalence principle to obtain contrast, $(\epsilon(\mathbf{r}) - \epsilon_b)$, within the body of interest; where, ϵ_b is homogeneous part of background's relative permittivity. These results further verify our proposed technique of posing inverse problem in well-posed form through appropriate background choice. Following figures illustrate relative permittivity reconstruction. The figures show higher ringing in case of higher contrast. We believe this is due to COMSOL's numerical error in forward problem solution.

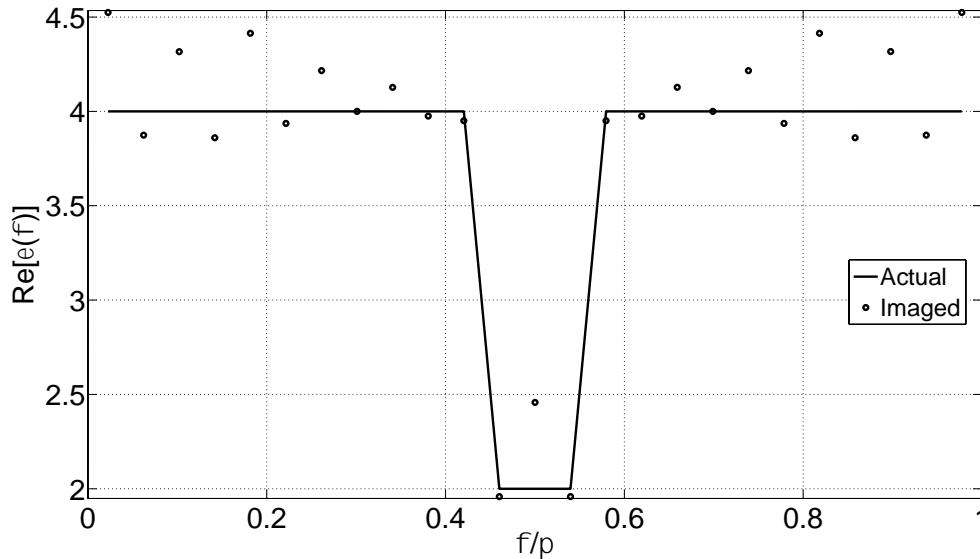


Figure 5.72: Real part of reconstructed relative permittivity is compared to exact relative permittivity distribution when homogeneous part of background is air.

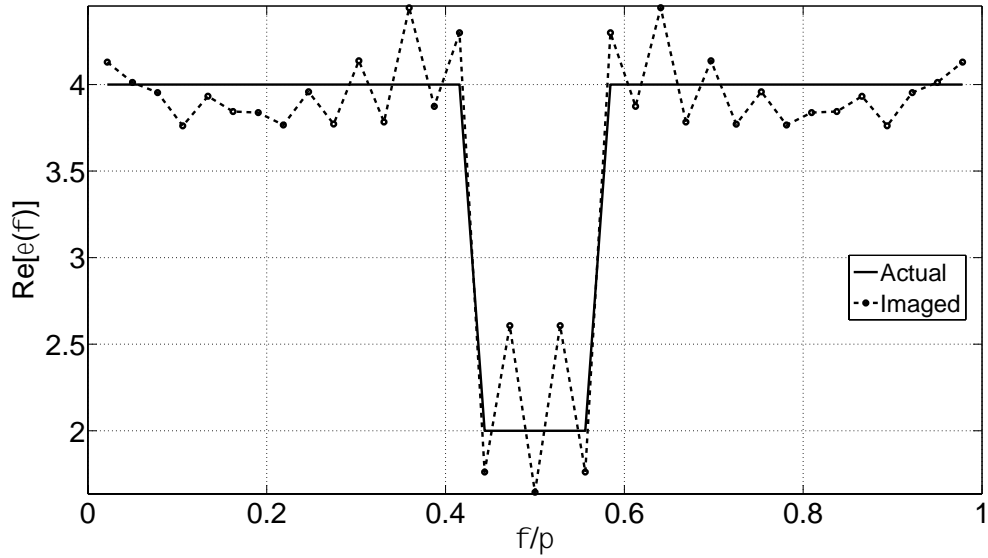


Figure 5.73: Real part of reconstructed relative permittivity is compared to exact relative permittivity distribution when homogeneous part of background is 2.

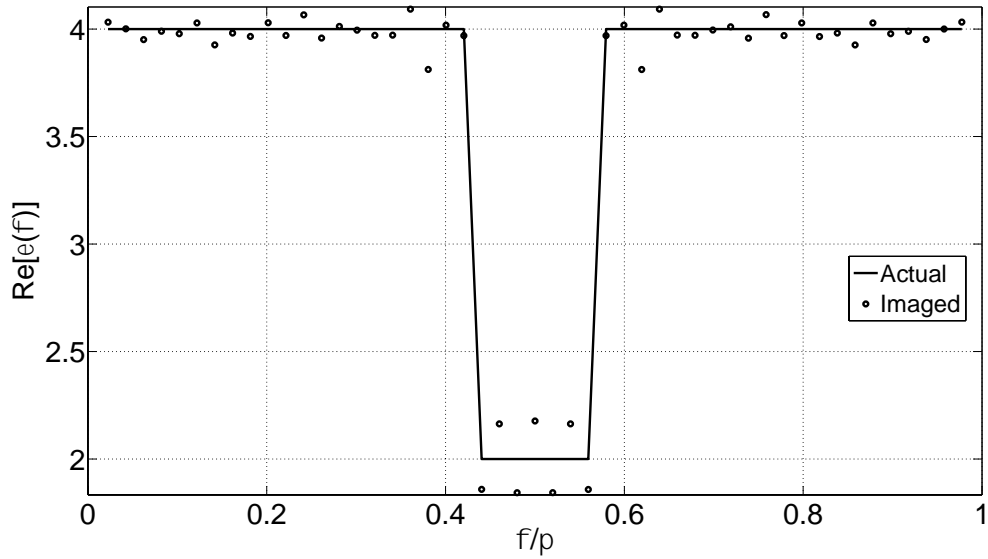


Figure 5.74: Real part of reconstructed relative permittivity is compared to exact relative permittivity distribution when homogeneous part of background is 4.

Gibbsian oscillations are found to decrease with low contrast reconstruction. Figure 5.74 is with the lowest contrast and is found to reconstruct image with lowest Gibbsian oscillations. Figure 5.76 is image reconstructed with relative permittivity 16 in homogeneous part of background. It shows highest Gibbsian oscillations in the image.

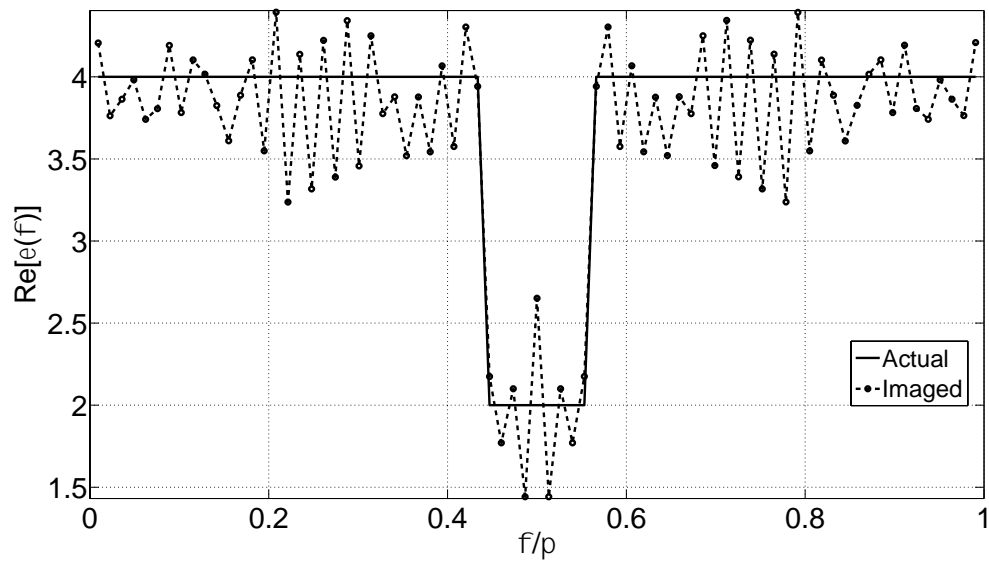


Figure 5.75: Real part of reconstructed relative permittivity is compared to exact relative permittivity distribution when homogeneous part of background is 9.

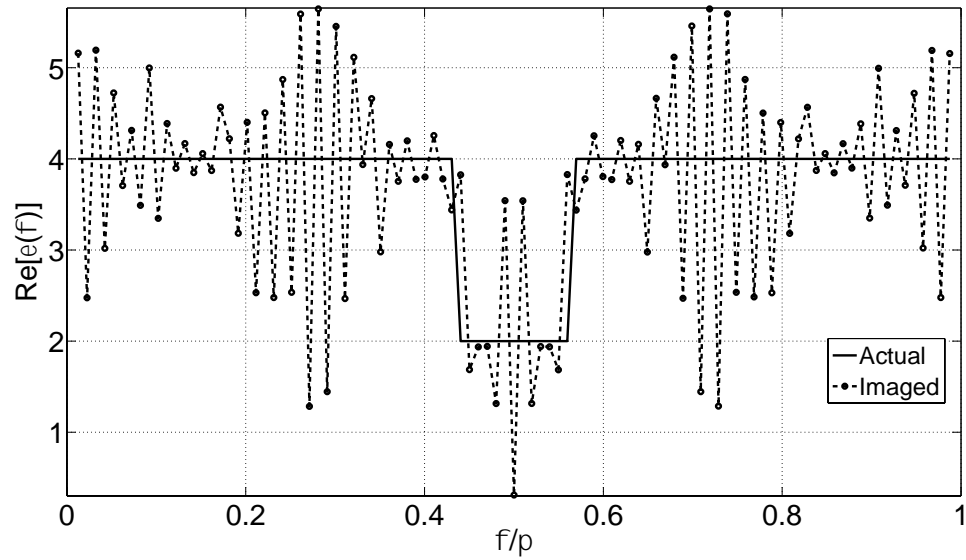


Figure 5.76: Real part of reconstructed relative permittivity is compared to exact relative permittivity distribution when homogeneous part of background is 16.

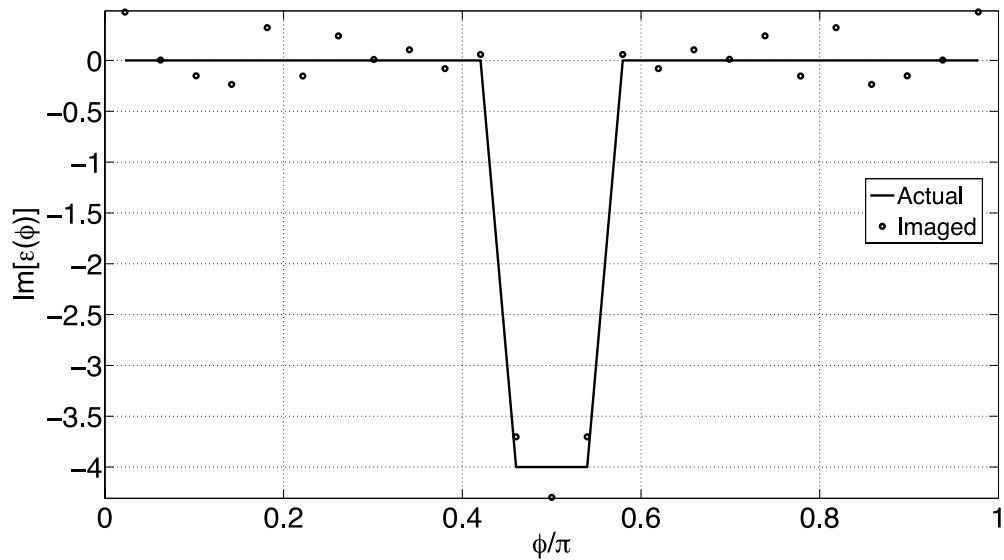


Figure 5.77: Imaginary part of reconstructed relative permittivity is compared to exact relative permittivity distribution when homogeneous part of background is air.

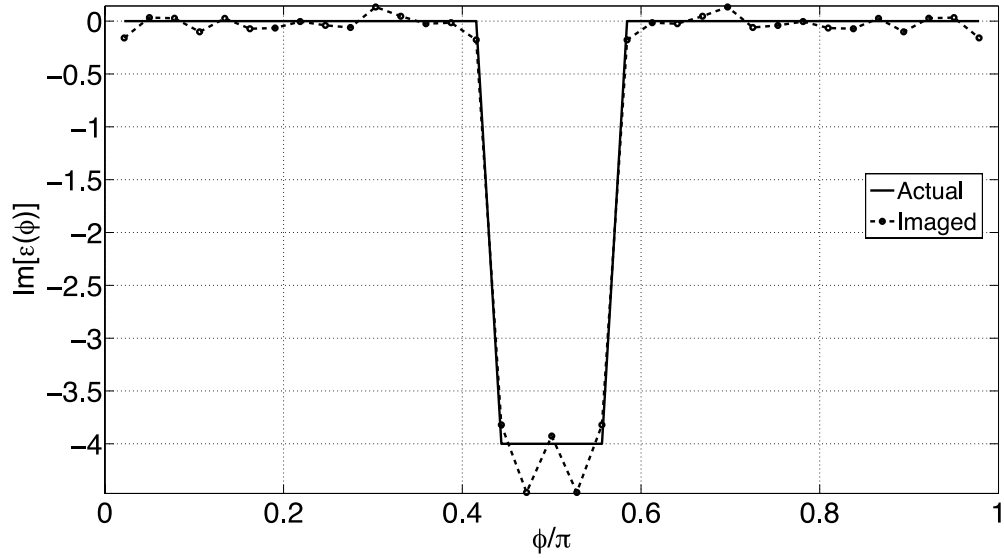


Figure 5.78: Imaginary part of reconstructed relative permittivity is compared to exact relative permittivity distribution when homogeneous part of background is 2.

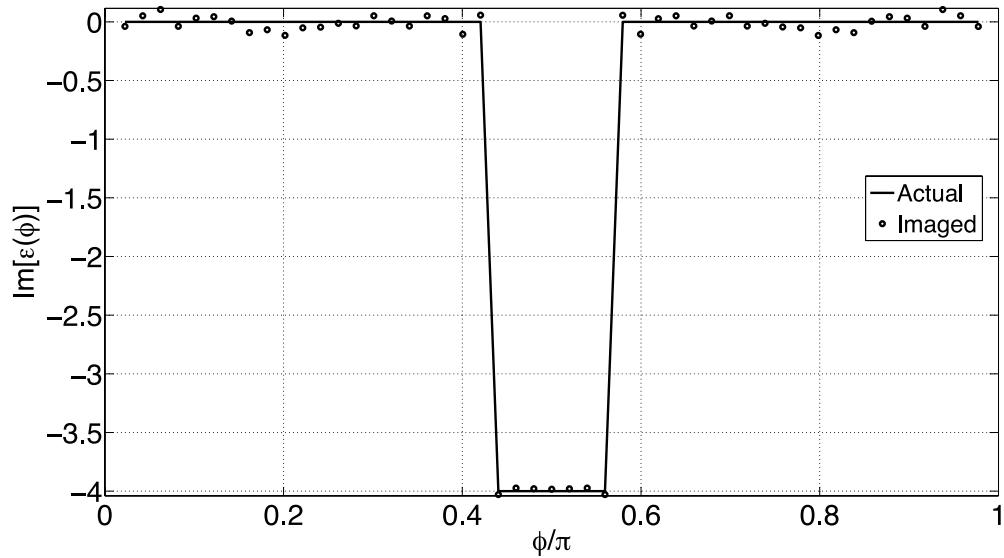


Figure 5.79: Imaginary part of reconstructed relative permittivity is compared to exact relative permittivity distribution when homogeneous part of background is 4.

Imaginary part and real part of permittivity reconstruction show similar characteristics. Low contrast produces more accurate image. Figure 5.79 is reconstructed permittivity with lowest contrast; whereas, Figure 5.81 is with highest contrast. More inaccuracy is obtained due to more Gibbsian oscillations in high contrast permittivity reconstruction.

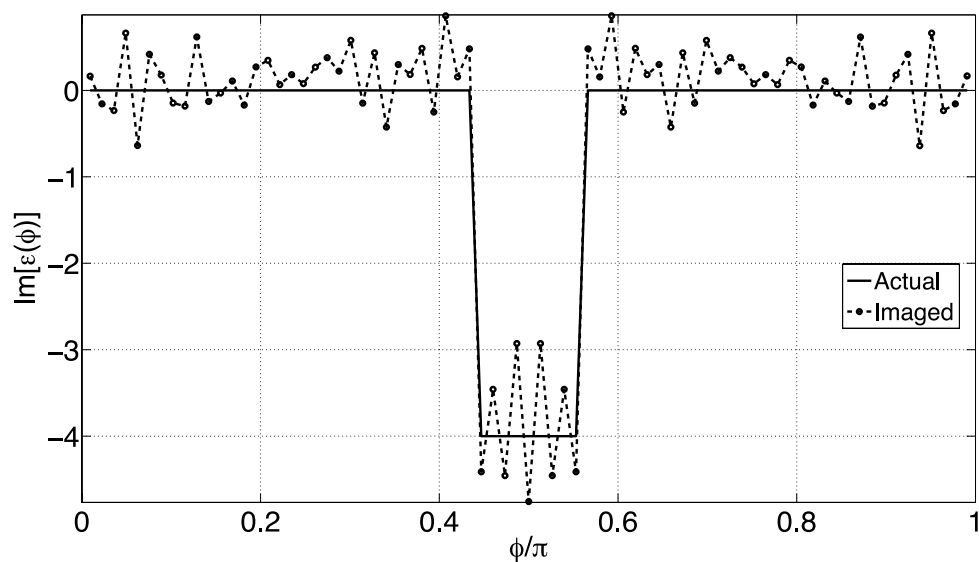


Figure 5.80: Imaginary part of reconstructed relative permittivity is compared to exact relative permittivity distribution when homogeneous part of background is 9.

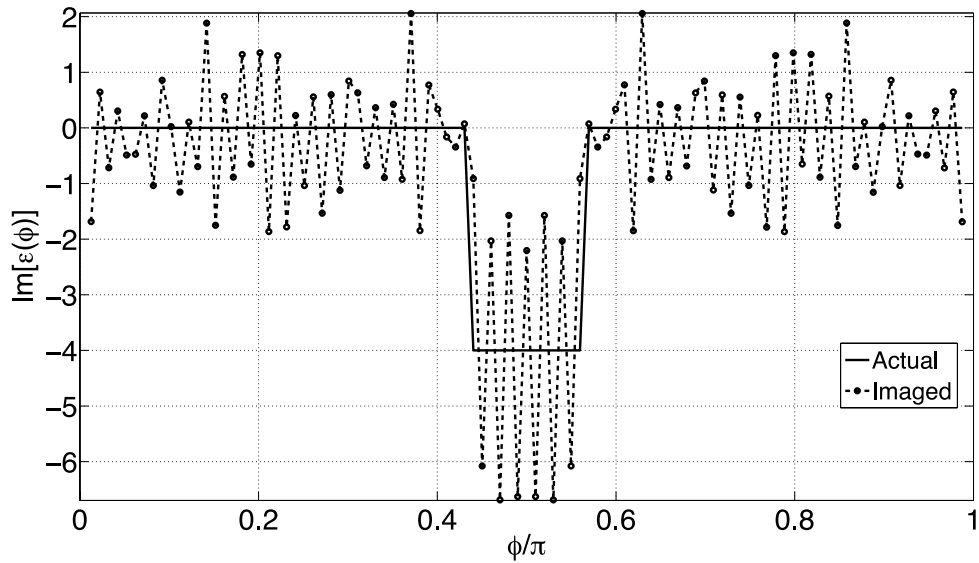


Figure 5.81: Imaginary part of reconstructed relative permittivity is compared to exact relative permittivity distribution when homogeneous part of background is 16.

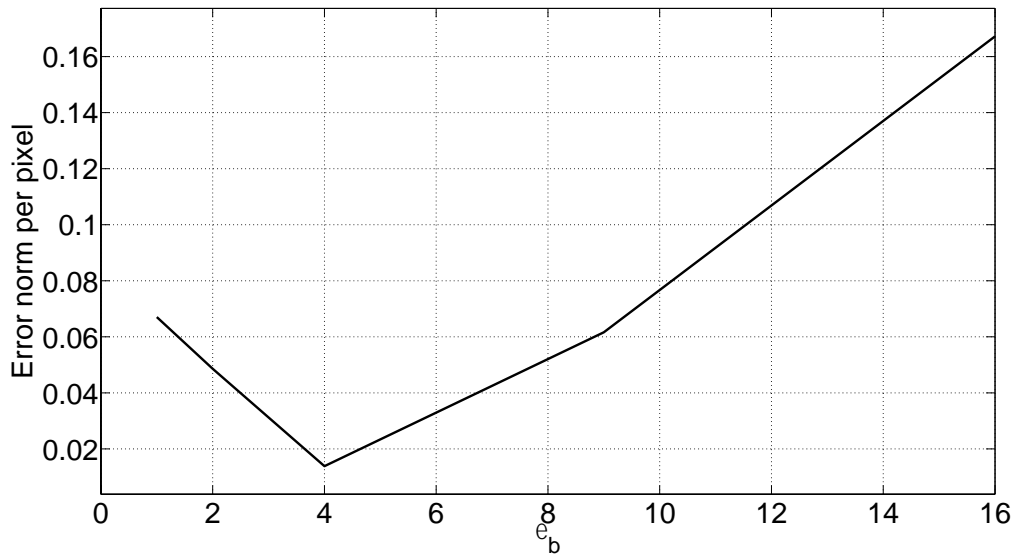


Figure 5.82: Error norm per pixel variation is illustrated when we confirm our proposed technique using COMSOL.

We observed following observations in this section:

- We have been able to confirm validity of our proposed technique using forward problem solutions from a different solver.
- Also, these results confirm that we have not committed inverse crime.

5.7 Noisy data

In this section, we test our method with various signal-to-noise ratio (SNR). These results show robustness of solution using the proposed method. When less noise is introduced, we observe better permittivity reconstruction. Also, we observe that low signal-to-noise ratio (SNR), i.e. high noise, give us low permittivity reconstruction error. This shows robustness of our method. Also, it confirms that inverse crime is not performed.

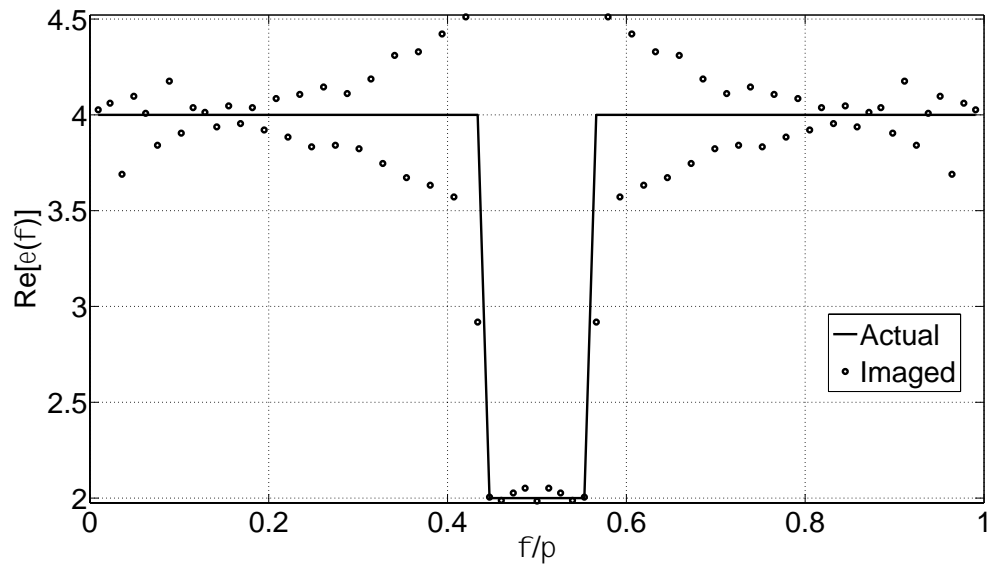


Figure 5.83: With no noise added, real part of reconstructed relative permittivity is illustrated.

Figure 5.83 and Figure 5.84 show real part of relative permittivity reconstruction. We present permittivity reconstruction without added noise in Figure 5.83. With signal-to-noise ratio (SNR) 20, as shown in Figure 5.84, permittivity reconstruction shows small increase in reconstruction error.

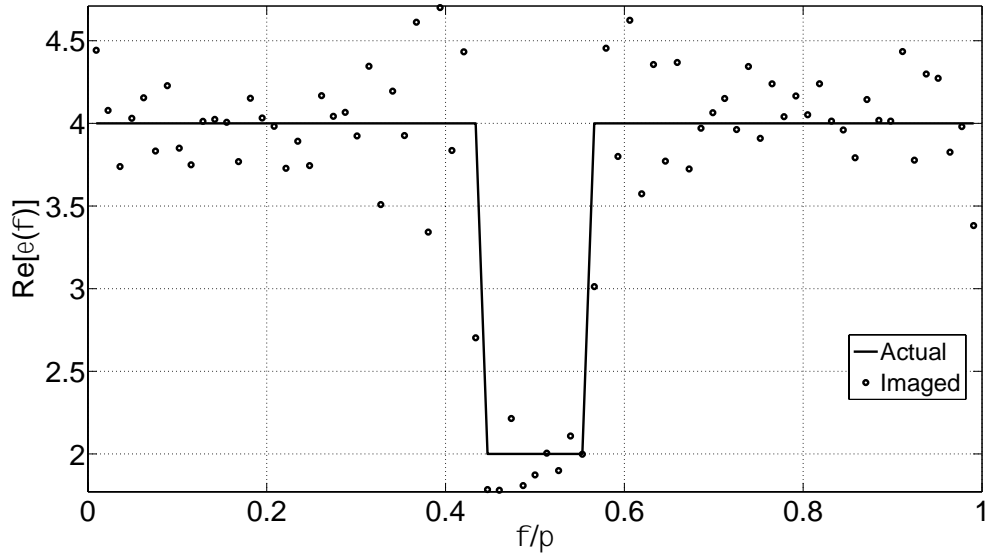


Figure 5.84: When signal-to-noise ratio (SNR) is 20, real part of reconstructed permittivity distribution is compared to true permittivity distribution.

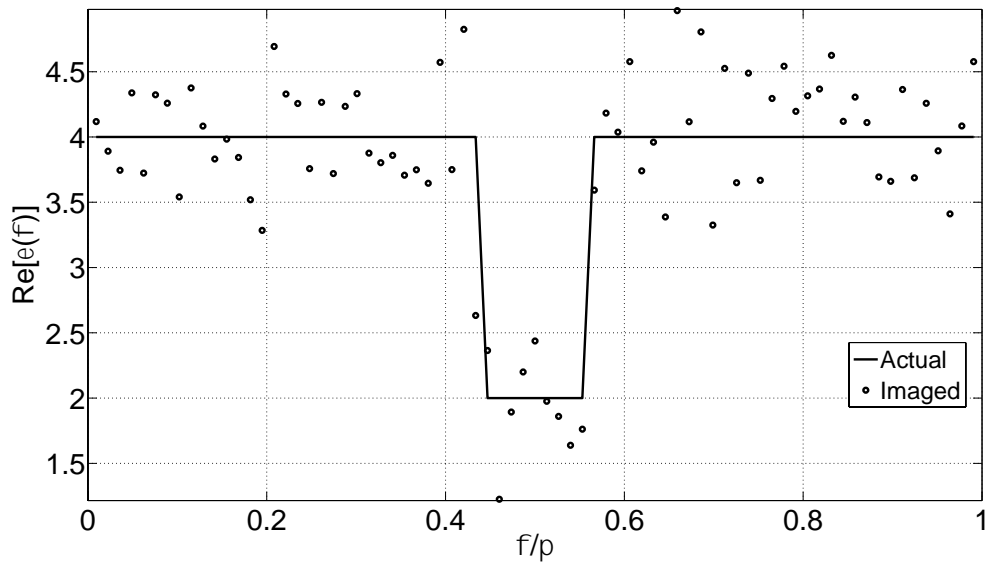


Figure 5.85: Real part of reconstructed permittivity distribution compared to true permittivity distribution when signal-to-noise ratio (SNR) is 10.

When the signal-to-noise ratio (SNR) is decreased to 10, error in inverse problem solution increased as shown in Figure 5.85. Figure 5.86 shows real permittivity reconstruction with signal-to-noise ratio (SNR) 5. Error in inverse problem solution is found to be less sensitive with lower signal-to-noise ratios (SNR), i.e. higher noise.

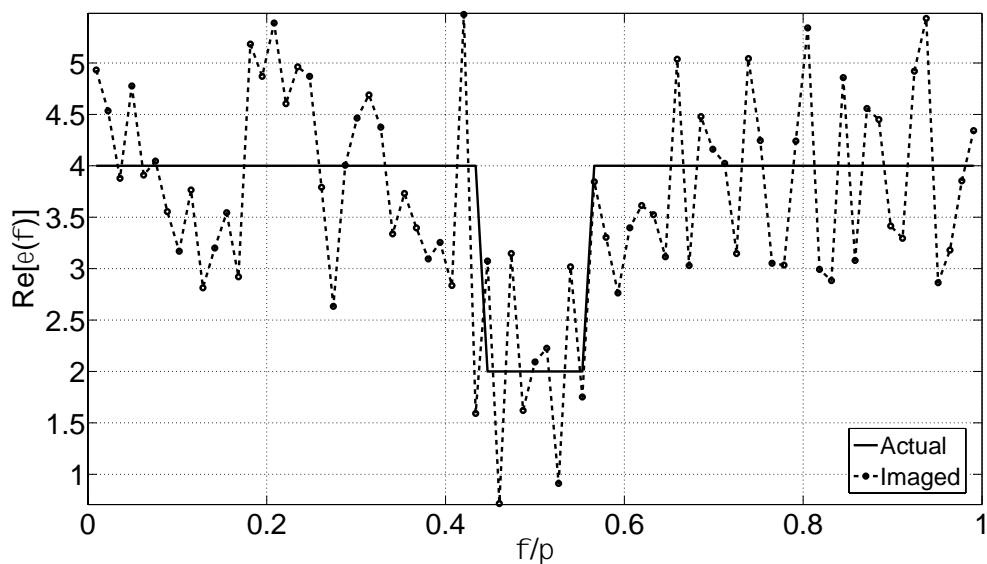


Figure 5.86: With signal-to-noise ratio (SNR) set to 5, real part of reconstructed permittivity distribution is illustrated.

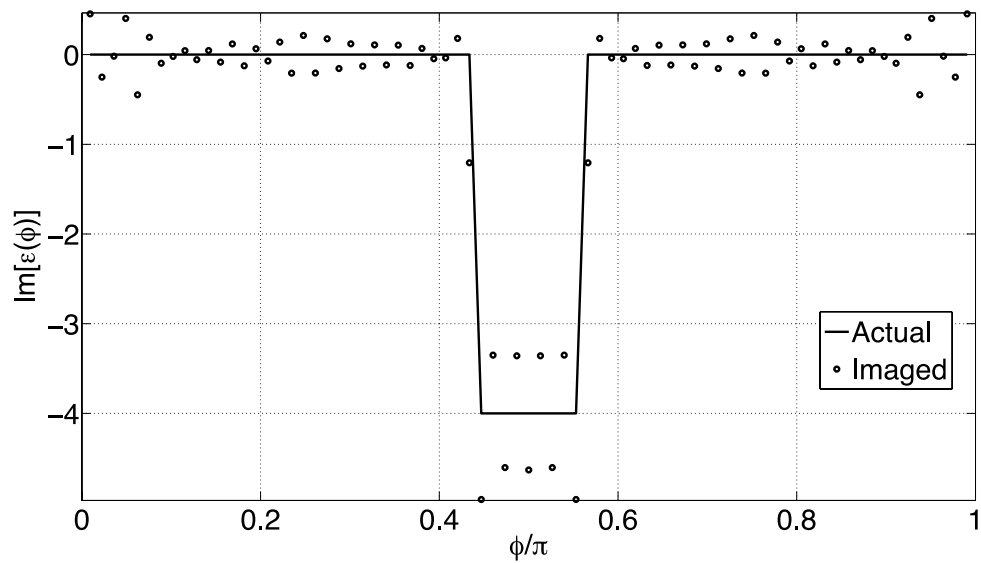


Figure 5.87: With no noise added, imaginary part of reconstructed relative permittivity is illustrated.

Imaginary part of permittivity reconstruction without any noise added is shown in Figure 5.87. When noise is added, imaginary permittivity reconstruction is shown in Figure 5.88 with signal-to-noise ratio (SNR) 20. It is noted that inverse problem solution without noise provides better permittivity reconstruction.

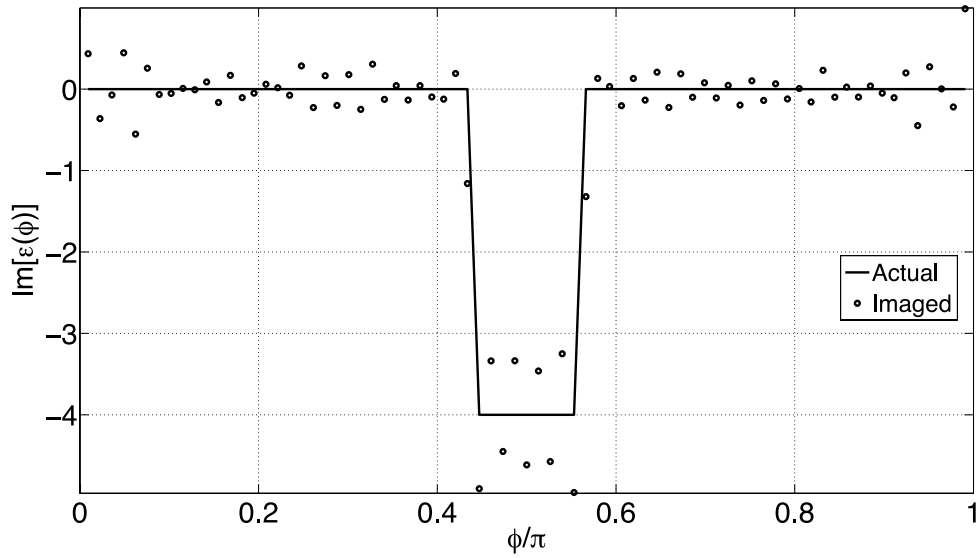


Figure 5.88: When signal-to-noise ratio (SNR) is 20, imaginary part of reconstructed permittivity distribution is compared to true permittivity distribution.

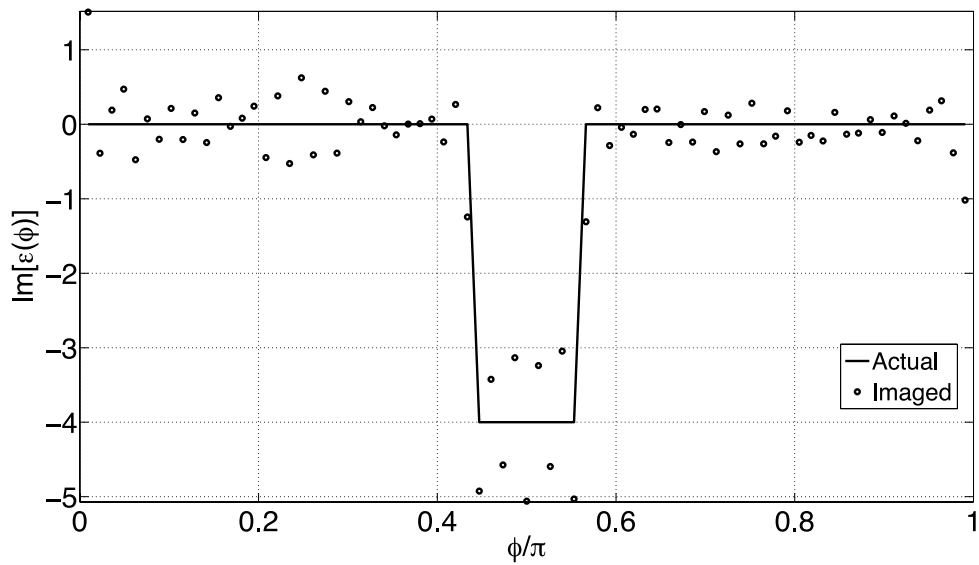


Figure 5.89: Imaginary part of reconstructed permittivity distribution compared to true permittivity distribution when signal-to-noise ratio (SNR) is 10.

Figure 5.89 shows permittivity reconstruction with signal-to-noise ratio (SNR) set at 10. Also, when signal-to-noise ratio is set to 5, imaginary part of reconstructed permittivity is illustrated in Figure 5.90. We note that introduction of noise produces more erroneous permittivity reconstruction. The solution does not change rapidly with high noise introduction. This shows robustness of inverse problem solution obtained through our proposed method.

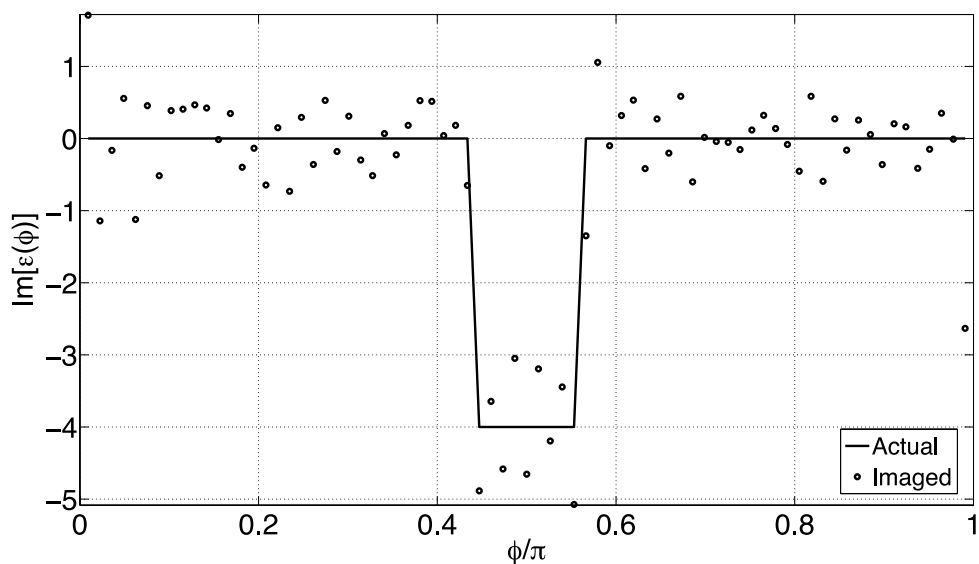


Figure 5.90: With signal-to-noise ratio (SNR) set to 5, imaginary part of reconstructed permittivity distribution is illustrated.

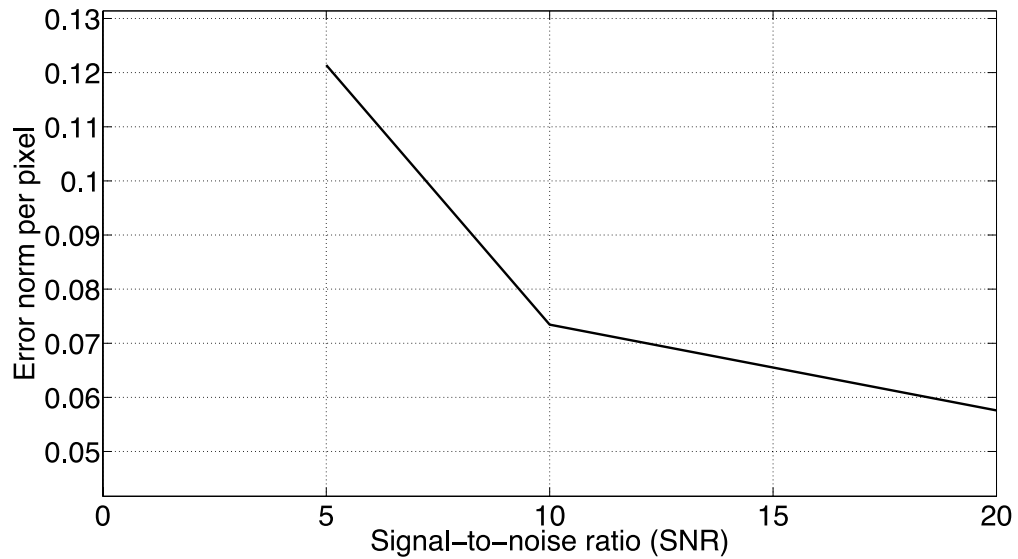


Figure 5.91: Effect of noise on error norm per pixel is illustrated.

This section has presented effect of noisy data. All the observations are listed as follows:

- Low signal-to-noise ratio (SNR), i.e. high noise, has been introduced to show robustness of our solution. Our solution is stable and hence introduces low error with noisy data.
- Robustness of inverse problem solution using proposed technique proves that we have not committed inverse crime.

Chapter 6

Conclusion and Future work

6.1 Conclusion

We have presented well-posed inverse problem solution utilizing Maxwell fish-eye lens. The results suggest inverse problem can be made well-posed through appropriate background medium choice. For the demonstrated cases, elimination of ill-posedness shows proper permittivity reconstruction for high enough contrast. We are not introducing resolution improvement. Other conventional techniques exhibit same resolution, such as diffraction tomography, but they work for low contrast. Our proposed technique shows proper reconstruction for high enough contrast and, at the same time, improves well-posedness despite noisy data. So, pursuing solution to inverse problem using proposed method will not only pose inverse problem in well-posed form, but also will increase robustness of the solution against noisy data. The main value of this work is not the practicality of the problem we have considered, but rather the demonstration that inverse problem can be cast in well-posed form. Our objective was to demonstrate that inverse source

problem and inverse scattering problem are not inherently ill-posed. They are ill-posed because typically experiments are staged in free space or in medium which does not support separation of scattered fields onto distinct observation locations. We have numerically presented this concept to reconstruct permittivity accurately and its robustness to noisy data. Extensions are required to make this method more practical. This work is a first step to a path where we seek proper background medium to cast two-dimensional or three-dimensional inverse problem in well-posed form. The numerical experiments were done in absence of inverse crime, i.e., the forward problem was solved with higher discretization. In addition, when the inverse problem was solved using noisy data, the proposed method remains stable. Thus, validating the robustness of the method.

6.2 Future work

The presented technique casts inverse problem in well-posed form for an object of interest with one dimensional permittivity variation. The challenge that follows is to generalize the concept to two dimensions and subsequently to three dimensions. Further research needs to be made to formulate methods for two dimensional permittivity reconstruction. The goal is to concentrate scattered field emanating from different regions to be focused onto different observation locations. To concentrate scattered field, microwave lenses may be utilized. In addition, holograms may be used to form image of two dimensional permittivity variations.

References

1. Vladimir Okhmatovski, Jonatan Aronsson, Lotfollah Shafai, “A well-conditioned non-iterative approach to solution of the inverse problem,” *IEEE Transactions Antennas and Propagation*, vol. 60, no. 5, pp. 2418-2430, May 2012.
2. Roger F. Harrington, *Time-Harmonic Electromagnetic Fields*, *IEEE Press*, 2001.
3. W. C. Chew, *Waves and Fields in Inhomogeneous Media*, *IEEE Press*, 1995.
4. Michael L. Oristaglio, Hans Blok, *Wavefield Imaging and Inversion in Electromagnetics and Acoustics*, Cambridge University Press, 2004.
5. Jack H. Richmond, “Scattering by a Dielectric Cylinder of Arbitrary Cross Section Shape,” *IEEE Transactions on Antennas and Propagation*, vol. 13, issue: 3, pp. 334- 341, 1965.
6. R. Szmytkowski, “Green’s function for the wavy Maxwell fish- eye problem,” *Journal of Physics A: Mathematical and Theoretical*, vol. 44, no. 6, pp. 065203, 2011.
7. Constantine A. Balanis, *Advanced Engineering Electromagnetics*, John Wiley & Sons, 1989.
8. Puyan Mojabi (2010), “Investigation and Development of Algorithms and Techniques for Microwave Tomography”, Ph.D. thesis, University of Manitoba, Canada.
9. E. N. Vasilév, V. Okhmatovski, “Diffraction of a surface electromagnetic wave by a junction of the dielectric and metal plates”, *Journal of communications technology & electronics*, vol. 41, no. 13, pp. 1083-1087, 1996.

10. E. N. Vasilév, V. Okhmatovski, "Diffraction of an electromagnetic wave by a junction of the dielectric and metal plates", *Journal of communications technology & electronics*, vol. 41, no. 11, pp. 963-968, 1996.
11. E. N. Vasilév, V. V. Solodukhov, A. I. Fedorenko, "The Integral Equation Method in the Problem of Electromagnetic Waves Diffraction by Complex Bodies", *Electromagnetics*, Vol. 11, Issue 2, pp. 161-182, 1991.
12. COMSOL Multiphysics – Wikipedia, accessed March 28, 2014, <http://en.wikipedia.org/wiki/COMSOL_Multiphysics>
13. A.J. Devaney, G.C. Sherman, "Non-uniqueness in inverse source and scattering problems," *IEEE Trans. Antennas Propag.*, vol. 30, no. 5, pp. 1034-1042, Sept. 1982.
14. D. Wilton, S.M. Rao, A.W. Glisson, D.H. Schaubert, "Potential integrals for uniform and linear source distributions on polygonal and polyhedral domains", *IEEE Trans. Antennas Propag.*, vol. AP-32, no. 3, pp. 276281, Mar. 1984.
15. Shanjie Zhang, Jian-Ming Jin, *Computation of special functions*, Wiley, 1962.
16. D. D. Jackson, "The use of a priori data to resolve non-uniqueness in linear inversion", *Geophys. J. Roy. Astron. Soc.*, vol. 57, pp. 137-157, April 1979.
17. G. Golub, C. Van Loan, *Matrix Computations*, 3rd edition, John Hopkins U. Press, 1992.
18. Emil Wolf, "Three-dimensional structure determination of semi-transparent objects from holographic data", *Optics Communications*, vol. 1, no. 4, pp. 153-156, October 1969.
19. A. J. Devaney, "A filtered back propagation algorithm for diffraction tomography", *Ultrasonic Imaging*, vol. 4, no. 4, pp. 336-350, October 1982.
20. C. Torres-Verdin, T.M. Habashy, "A two-step linear inversion of two-dimensional electrical conductivity", *IEEE Trans. Antennas Propag.* vol. 43, no. 4, pp. 405-415, April 1995.
21. W. C. Chew, Y. M. Wang, "Reconstruction of Two-Dimensional Permittivity Distribution using the Distorted Born Iterative Method", *IEEE Transactions on Medical Imaging*, vol. 9, no. 2, June 1990.